*Doklady Physics, Vol. 45, No. 12, 2000, pp. 635–639. Translated from Doklady Akademii Nauk, Vol. 375, No. 4, 2000, pp. 457–461.*
*Original Russian Text Copyright © 2000 by Elyutin, Ermolaev, Laptev, Manukhin.*

**PHYSICS**

# The Effect of Metallic Phase in a Diamond Polycrystal on Its Oxidation

**Academician A. V. Elyutin, A. A. Ermolaev, A. I. Laptev, and A. V. Manukhin**

Received April 26, 2000

The oxidation process of diamond powders in various media and under various conditions has been analyzed in a large number of papers. There is no common opinion on the mechanism of diamond gasification. The kinetics of the oxidation process is very sensitive to the grain shape, size, and impurity content in diamond powders. The ARK4 and ARV1 diamond powders obtained by crushing polycrystalline diamonds of the carbonado and ballas types contain up to 20 wt % of metallic impurities, whose composition corresponds to commonly used catalyst alloys. However, there has been no systematic study on the effect of catalyst alloy content on the oxidation kinetics of polycrystalline diamonds.

In this paper, we study the effect of catalyst alloy content on the oxidation process in the ARK4 polycrystalline diamond powders. The powders were prepared by crushing carbonado diamonds. Carbonado polycrystals were synthesized using MGOSCH graphite over the course of 15 s at 1800–1900 K with a starting pressure equal to 8.0 GPa. A toroid-type high-pressure chamber was used for the synthesis of the crystals.

The oxidation of diamonds in air was studied under nonisothermic conditions using the Paulik–Paulik–Erdelyi derivatograph. For each sample, thermogravimetric (TG), differential thermogravimetric (DTG), and differential thermal (DTA) curves were recorded. The measurements were characterized by the following values of sensitivity: 200 and 500 mg/100 divisions for TG curve, 1/10 (DTG curve), 1/15 (DTA curve). The studies were carried out in ambient air at atmospheric pressure. The heating rate was 5 K/min for heating up to 1270 K and 7.5 K/min for heating up to 1670 K. Ceramic crucibles and platinum plates were used as vessels for the samples. The mass of the batch of polycrystalline diamond powder was 0.5 g. Aluminum oxide annealed at 1700 K was used as the standard.

The study of the oxidation process in polycrystalline diamonds included two stages: analysis of the oxidation process in ARK4 800/630 diamond powders obtained with the use of a Cr20Ni80 alloy as a catalyst and study of the resistance to oxidation of ARK4 250/200 powder produced in the case of different metallic systems. The thermograms characterizing the oxidation of these diamond powders (Fig. 1, ceramic crucibles were used as vessels) illustrate the complexity of the processes occurring in the system under study. The initial stage of carbonado oxidation at temperatures above 850 K is characterized by an exothermic effect (the DTA curve), by a loss of mass (TG curve), and by an increase in the reaction rate (DTG curve). The exothermic effect attains its peak at 1030–1050 K. As a result of further heating, the enthalpy of the system under study increases (the DTA curve goes down, illustrating the decreasing heat release in the oxidation process), whereas the oxidation rate changes only slightly. At 1120–1150 K, another exothermic peak is observed in the DTA curve simultaneously with a sharp increase in the oxidation rate (DTG curve). Beginning from 1170 K, the reaction under study shifts toward the endothermic zone, since the oxidation process is accompanied by heat absorption, and the oxidation rate, having attained its maximum, slightly decreases and then remains nearly unchanged. At a temperature of about 1300 K, a local endothermic minimum (DTA curve) is observed, which is related to the melting of the metallic phase in diamond polycrystals. The melting of eutectics is accompanied by a certain increase in the oxidation rate, manifesting itself not only in the DTG curve but also in the DTA curve, which shifts toward the exothermic side of the oxidation process.

From the standpoint of application, it is undoubtedly of primary importance to study the initial stages of the oxidation process in diamond polycrystals, because significant changes in their physical and mechanical properties occur at relatively low temperatures. Qualitatively, description of the initial stages of the oxidation process in polycrystalline diamonds seems to be similar to that reported in [1, 2] for the oxidation of synthetic diamond single crystals. At the beginning, when there are no limitations on oxygen transport to the diamond surface, the exothermic reaction dominates:

$$C_{diam} + O_2 \rightarrow CO(CO_2) + Q. \quad (1)$$

A certain amount of the heat absorption by the system under study at 1070–1120 K is most probably related to the fracture of the diamond crystallites [3].

*Moscow State Institute of Steel and Alloys, Leninskiĭ pr. 4, Moscow, 117936 Russia*

1028-3358/00/4512-0635$20.00 © 2000 MAIK “Nauka/Interperiodica”

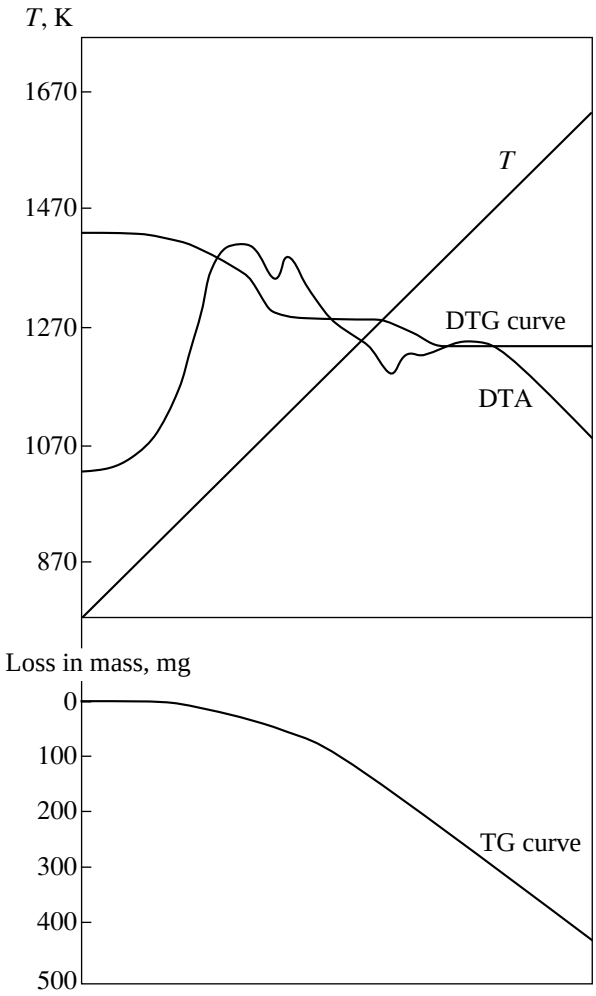


**Fig. 1.** Oxidation thermogram for ARK4 800/630 powder. The vessel for the sample is a ceramic crucible; the batch mass is 500 mg.

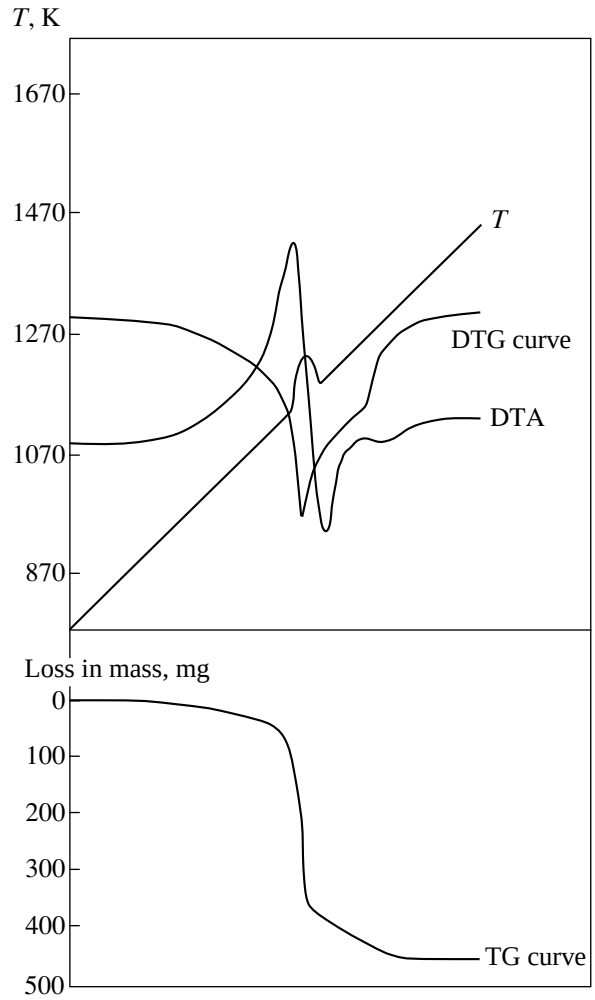


**Fig. 2.** Oxidation thermogram for ARK4 800/630 powder. The vessel for the sample is a platinum plate; the batch mass is 500 mg.

Oxygen adsorption at the virgin surfaces results in a decrease in the reaction rate (DTG curve) and then, in its steep increase, represented by the exothermic peak in the DTA curve.

Carbon oxide CO, arising according to the above reaction, transforms partially or completely into $CO_2$ if there is enough oxygen. Enhancement of the $CO_2$ concentration in the intergrain pores and above the diamond batch in the free space of the crucible impedes oxygen transport to the reaction zone. This causes a change in the mechanism of diamond oxidation [1]. The following endothermic reaction begins:

$$C_{diam} + CO_2 \rightarrow CO - Q. \quad (2)$$

The existence of the peak in the DTA curve testifies to the limitations of oxygen transport for oxygen atoms and is a consequence of the competition between reactions (1) and (2). The pronounced endothermic effect in the system under study suggests that the second reaction dominates above 1100 K.

The sequence of the oxidation stages in the polycrystalline diamond is most clearly illustrated by analysis of the thermogram shown in Fig. 2. In this case, platinum plates were used as vessels for the diamond powder batch. As a result, both the oxygen transport to the diamond surface and the removal of reaction products becomes easier in the process of oxidation. The oxidation of carbonado, which begins at temperatures above 850 K, occurs as an exothermic reaction. The oxidation rate significantly increases at temperatures above 1100 K, and the DTA and DTG curves confirm this fact. The oxidation has such an intensity that the heat released in the exothermic reaction becomes sufficient for the diamond powder to be self-heated. The sharp temperature increase in the reaction zone (curve *T*) is an indication of this fact. The amount of carbon dioxide produced in the course of the actively

proceeding reaction (1) is so large that this gas does not have enough time to leave the reaction zone, and, as a consequence, a pronounced endothermal dip is observed in the DTA curve immediately after the exothermic peak at 1170 K. The former is an indication of intense endothermic reaction (2). The significant heat absorption by the system under study in the course of this reaction affects even the temperature decrease (curve *T*) in the reaction zone. A certain decrease in the oxidation rate of the polycrystalline diamond (DTG curve) can also be explained by this effect. Further on, the oxidation process occurs in the endothermic zone and the shape of the DTG and DTA curves is determined by the competition of exothermic and endothermic reactions (with account taken of the relatively intense removal of the oxidation products).

The effect of chromium in the alloys of a nickel–chromium system and the effect of carbon in the alloys of a Cr20Ni80–carbon system used for producing diamond polycrystals were studied based on the estimate of the mass loss $\Delta m/m$ for ARK4 250/200 powders on heating up to 1270 K. The heating was performed at a rate of 5 K/min. The resistance to oxidation of the diamond powder increases with chromium content in the catalyst up to 20 wt % ($\Delta m/m$ decreases from 37 to 23%). The increase in the carbon content in the catalyst leads to lowering of the resistance of the diamond to oxidation ($\Delta m/m$ attains 33%). Introducing titanium, tantalum, and molybdenum into the catalyst alloy Cr20Ni80 does not affect the resistance of the diamond to oxidation. The temperature at which the batch mass of ARK4 250/200 powder reduces by one percent was considered the temperature of the onset of oxidation $T_{\text{onset}}$. For ARK4 250/200, $T_{\text{onset}}$ was always equal to 910 K.

The effect of boron and boron-containing compounds upon the oxidation of polycrystalline diamonds was studied by doping of Cr20Ni80- and Mo15Ni85-based catalyst alloys, respectively. The Cr20Ni80 alloy was doped by up to 10 wt % of boron, and up to 50 wt % of borides $TiB_2$ and $BN_{\text{cub}}$ was introduced into the Mo15Ni85 alloy. Quantitative spectral analysis demonstrated that the boron content in the polycrystals (up to 4%) was proportional to that in the catalyst alloy Cr20Ni80 and that the introduction of up to 10–15% borides into the Mo15Ni85 alloy also results in a proportional enhancement of the boron content in the polycrystals. Analysis of the oxidation thermograms for the ARK4 250/200 polycrystalline diamond demonstrated that boron and titanium diboride introduced into the initial catalyst alloy stimulate a substantial increase in the resistance to oxidation of the synthesized carbonado. Oxidation starts above 900 K, and up to 1100 K, the polycrystalline diamond is oxidized at a very low rate. Hence, the exothermic peak (at 1130 K) and the endothermic dip in the DTA curve become shifted toward higher temperatures.

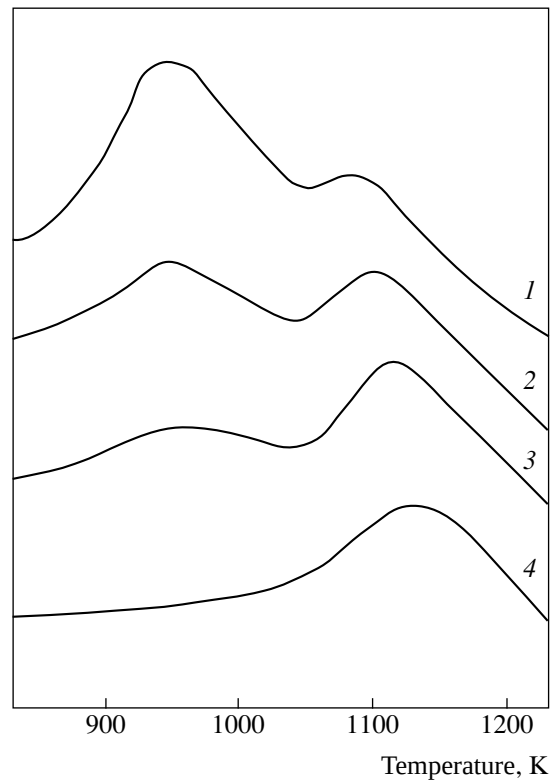


**Fig. 3.** Qualitative change in the initial stages of the oxidation process (DTA curves) for a polycryctalline diamond at various contents of titanium diboride in the initial catalyst. The powders are ARK4 250/200; the vessels for the sample are ceramic crucibles. Contents of titanium diboride in Mo15Ni85 catalyst are (*1*) 0; (*2*) 1; (*3*) 5; (*4*) 10%.

Qualitative changes in the initial oxidation stages of the synthetic polycrystalline diamond with an increase in the titanium diboride content in the catalyst used for the synthesis can be revealed by analysis of the DTA curve corresponding to the oxidation thermograms (Fig. 3). Even a small addition (1%) of $TiB_2$ into the catalyst results in a larger splitting of the exothermic peaks: the first peak becomes lower and the second slightly increases. Such a picture testifies to the decrease as a whole in the intensity of oxidation for polycrystalline diamond at the initial period of time. At a low content of boron-containing compounds, the amount of boron seems to be insufficient for the formation of a dense protective $B_2O_3$ film. Thus, the oxidation of diamond and the formation of the protective film occur simultaneously with an increase in temperature. The complicated form of the DTA curve is a consequence of these two simultaneous processes. An increase in the $TiB_2$ content in the catalyst results in smoothing of the first exothermic peak corresponding to the carbonado oxidation reaction until the peak completely disappears. This occurs when the amount of

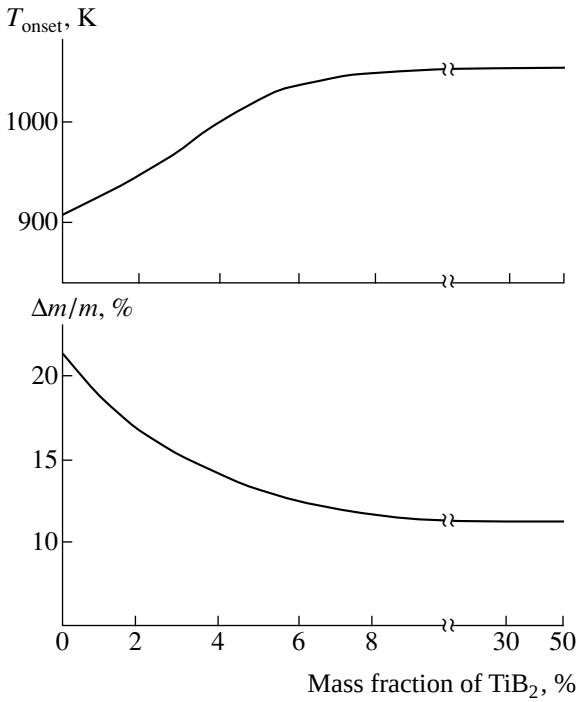


**Fig. 4.** The effect of titanium diboride content in the initial catalyst on the temperature of the oxidation onset $T_{onset}$ and on the relative mass loss $\Delta m/m$ for the polycrystalline diamond. $T_{onset}$ corresponds to the 1% mass loss for the ARK4 250/200 powder; $\Delta m/m$ is the mass loss for ARK4 250/200 while heating in ambient air up to 1270 K.

$TiB_2$ introduced attains 10%. In addition, the second exothermic peak undergoes a certain shift to higher temperatures (up to 1130 K). This evolution of the DTA curves seems to be related to the enhancement in uniformity of the protection of polycrystalline diamond against oxidation. This results in lowering of the oxidation intensity.

The results of quantitative analysis of the oxidation thermograms for polycrystals synthesized on the basis of a Mo15Ni85–$TiBr_2$ catalyst system are shown in Fig. 4. The increase in the $TiB_2$ content in the catalyst up to 10% is accompanied by a quantitative increase in the resistance to oxidation of the synthesized diamond polycrystals. The increase in the resistance to oxidation is characterized by the following parameters: $T_{onset}$ increases from 910 to 1040 K and $\Delta m/m$ decreases from 22 to 11% (heating to 1270 K at a rate of 7.5 K/min). Further increase in the $TiB_2$ content does not cause any changes in the quantitative characteristics of the carbonado oxidation process. The resistance to oxidation of polycrystals exhibits no quantitative changes, if, in addition to titanium diboride, the initial catalyst contains cubic boron nitride. A similar quantitative enhancement of the resistance to oxidation is observed for carbonado polycrystals when the Cr20Ni80–B system is used as a catalyst for synthesis.

The enhancement of the resistance to oxidation for diamond polycrystals containing boron compounds is caused by the formation of boron oxide ($B_2O_3$) due to interaction with air oxygen. For example, titanium diboride starts to oxidize at a temperature of approximately 700 K [4]. Melting of $B_2O_3$ (above 900 K) seems to enhance its protective properties, since the high-mobility liquid oxide film "heals" the macro- and microdefects in the diamond polycrystal. $B_2O_3$ oxide manifests itself as a white substance at the surface of boron-containing polycrystalline diamonds after they have been heated.

The experimental results presented above, in particular, the evolution of the DTA curves corresponding to the oxidation thermograms (Fig. 3) and the quantitative variation in the resistance to oxidation for carbonado polycrystals (Fig. 4), are adequately explained by the formation of a protective $B_2O_3$ oxide film. However, if we use a catalyst with another boron-containing compound, namely, cubic boron nitride, the enhancement of the resistance to oxidation is not observed for synthesized diamond polycrystals, since the quantitative characteristics of the oxidation process remain almost unchanged. This can be explained by the fact that cubic boron nitride starts to oxidize at higher temperatures than diamond does [5].

Thus, in this paper, we revealed the features of the oxidation process for polycrystalline carbonado diamonds. The sophisticated character of this process is determined by the exo- and endothermic reactions proceeding in succession and in parallel to the gasification of the diamond.

It was experimentally established that by introducing carbon into the initial Cr20Ni80 catalyst alloy, we increase the carbonado oxidation rate. This testifies to the fact that the ultimate saturation of the metallic phase in polycrystals by carbon is not attained in the synthesis of diamond polycrystals.

It was found that doping by boron ($TiB_2$) results in both an increase in the oxidation onset temperature for polycrystalline diamond from 910 to 1040 K and a slowing down of the diamond oxidation rate, which is related to the formation of a protective layer of $B_2O_3$ oxide at relatively low temperatures.

The evolution of the experimental DTA curves corresponding to the carbonado oxidation thermograms discussed in this paper clearly demonstrates a qualitative change in the initial stages of the oxidation process for polycrystalline diamond with enhanced $TiB_2$ content in the catalyst used for synthesis. This change manifests itself in a shift of the exothermic peaks toward higher temperatures, which is caused by enhancement of the uniformity of diamond protection against oxida-

tion with an increase in the amount of protective $B_2O_3$ oxide.

## REFERENCES


1. V. V. Ogorodnik, É. A. Pugach, and G. G. Postolova, in *Surface and Thermal Properties of Diamonds* (Inst. Sverkhtverd. Mater., Akad. Nauk USSR, Kiev, 1985), pp. 42–48.
2. V. V. Ogorodnik, É. A. Pugach, and G. G. Postolova, in *Physical and Chemical Properties of Superhard Materials and Methods of Their Analysis* (Inst. Sverkhtverd. Mater., Akad. Nauk USSR, Kiev, 1987), pp. 59–64.
3. V. V. Ogorodnik, É. A. Pugach, and G. G. Postolova, in *Interaction of Diamonds with Gaseous and Liquid Media* (Kiev, 1984), pp. 51–58.
4. É. A. Pugach, M. S. Borovikova, S. I. Filipchenko, *et al.*, in *Borides and Boride-Based Materials* (Inst. Sverkhtverd. Mater., Akad. Nauk USSR, Kiev, 1986), pp. 125–130.
5. Yu. V. Naĭdich, G. A. Kolesnichenko, I. A. Lavrinenko, and Ya. F. Motsak, *Soldering and Metallization of Superhard Tool Materials* (Naukova Dumka, Kiev, 1977).


*Translated by T. Galkina*

*Doklady Physics, Vol. 45, No. 12, 2000, pp. 640–642. Translated from Doklady Akademii Nauk, Vol. 375, No. 4, 2000, pp. 462–464.*
*Original Russian Text Copyright © 2000 by Mesyats, Barengol'ts.*

**PHYSICS**

# A High-Current Vacuum Arc as a Collective Multiecton Process

**Academician G. A. Mesyats and S. A. Barengol'ts**

Received July 19, 2000

It may be taken for granted that the functioning of a cathode spot of a vacuum arc at low electric-current values (on the order of several threshold values for the arc-discharge currents) is caused by electric microexplosions at the cathode surface due to the high energy concentration in the cathode's microvolumes [1, 2]. Each of such microexplosions emits a portion of electrons (electron cluster) referred to as an ecton. On this basis, the occurrence of spatial (cells) and time (cycles) discreteness of a cathode spot was explained in [3]. From the data of [3], the cell current for mercury and copper cathodes is $2i_{thr}$, where $i_{thr}$ is the threshold current. This is also confirmed by later measurements for tungsten and molybdenum cathodes [4]. According to the ecton model, a cathode spot of a high-current vacuum arc consists of a number of autonomous cells and each of them proceeds for a time $\sim 10^{-8}$ s. This conclusion is confirmed by the fact that the trace of a cathode spot always has a substructure (small craters with a size of $\sim 10^{-4}$ cm [5-7]) and also by optic studies of cathode-spot structure [8].

However, there are certain facts that do not fit into the above concept. The most essential of them is that there exists a critical current such that, upon attaining it, a spot is divided into parts. For many metals (Cu, Mo, W, Al, etc.), this current amounts to $i_l$ = 50–300 A [5]; i.e., it is many times higher than the double arc threshold current. There are other facts that, at first glance, also contradict the idea of the spot's cellular structure: the increase in the cathode-spot diameter with current [9], the dependence of the spot-current density on the arc current intensity [9], the increase in formation time for a trace of a cathode spot with current [7], etc.

Nevertheless, assuming that a high-current arc ($i \gg 2i_{thr}$) is a collective ecton process, all these points can be explained. As was noted above, a major argument in favor of this assumption is the presence of microcraters with radius $r_c$ on the order of $10^{-4}$ cm in a cathode-spot trace [5–7]. This is not only qualitative, but also quantitative evidence of ecton processes in a cathode spot. Indeed, if a crater is produced because of the thermal conductivity, the speed of the thermal boundary attains $10^4$ cm/s; therefore, the formation time for such a crater is $\tau_c \sim 10^{-8}$ s. If the current flowing through a cell is $i_c = 2i_{thr}$ and $i_{thr} \sim 1$ A [3], then the current density in the cell will be $j_c \sim 10^8$ A/cm$^2$. Such values for the parameters $r_c$, $\tau_c$, and $j_c$ stem from ecton processes in a cathode spot of a vacuum arc [1].

With the purpose of analyzing the parameters of a cathode spot, we use experimental data obtained by Daalder [9]. In the figure, the most probable diameter of a cathode-spot trace is shown as a function of the vacuum-arc current for a copper cathode. From this figure, it follows that the spot diameter is ~4 μm for currents lower than 40 A and, furthermore, linearly increases with the current. The dependence of the mean spot-current density on the current magnitude (see figure) exhibits a pronounced maximum; $j \sim i$ to the left of the maximum and $j \sim i^{-1}$ to the right of it. For an arc current equal to the double threshold value, the current density estimated from a spot trace is $2.7 \times 10^7$ A/cm$^2$ and the current-density maximum is $j_m = 2 \times 10^8$ A/cm$^2$. Therefore, for $j = j_m$, no less than seven cells located in immediate proximity to each other act in the cathode spot; i.e., this is the maximum overlapping of cells in

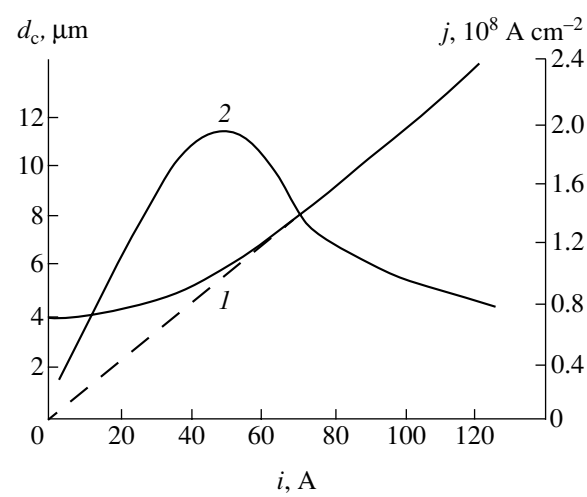


Vacuum arc with a single cathode spot in the case of a copper cathode [9]: (*1*) most probable diameter of the crater and (*2*) spot-current density as functions of the arc current.

*Institute of Electrophysics, Ural Division,*
*Russian Academy of Sciences,*
*Komsomol'skaya ul. 34, Yekaterinburg, 620219 Russia*

1028-3358/00/4512-0640$20.00 © 2000 MAIK "Nauka/Interperiodica"

the current density. Thus, a cathode spot of a high-current vacuum arc is caused by a multiecton process. Collectivization of plasma flows for individual ecton cycles occurs in this process, and this fact explains many of the apparent contradictions between high-current and low-current arcs.

We now consider this effect in more detail. In the case of low currents, a weak dependence of the diameter of a cathode-spot trace on the current intensity (see figure) follows from the fact that this trace is governed by the thermal conductivity of the cathode material. Indeed,

$$d_c = 4(at_c)^{1/2}, \tag{1}$$

where $a$ is the thermal diffusivity and $t_c$ is the current-flow time during the ecton cycle. For copper, $t_c \approx 3 \times 10^{-8}$ s and $a = 0.42$ cm$^2$/s (liquid copper) [1]. Therefore, $d_c \approx 4$ μm, which is consistent with the results of [9]. In this case, the current density is

$$j = \frac{4i}{\pi d_c^2}; \tag{2}$$

i.e., in the right-hand side of the curve $j(i)$, we have $j \sim i$.

In the linear high-current segment of the curve $d_c(i)$ (see figure), the expansion of the cathode-spot radius is determined by the Joule heating. Under the assumption that, for the arc current $i \gg 2i_{thr}$, a number of cells simultaneously act inside a cathode spot, the cyclicity factor can be disregarded and the arc current can be considered as time-independent; i.e., $i$ = const. In this case, the diameter of a crater produced due to the Joule heating is found from formula given by [1] as

$$d = \frac{\sqrt{2}i}{\pi}\left(\frac{t}{\bar{h}}\right)^{1/4}, \tag{3}$$

where $\bar{h}$ is the specific action for an explosion. The arc current is assumed to flow from a flat cathode surface. The crater expansion ceases at the time moment when the heat transfer into the cathode interior owing to the thermal conductivity begins to play an essential role, i.e., when

$$\frac{\sqrt{2}i}{\pi}\left(\frac{t}{\bar{h}}\right)^{1/4} = 4(at)^{1/2}. \tag{4}$$

From formula (4), it follows that the lifetime for such a collective cathode spot is

$$\tau_c = \frac{i^2}{64\pi^2 a^2 \bar{h}}, \tag{5}$$

its diameter is

$$d_c = \frac{i}{2\pi\sqrt{a\bar{h}}}, \tag{6}$$

and the current density is

$$j \approx \frac{16\pi a\bar{h}}{i}. \tag{7}$$

Therefore, as in the experiments described in [9], we obtain $d_c \sim i$ and $j \sim i^{-1}$ for high currents (see the figure). It is also worth noting that, according to the Juttner data (see [7]), the spot lifetime in the case of a copper cathode for current values of $i \geq 50$ A attains $\tau_c \sim i^2$, which is in agreement with relation (5) derived by us.

Here, the following question arises: To what value of the current will a cathode spot of a high-current vacuum arc exist as a whole? Evidently, this will remain true as long as it is profitable from the energetic standpoint, namely, as long as the mean current density in a spot exceeds the current density in an individual cell, i.e., as long as the collectivization of cathode-plasma flows takes place. In this case, both the energy concentration and the plasma density are higher than for autonomous cells and they are confined to a single collective cathode spot. As soon as these current densities become equal, spot splitting occurs. The corresponding arc current is the cathode-spot ultimate current.

For understanding the mechanism of confining cells in a cathode spot for an arc current below its ultimate value and for explaining the nature of the ultimate current, we turn back once again to the dependence $j(i)$. The spot-current density has a maximum for a current magnitude of ~50 A. The intensity of the arc current $i_m$, which corresponds to the maximum current density, can be estimated from formulas (2) and (7) by equating quantities $j$. Then, we obtain for the current $i_m$

$$i_m = 2\pi(a\bar{h})^{1/2}d_c, \tag{8}$$

where $d_c$ is the cell crater diameter. From formula (8), the value of $i_m$ for copper is ~90 A. Changing the arc-current dependence of the current density according to the law $j \sim i^{-1}$ causes a decrease in the energy concentration in a spot with increasing current; such a spot tends to split.

The maximum value of the current density $j_m$ is $2 \times 10^8$ A/cm$^2$; i.e., it is more than seven times higher than the cell-current density. The number of cells acting in such a spot is $n \approx i_m/2i_{thr} \approx 16$. We call the ratio $\delta = j/j_c$ the overlap coefficient. For the 100-A current, the mean current density reduces to $j = 8 \times 10^7$ A/cm$^2$. Therefore, we have $\delta = 3$; i.e., there is a triple overlap of the current density, although in this case, the total number of cells in the cathode spot attains almost 30. All the processes in a spot are intensified for a large overlap $\delta$; the plasma pressure increases ($P \sim \delta$); the expansion velocity of liquid metal jets ($v_l \sim \delta^{1/2}$) [1] is enhanced; and the concentration of the cathode plasma rises as long as it is produced by several cells acting in immediate proximity to each other. Since the process of cathode-spot self-maintenance occurs due to plasma interaction with jets

of liquid metal, this promotes the confinement of all the cells at the same place in the case of $\delta > 1$. For $\delta \leq 1$, in such a collective spot, there will be no advantages for the existence of all the cells together. Therefore, this condition determines the ultimate arc current. To find its value from this condition, we use the dependence $j(i)$ once more. If it is continued to the region of higher current intensities, a value $\delta = 1$ is attained for $i \approx 150$–200 A; this must correspond to the ultimate current. This value of the current is consistent with the results for copper [10], according to which the mean number of cathode spots simultaneously acting on the copper cathode within the range 150–200 A is equal to two.

On the basis of this analysis, it can be concluded that the high-current vacuum arc is a collective multiecton process. From the energetic standpoint, the collectivization of cathode cells provides more advantageous conditions for initiation and reproduction of microexplosions inside a cathode spot. As the arc current increases, the mean current density in a spot decreases, which results in its splitting.

## ACKNOWLEDGMENTS

This study was supported by the Russian Foundation for Basic Research and International Science Foundations, projects no. 97-0663 and 99-02-18234, respectively.

## REFERENCES

1. G. A. Mesyats, *Ectons in Vacuum Discharge: Breakdown, Spark, Arc* (Nauka, Moscow, 2000).
2. G. A. Mesyats, IEEE Trans. Plasma Sci. **23**, 879 (1995).
3. I. G. Kesaev, *Cathode Processes in Electric Arc* (Nauka, Moscow, 1968).
4. V. F. Puchkarev and A. M. Murzakaev, J. Phys. D **23**, 26 (1990).
5. L. P. Harris, in *Vacuum Arcs: Theory and Application* (Wiley, New York, 1980).
6. G. A. Mesyats and D. I. Proskurovskiĭ, *Pulsed Electric Discharge in Vacuum* (Nauka, Novosibirsk, 1984).
7. B. Juttner, Beitr. Plasmaphys. **19**, 25 (1979).
8. B. Juttner, J. Phys. D **28**, 516 (1995).
9. J. E. Daalder, IEEE Trans. Power Appar. Syst. **PAS-93**, 1747 (1974).
10. B. E. Djakov and R. Holmes, J. Phys. D **4**, 504 (1971).

*Translated by V. Tsarev*

*Doklady Physics, Vol. 45, No. 12, 2000, pp. 643–646. Translated from Doklady Akademii Nauk, Vol. 375, No. 4, 2000, pp. 465–468.*
*Original Russian Text Copyright © 2000 by Trofimov, Mokerov.*

**PHYSICS**

# Kinetic Model of Heteroepitaxial Growth in the Presence of Schwebel Barriers

**V. I. Trofimov and Corresponding Member of the RAS V. G. Mokerov**

Received July 5, 2000

In recent years, considerable attention has been drawn to the problem of epitaxial growth in steps in the presence of the Schwebel diffusion barrier. This barrier hampers interlayer mass transfer and leads to morphological instability in the growth surface and to the formation of three-dimensional (3D) hillocks violating smooth epitaxial growth [1–6]. In [7, 8], we proposed a kinetic model of homoepitaxial growth in the presence of the Schwebel barriers and clearly demonstrated that an increase in barrier height leads to evolution from atomically smooth layer-by-layer growth to smooth multilayer growth and, then, to rough 3D growth. In this paper, we extend this model to the case of heteroepitaxial growth.

## THE MODEL

According to model [7, 8], growth takes place owing to the formation and development of consecutive 2D islands in successive monolayers. The interlayer mass transfer is taken into account using the concept of a feeding zone. This can be introduced in the following manner: we assume that only those atoms which are found in a stripe of width $\lambda$, which is adjacent to the perimeter of the islands, migrate into a lower layer from an arbitrarily chosen $k$th layer of atoms deposited on the islands. At the same time, the atoms deposited in the central part remain there, forming the feeding zone for the next $(k + 1)$th layer. The specific area $\xi_{ka}(t)$ of the feeding zone is related to the filling $\xi(t)$ of the $k$th layer by the formula $\xi_{ka}(t) = \xi_k(R(t) - \lambda)$, where $R(t)$ is the generalized radius of the islands. In [7], using the concept of the feeding zone, we derived a set of kinetic equations for homoepitaxial growth. For their generalization to the case of heteroepitaxy (with no misfit in the conjugated lattices), it is sufficient to take into account that atoms deposited directly on a substrate ($k = 1$) migrate along it according to with rate determined by the heterodiffusion coefficient $D_h$ (cm$^2$ s$^{-1}$). At the same time, the atoms deposited at the surface of the islands of the first layer and of all the subsequent layers ($k > 1$) already migrate along their native surface with a coefficient of self-diffusion, which we denote as $D_s$ (cm$^2$ s$^{-1}$). In this case, after the corresponding transformations, the kinetic equations for the surface concentrations of adatoms ($n_k'$) and 2D islands ($N_k'$) and for the filling $\xi_k$ in the $k$th layer can be written $\left(\text{in the dimensionless variables } n_k = \frac{n_k'}{N_0}, N_k = \frac{N_k'}{N_0}, \text{ and } \tau = \frac{Jt}{N_0}\right)$ in the following form:

$$\frac{dn_1}{d\tau} = (1-\xi_1) - 2\sigma_{11}\mu_h n_1^2 - \langle\sigma\rangle\mu_h n_1 N_1,$$

$$\frac{dN_1}{d\tau} = (1-\xi_1)\eta_{i*}\mu_h n_1^{i*+1} - 2\delta N_1\frac{d\xi_1}{d\tau},$$

$$\frac{dn_k}{d\tau} = (\xi_{k-1,a} - \xi_k) - 2\sigma_{11}\mu_s n_k^2 - \langle\sigma\rangle\mu_s n_k N_k, \quad (1)$$

$$\frac{dN_k}{d\tau} = (\xi_{k-1,a} - \xi_k)\eta_{i*}\mu_s n_k^{i*+1} - 2\delta N_k\frac{d\xi_k}{d\tau}, \quad k > 1,$$

$$\frac{d\xi_k}{d\tau} = \begin{cases}\xi_{k-1,a}, & \tau < \tau_{ck},\\ \xi_{k-1,a} - \xi_{ka}, & \tau > \tau_{ck},\end{cases} \quad k \geq 1.$$

Here, $\xi_{0a} \equiv 1$, because it is evident that the entire substrate serves as the feeding band for the first layer, whereas all $\xi_{ka}$ with $k \geq 1$ are given by the formulas

$$\xi_{ka} = \begin{cases}0, & \tau < \tau_{ck}\\ 1 - \exp\{-[(-\ln(1-\xi_k))^{1/2} - (-\ln(1-\xi_{ck}))^{1/2}]^2\}, & \tau > \tau_{ck}.\end{cases} \quad (2)$$

Here, $\mu_h$, $\mu_s$, $\eta_{i*}$, and $\omega$ are the numerical parameters

*Institute of Radio Engineering and Electronics, Russian Academy of Sciences, Mokhovaya ul. 11, Moscow, 103907 Russia*

of the model:

$$\mu_h = \frac{N_0^2 D_h}{J}, \quad \mu_s = \frac{N_0^2 D_s}{J},$$
$$\eta_{i*} = C_{i*}\exp\left(\frac{E_{i*}}{kT}\right), \quad \omega = \frac{\nu_s}{\nu_d} = \exp\left(-\frac{E_B}{kT}\right). \tag{3}$$

These parameters characterize the diffusion mobility of the adatoms ($\mu_h$ and $\mu_s$), the stability of the critical nucleus ($\eta_{i*}$), and the Schwebel effect ($\omega$). Furthermore, $J$ (cm$^{-2}$ s$^{-1}$) is the deposition rate; $\sigma_{11}$ and $\langle\sigma\rangle$ are the adatom–adatom and adatom–island (averaged over the entire ensemble of the islands) trapping coefficients, respectively; $i*$ is the size of the critical nucleus; $C_{i*}$ is the configuration constant; $E_{i*}$ is the binding energy for atoms in the critical nucleus; and $N_0$ (cm$^{-2}$) is the density of surface lattice sites. Coefficient $\delta$ takes into account the character of the coalescence: if the islands colliding with each other cease to grow at their contact area but retain their individuality and continue to grow in all permitted directions, then $\delta = 0$; if they merge to form a single island, $\delta = 1$. $\nu_s$ and $\nu_d$ are the frequencies of the diffusion-driven jumps of an adatom over the descending step at the island edge and at a smooth terrace with activation energies $E_s$ and $E_d$, respectively, and $E_B = E_s - E_d$ is the height of the Schwebel barrier. The critical time moments $\tau_{ck}$, corresponding to the nucleation of the $(k + 1)$th layer at the $k$th layer, are measured from the time moment when the $k$th layer arises. They determine the critical filling $\xi_{ck} = \xi_k(\tau_{ck})$ and are found from the integral equation

$$\frac{\pi\eta_{i*}}{(i*+2)\times 4^{i*+1}\mu_s^{i*}}$$
$$\times \int_0^{\tau_c} \rho^{2(i*+2)}\left\{\left[1+\frac{2}{\omega\rho}\right]^{i*+2} - \left[\frac{2}{\omega\rho}\right]^{i*+2}\right\}d\tau = 1,$$
$$\rho \equiv \frac{R}{a} = \rho(\tau) = \left[\frac{-\ln(1-\xi_k(\tau))}{\pi N_k(\tau)}\right]^{1/2}, \quad a = N_0^{-1/2}. \tag{4}$$

## RESULTS AND DISCUSSION

We now consider the case of the full condensation characteristic of epitaxy for semiconductors and assume that $i* = 1$. Then, we have $\eta_{i*} = \sigma_{11} = 2$ and $\delta = 1$. The trapping coefficient $\langle\sigma\rangle$ can be calculated using the relationship derived in the lattice approximation [9, 10]:

$$\langle\sigma\rangle = \frac{-4\pi(1-\xi)}{\ln\xi + (1-\xi)(3-\xi)/2}. \tag{5}$$

To characterize quantitatively the morphology of a growing film, we calculated the rms roughness based on kinetic curves for filling $\xi_k(\tau)$ of consecutive layers obtained by the numerical integration of the equations in (1):

$$\sigma \equiv [\langle h^2\rangle - \langle h\rangle^2]^{1/2}$$
$$= \left[\sum_{k=1}(2k-1)\xi_k - \left(\sum_{k=1}\xi_k\right)^2\right]^{1/2}, \tag{6}$$

where $h$ is the local thickness of the film, the angular brackets denote the averaging over the entire film, and $h$ and $\sigma$ are measured in units of monolayers. We also calculated the intensity of the reflection high-energy electron diffraction (RHEED) using the relationship

$$I(\tau) = \left[\sum_{k=0}(-1)^k(\xi_k - \xi_{k+1})\right]^2, \quad \xi_0 \equiv 1. \tag{7}$$

In principle, the Schwebel barrier can be both repulsive ($E_B \geq 0$) and attractive ($E_B \leq 0$). We restrict ourselves to the widespread case of a repulsive barrier which violates only smooth epitaxial growth because it gives rise to an ascending diffusion flux of adatoms. If this is absent, homoepitaxial growth (at sufficiently high values of $\mu$) occurs owing to the mechanism of atomically smooth layer-by-layer growth. In this case, roughness $\sigma$ oscillates with a period equal to the deposition time for a single monolayer between $\sigma_{max} = 0.5$ and $\sigma_{min} > 0$. The value of $\sigma_{min}$ serves as the measure of deviation of the actual growth observed from the ideal layer-by-layer growth for which $\sigma$ oscillates between $\sigma_{max} = 0.5$ and $\sigma_{min} = 0$ according to the $\sigma(\tau) = (\xi - \xi^2)^{1/2}$ law. In the presence of a barrier, the oscillations $\sigma$ damp gradually with an increase in barrier height (decreasing $\omega$) due to the growth of $\sigma_{min}$ and, for a certain value of $\omega$ depending on $\mu$ and $\sigma$, are stabilized at the level $\sigma_s \simeq 0.5$, indicating the transition from the layer-by-layer to smooth-multilayer growth when its front consists of several layers being filled simultaneously [8]. With subsequent decrease in $\omega$, the value of $\sigma_s$ increases continuously and, at a certain $\omega$, transition to the 3D growth occurs. This is characterized by an infinitely growing roughness. We concentrate on these transient regimes of growth (layer-by-layer to smooth multilayer and smooth multilayer to 3D).

In the figure, we show the results for fixed $\mu_s = 10^{10}$ and $\omega = 0.025$ corresponding to the layer-by-layer to smooth multilayer transition and for three values of $\mu_h$: $\mu_h = 10^8 < \mu_s$, $\mu_h = 10^{10} = \mu_s$ (homoepitaxy), and $\mu_h = 10^{12} > \mu_s$. After the deposition of several monolayers, the kinetics of growth in all these cases is, naturally, identical, because it is determined by fixed parameters $\mu_s$ and $\omega$; however, at early stages, there are significant distinctions. As is seen for $\mu_h < \mu_s$, the second layer nucleates much later ($\xi_{1c} = 0.826$) than for the homoepitaxy ($\xi_{1c} = 0.5$) that clearly manifests itself in a dip in the $\sigma(\tau)$ curve and in the enhanced peak in the

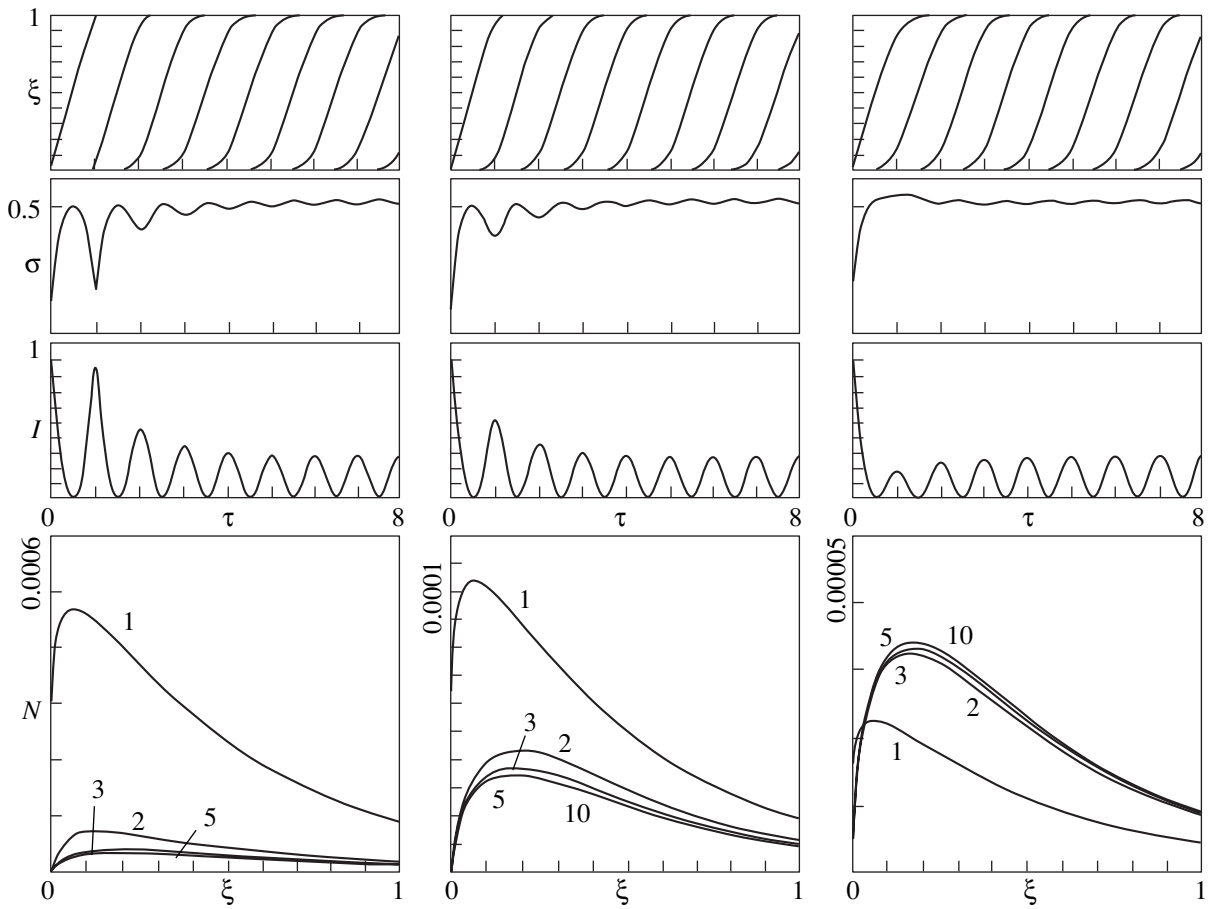


Kinetics of epitaxial growth for fixed values of $\mu_s = 10^{10}$ and $\omega = 0.025$ and three different values of $\mu_h$: $10^8$ (on the left), $10^{10}$ (in the center), and $10^{12}$ (on the right). From the top to the bottom: kinetic filling curves $\xi_k(\tau)$ of the consecutive layers, rms roughnesses $\sigma$, diffraction intensities $I$, and densities $N_k(\xi)$ of islands in the consecutive layers whose numbers are indicated near the curves.

$I(\tau)$ curve. This is explained by the fact that, owing to slow heterodiffusion, high-density islands are formed in the first layer and are, correspondingly, small in size. Thus, the highly mobile atoms deposited on them migrate into the first layer and, being built in at the perimeter of the islands, accelerate their growth. Therefore, the first layer becomes almost completely continuous before the nucleation of the second layer. On the other hand, for $\mu_h > \mu_s$, owing to fast heterodiffusion, a small number of large-size islands are formed in the first layer, so that the low-mobility atoms deposited on them do not have enough time to migrate to the first layer and the second layer starts to grow very early ($\xi_{1c} = 0.25$). Thus, the effect of two mobilities can lead either to the smoother ($\mu_h < \mu_s$) or rougher ($\mu_h > \mu_s$) initial growth impeding or stimulating the layer-by-layer to smooth multilayer transition. With an increase in barrier height and in the (relative) difference of mobilities, this effect manifests itself even more distinctly. For example, for the transition from the smooth-multilayer to 3D regime ($\mu_s = 10^9$, $\omega = 0.01$), the second layer arises rather early in the case of homoepitaxy ($\xi_{1c} = 0.35$); whereas in the case of heteroepitaxy with $\mu_h = 10^6 < \mu_s$, the second layer manifests itself at the nearly filled ($\xi_{1c} = 0.95$) first layer. At the same time, the rough growth takes place almost from the very beginning ($\xi_{1c} = 0.09$) for $\mu_h = 10^{12} > \mu_s$.

The results obtained also clarify the evolution of the nucleation kinetics $N_k(\xi)$ in consecutive layers, which is poorly known in contrast to submonolayer kinetics. In the regime of smooth homoepitaxial growth (layer-by-layer and smooth multilayer), $N_k(\xi)$ varies at first, but gradually tends to the steady-state form. As can be seen from the figure (in the center), the $N_k(\xi)$ curves move downward with increasing layer number because, in contrast to the first layer, for which the whole substrate serves as the feeding zone, for all the next layers, it is formed in the process of growth, so that the area allowed for the nucleation is smaller. In the case of heteroepitaxy, the $N_k(\xi)$ curves tend to the same limiting curve $N(\xi)$ determined by parameters $\mu_s$ and $\omega$ from

above (from below) owing to the high (low) density of islands in the first layer for $\mu_h < \mu_s$ ($\mu_h > \mu_s$). The obtained curves $N_1(\xi)$ are excellently fitted by the well-known scaling law for submonolayer kinetics (cf., [4, 10]):

$$N_1(\xi) = \mu^{-p} f(\xi) \tag{8}$$

with the exponent $p = \frac{i^*}{i^* + 2}$. Therefore, in the case under consideration, we have $i^* = 1$ with $p = 1/3$ and a certain universal unimodal function $f(\xi)$ with a maximum at $\xi = 0.07$. The amplitude and width of limiting curves $N(\xi)$ depend on $\mu_s \equiv \mu$ and $\omega$, but, as analysis shows, they can also be represented in universal scaling form:

$$N(\xi) = \mu^{-p}\omega^q\varphi(\xi) \tag{9}$$

with the same exponent $p = 1/3$, exponent $q = 0.18$, and another unimodal filling function $\varphi(\xi)$ having a peak at larger $\xi$ ($\xi = 0.2$).

Thus, the model allows us to estimate quantitatively the effects of two different mobilities in the case of heteroepitaxy, which can play a substantial role in the early stages important for the growth of ultrathin films ($\delta$-layers as well as tunneling structures and heterostructures in nanoelectronics).

## REFERENCES


1. J. Villain, J. Phys. I (France) **1**, 19 (1991).
2. J. A. Meyer, J. Vrijmoeth, H. A. van der Vegt, *et al.*, Phys. Rev. B **51**, 14790 (1995).
3. M. Siegert and M. Plischke, Phys. Rev. E **53**, 307 (1996).
4. J. G. Amar and F. Family, Phys. Rev. B **54**, 14071 (1996).
5. K. Kyuno and G. Ehrtich, Surf. Sci. **394**, 179 (1997).
6. *Epitaxial Growth: Principles and Applications Symposium, San Francisco, 1999* (Materials Research Society, Warrendale, 1999), Mater. Res. Soc. Symp. Proc., Vol. 570.
7. V. I. Trofimov and V. G. Mokerov, Dokl. Akad. Nauk **367**, 749 (1999) [Dokl. Phys. **44**, 527 (1999)].
8. V. I. Trofimov and V. G. Mokerov, Comput. Mater. Sci. **17**, 510 (2000).
9. J. A. Venables, G. D. T. Spiller, and M. Hanbuken, Rep. Prog. Phys. **47**, 399 (1984).
10. V. I. Trofimov and V. A. Osadchenko, *Growth and Morphology of Thin Films* (Énergoatomizdat, Moscow, 1993).


*Translated by V. Bukhanov*

*Doklady Physics, Vol. 45, No. 12, 2000, pp. 647–648. Translated from Doklady Akademii Nauk, Vol. 375, No. 5, 2000, pp. 609–610.*
*Original Russian Text Copyright © 2000 by Gergel', Mokerov.*

**PHYSICS**

# Enhancement of Operation Speed in Field-Effect Transistors Using Channel Profiling

**V. A. Gergel' and Corresponding Member of the RAS V. G. Mokerov**

Received July 13, 2000

The enhancement of differential transconductance and operation speed of field-effect transistors is one of the main lines in development of microelectronic technology. This enhancement comes about through minimization of the device channel length using the ultimate potentialities of the lithographic process and the implementation of materials with high charge-carrier mobility (High Electron Mobility Transistor—HEMT technology). The current level of technology makes it possible to attain a minimum channel length $L_g \approx 0.1$–$0.2$ μm and a maximum electron mobility $\mu \sim 10^5$ cm$^2$/(V s$^{-1}$) at $T = 77$ K and $\sim 10^4$ cm$^2$/(V s) at $T \simeq 300$ K (in two-dimensional electron gas at a heterocontact). The ultimate frequency $f_T = \frac{1}{4\pi}\frac{\mu V}{L^2}$ would be as high as several thousand gigahertz for characteristic operating voltages $V = 1$ V, thereby far exceeding the requirements of developers of up-to-date and future systems for data transmission and processing. However, the Joule heating of electrons at high electric fields ($\sim 10^5$ V/cm) in the device channel reduces the effective electron mobility to approximately $\sim 10^2$ cm$^2$/(V s) and, consequently, the ultimate frequency to 150–180 GHz. At first glance, the fundamental implications of this lowering of the mobility at high fields and the difficulties preventing significant reduction of the channel length through radical improvement in the quality (spatial resolution) of the lithography restrict the operating speed of the field-effect transistor to a level of several hundred gigahertz.

The previous discussion is related to conventional transistor technology where the parameters of the subgate region are uniform along the channel length. However, we now assume that a series of local unconnected regions with high conductivity (electron concentration) in the transistor channel can be formed. In this case, the channel will be an array of alternating high-resistance and low-resistance regions of nearly equal length $L$ (approximately 10–20 nm). It is obvious (from the condition of current conservation) that the electric field in the channel of such a transistor oscillates in accordance with the ratio of electron concentrations; i.e., high electric field $E_1$ in the high-resistance regions and low field $E_2$ in the low-resistance regions $\left(\frac{E_1}{E_2} = \frac{n_2}{n_1}\right)$ will alternate in the manner qualitatively represented in Fig. 1. Now, we recall a feature of electron Joule heating in semiconductors that is of importance to us: electrons are not instantaneously heated to the quasi-steady-state temperature $T = T_0 + \mu E^2 \tau_0$ (where $T_0$ is the steady-state value of the electron temperature). The heating requires a so-called energy relaxation time $\tau_0 \simeq 10^{-12}$ s, during which the drifting electrons pass a distance $L_T = \mu E \tau_0$. It turns out that in choosing a sufficiently high concentration of electrons $n_2$ in the low-resistance inclusions ($n_2 > 10 n_1$), one can ensure the validity of the following set of inequalities: $L_{T1} > L > L_{T2}$. It is easy to understand that in this situation, the electrons passing across the high-resistance region do not have enough time to be heated to high quasi-steady-state temperature values $\mu E_1^2 \tau_0$ which correspond to the high field $E_1 \simeq 2\frac{V}{L}$.

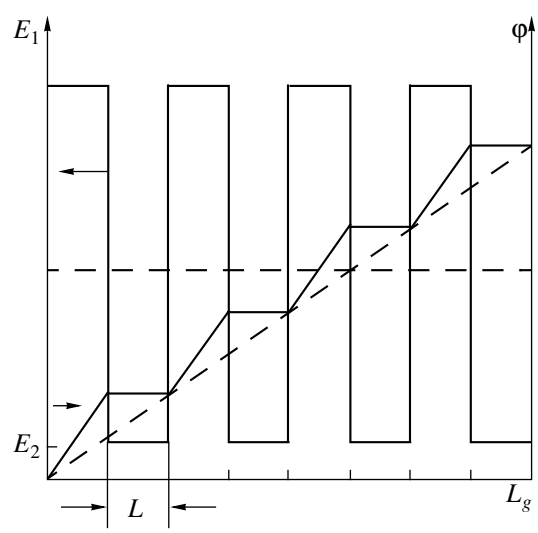


**Fig. 1.** Distributions of voltage and electric field in the profiled-channel transistor; dashed lines correspond to the distributions in a uniform channel.

*Institute of Radio Engineering and Electronics, Russian Academy of Sciences, Mokhovaya ul. 11, Moscow, 103907 Russia*

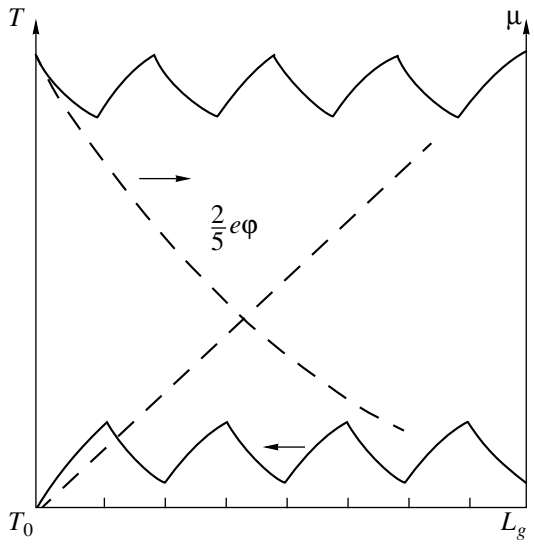


**Fig. 2.** Distribution shapes of the electron temperature and mobility in the profiled-channel transistor.

Here, they gain a rather small thermal energy $\frac{2V}{5\nu}$, where $\nu$ is the number of low-resistance inclusions in the profiled channel under discussion. On the other hand, when passing across the low-resistance region, the electrons have time to be cooled to lower quasi-steady-state temperature values $T_0 + \mu E_2^2\tau_0$, which slightly exceed the steady-state value $T_0$. Thus, the motion of electrons in the profiled channel under consideration, with a strongly oscillating electric field, will be characterized by a relatively low mean electron temperature $T = T_0 + \mu E_2^2\tau_0 + \frac{V}{5\nu}$ with insignificant $\left(\sim\frac{V}{5\nu}\right)$ oscillations (Fig. 2). This ensures a high constant value of electron mobility along the entire channel length. Consequently, the operation speed (ultimate frequency) of such a transistor will attain a level of several thousand gigahertz. This is the basic idea of the present paper.

The suggested idea is entirely viable. It is well known that the implementation of such basic operations of microelectronic technology as laser annealing, ion etching, and molecular-beam epitaxy, can give rise to the formation of either "point" or "filamentary" spatial structures with enhanced carrier concentrations at the surface of the semiconductor layers. In the literature, both methods that prevent the formation of such spatial structures and their possible application are widely discussed. In this connection, we can also mention studies of filamentary structures aiming to reveal the features of electrical conductance inherent in one-dimensional quantum objects and the more successful applications of so-called quantum dots in semiconductor lasers [1]. It is clear that the same methods, e.g., molecular-beam epitaxy of heterostructures, can ensure the formation of the quasi-classical many-electron dot structures or filamentary structures needed for the implementation of our idea.

## REFERENCES

1. N. N. Ledentsov, V. M. Ustinov, V. A. Shchukin, *et al.*, Fiz. Tekh. Poluprovodn. (St. Petersburg) **32**, 385 (1998) [Semiconductors **32**, 343 (1998)].

*Translated by T. Galkina*

*Doklady Physics, Vol. 45, No. 12, 2000, pp. 649–652. Translated from Doklady Akademii Nauk, Vol. 375, No. 6, 2000, pp. 754–757.*
*Original Russian Text Copyright © 2000 by Mokerov, Fedorov, Velikovskiĭ, Shcherbakova.*

**PHYSICS**

# A Novel Quantum-Dot Heterostructure Transistor

**Corresponding Member of the RAS V. G. Mokerov, Yu. V. Fedorov, L. É. Velikovskiĭ, and M. Yu. Shcherbakova**

Received July 27, 2000

## INTRODUCTION

Semiconductor heterostructures with quantum dots (QDs), which are often considered to be artificial atoms, are of interest both for pure science and in application (i.e., for instrumentation). The most promising technology of their production is based on heteroepitaxial growth by the Stranski–Krastanov mechanism, when the epitaxial layer grows at the substrate which is lattice-mismatched with the layer and QTs are formed when the layer thickness exceeds a certain critical value [1–3]. Although a lot of papers on the structural and optical properties of QTs have been published in recent years, to date, the electron transport in these systems, in particular, under the effect of strong electric fields, is far from being well understood. Data on QD-based transistors are also absent.

In this paper, we study the optical and transport properties of two-dimensional (2D) electron gas in modulation doped InAs *N*-AlGaAs/GaAs/InAs/GaAs/InAs/GaAs heterostructures containing QDs built into the instrument channel. We also study the characteristics of transistors based on these structures.

## MOLECULAR-BEAM EPITAXY OF MODULATION-DOPED HETEROSTRUCTURES WITH QDs

In this paper, we study two types of heterostructures with QDs (S1 and S2) grown by molecular-beam epitaxy on semi-insulating GaAs(100) substrates. Their cross section is schematically shown in Fig. 1. This cross section involves an undoped buffer GaAs layer 0.5 μm thick and two very thin InAs layers separated by an undoped GaAs spacer layer 5.6 nm thick. For the S1 samples, the thickness of InAs- and GaAs-spacer layers was equal to 1.07 and 5.6 nm, respectively. For the S2 samples, the corresponding values of thickness were 0.7 and 3.7 nm. In both cases, two QD layers of different size and density were formed. Then, after growing a second GaAs spacer layer 5.6 and 3.7 nm thick for the S1 and S2 samples, respectively, an undoped $Al_{0.2}Ga_{0.8}As$ spacer layer 10 nm thick, a δ(Si)-doped layer, and an undoped barrier $Al_{0.2}Ga_{0.8}As$ layer 35 nm thick were grown. The formation of the heterostructures was completed by the growth of an undoped GaAs layer 6 nm thick and an $n^+$ GaAs contact layer 40 nm thick doped with silicon (with a dopant density of $3 \times 10^{18}$ cm$^{-3}$). Pseudomorphic strained AlGaAs/$In_yGa_{1-y}As$/GaAs heterostructures without QDs were grown as reference samples; these samples had the same mean molar content of In, $y = 0.17$, and the thickness of the $In_{0.17}Ga_{0.83}As$ layer was 12 nm.

## OPTICAL AND ELECTRICAL PROPERTIES OF THE HETEROSTRUCTURES WITH QDs

An atomic-force microscopy image of the surface of the S1 sample is shown in Fig. 2. For this sample, the molecular-beam epitaxy growth was terminated imme-

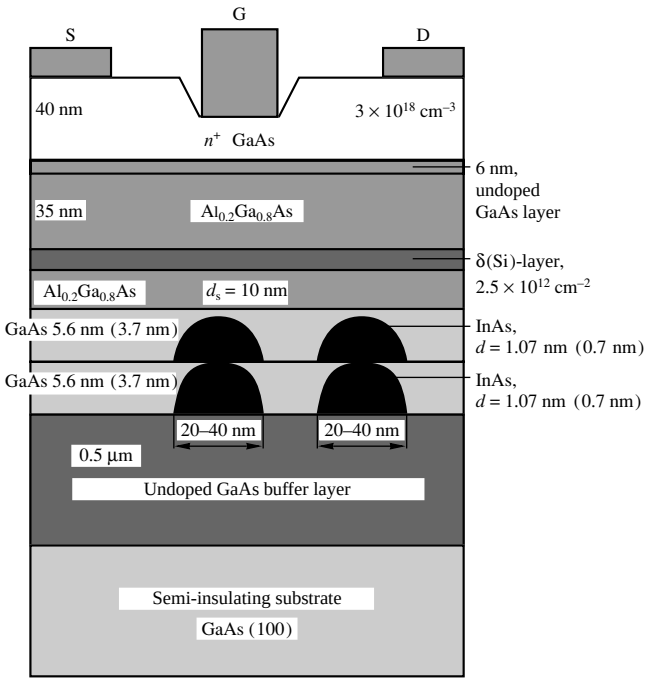


**Fig. 1.** Cross section of the modulation-doped heterostructures with QDs.

*Institute of Radio Engineering and Electronics, Russian Academy of Sciences, ul. Mokhovaya 11, Moscow, 103907 Russia*

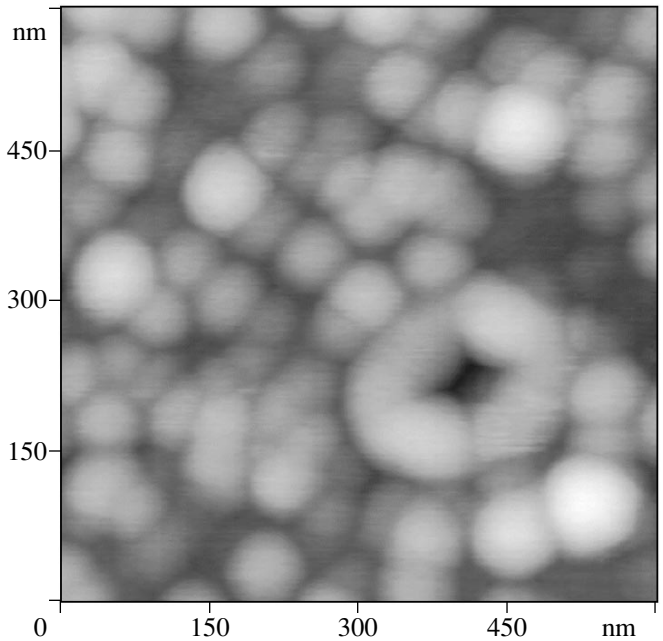


**Fig. 2.** Atomic-force microscopy image of the S1 sample surface.

diately after the deposition of the second InAs layer had occurred. It is clear from Fig. 2 that the mean size of QDs and their density are ~40 nm and $3 \times 10^{10}$ cm$^{-2}$, respectively. The formation of QDs in the S1 and S2 samples was also confirmed by photoluminescence measurements at 77 K. For these samples, broad photoluminescence bands characteristic of QDs were observed at photon energies $h\nu$ = 1.27 and 1.25 eV, respectively. On the other hand, in the reference SR sample, where QDs are absent, two narrow lines (at $h\nu_1$ = 1.356 eV and $h\nu_2$ = 1.400 eV, respectively) were observed in the photoluminescence spectrum instead of a broad band. This is characteristic of modulation-doped quantum wells; these lines correspond to the optical transitions between two occupied electron subbands and hole states [4, 5].

The results of the Hall-effect-based measurements of the mobility $\mu_{2D}$ and density $n_{2D}$ of 2D electrons in various samples are presented in the table. It follows from the table that the introduction of QDs into the instrument channel (samples S1 and S2) causes a decrease in electron mobility $\mu_{2D}$ for both of them and a substantial lowering of the electron concentration $n_{2D}$ in the S1 sample as compared to the reference sample SR. In the S1 samples, evidently, trapping of the majority of electrons at deep levels in the QDs takes place. In the S2 samples grown with a smaller amount of deposited InAs, the lateral sizes of the QDs can be smaller and their deep levels, are, consequently, less deep. As a result, a smaller number of electrons can be trapped by these QDs. The lower values of electron mobility in the S1 and S2 samples in comparison with the SR sample provide a direct indication of the specific potentials related to the introduction of InAs QDs into the instrument channel. These potentials efficiently scatter the 2D electrons. The electron charges trapped by the QDs and the elastic stresses arising around each QD can be responsible for these scattering potentials.

Results of the Hall-effect-based measurements of $\mu_{2D}$ and $n_{2D}$

| Samples | $\mu_{2D}$, cm$^2$/(V s) | | $n_{2D}$, cm$^2$ | |
|---|---|---|---|---|
| | $T$ = 77 K | $T$ = 300 K | $T$ = 77 K | $T$ = 300 K |
| SR | 10108 | 4500 | $8.2 \times 10^{11}$ | $9 \times 10^{11}$ |
| S1 | 3000 | 2852 | $1 \times 10^{11}$ | $6 \times 10^{10}$ |
| S2 | 1500 | 1000 | $8.3 \times 10^{11}$ | $8.05 \times 10^{11}$ |

## ELECTRON TRANSPORT IN HETEROSTRUCTURES WITH QDs UNDER THE EFFECT OF A STRONG ELECTRIC FIELD

If a certain portion of 2D electrons in the S1 and S2 samples (especially in S1) is trapped by QDs, they, naturally, cannot participate in low-field electron transport. However, if this is actually the case, their contribution should manifest itself in electron emission from the QDs under the effect of a strong electric field. To perform such experiments, special transistor structures were produced for the S1 and S2 samples, such as shown in Fig. 1, but without the gates. The distance between the ohmic contacts corresponding to the source and drain was 2 μm. Their current–voltage characteristics (*I–V* curves) are shown in Fig. 3. As is seen in Fig. 3, in contrast to the "classical" structures of field-effect transistors, the *I–V* curves of the heterostructures with QDs have an anomalous two-step shape. The two steps on these *I–V* curves are related to the contributions of two different types of electron states: mobile 2D electrons (as in conventional field-effect transistors) are responsible for the first step, which corresponds to the saturation of their drift velocity and electrons localized at QDs. The latter are responsible for the second step. They contribute to the electron transport only under the effect of a strong electric field $F$ exceeding a certain threshold value $F_{th}$. This contribution arises due to the electron emission from QDs, which is induced by this field. It is clearly seen in Fig. 3 (curves *b* and *c*) that a decrease in the distance between the surface of the sample and the transistor channel due to the etching-off of a certain surface layer leads to a decrease in or even vanishing of the currents in the vicinity of the first step. This is, evidently, caused by the channel depletion in the mobile charge carriers owing to the enhancement of the surface-potential effect. In this case, due to the presence of only the sec-

ond step, the *I–V* curves exhibit a clearly pronounced threshold behavior.

## CHARACTERISTICS OF TRANSISTORS BASED ON MODULATION-DOPED HETEROSTRUCTURES WITH QDs

Field-effect transistors with gate lengths ranging from 0.3 to 0.4 μm were manufactured using samples of S1 and S2 heterostructures (Fig. 1). The *I–V* curves of these transistors are shown in Fig. 4. This figure demonstrates that even at zero bias voltage across the gate, we have a substantial shift of the second current step toward lower values of voltages compared to the "gateless" transistors. This effect can be explained by the redistribution of the electric field in the instrument channel. Actually, the majority of electrons in the S1 samples is localized at deep levels in the QDs, hence their concentration should be insignificantly controlled by the gate voltage. Owing to this effect, the potential distribution along the gate length should remain unchanged. In this case, the main part of the voltage applied between the source and drain should drop only across gap $d_{gd}$, between the drain and the gate edge nearest to it. Since distance $d_{gd}$ is less than that between the source and drain $d_{sd}$, the electric field in the actual operating region (i.e., in the gap $d_{gd}$) should be larger than the mean electric field in the gateless transistor. Therefore, threshold voltage $U_{th}$ should decrease compared to the gateless transistors. It follows also from Fig. 4 that saturation current $I_{dss}$ for the second step is in fact independent of the gate voltage $U_g$; however, the threshold voltage $U_{th}$ for this step is very efficiently controlled by voltage $U_g$. These characteristics qualitatively differ from those intrinsic to classical field-effect transistors, for which only the electron density and, consequently, the saturation currents are governed by voltage $U_g$. Thus, the data in Fig. 4 show that in the transistors under study, the concentration of electrons participating in the strong-field transport is independent of $U_g$, whereas the threshold voltage $U_{th}$ needed for electron emission from the QDs decreases when $U_g$ becomes more negative. Thus, in this case, instead of "blocking" the transistor for negative values of $U_g$, as occurs in all field-effect transistors, in the QD-based devices, drain current $I_d$ even increases in the range of low $U_d$ voltage. The observed decrease in the threshold voltage $U_{th}$ is explained by the increase in the effective field $d_{gd}$ in the gap.

The value of the threshold electric field $F_{th}$ needed in order to initiate electron emission from the deep levels in a QD can be determined from the *I–V* curves of the gateless devices:

$$E_{th} = \frac{U_{th}}{d_{sd}} = 4 \times 10^4 \text{ V/cm}.$$

Using the value of $F_{th}$, one can also estimate the effective depth (the energy of position) of occupied electron levels $E_{QD}$ in QDs:

$$E_{QD} = eE_{th}d_{QD} = 160 \text{ meV}. \quad (1)$$

Here, $d_{QD}$ = 40 nm is the lateral QD size. The maximum relative transconductance $g_m$ of the transistors under study was also determined from the curves in Fig. 4 in the range of low voltages $U_d$, i.e., where currents $I_d$ are controlled by the bias voltage $U_g$ across the gate: $g_m \cong$ 500 m S/mm. In this case, one should expect the operating capacitance of these transistors not to be large. The relatively large transconductance and the expected small capacitance of these devices suggest that they are rather promising for high-frequency applications.

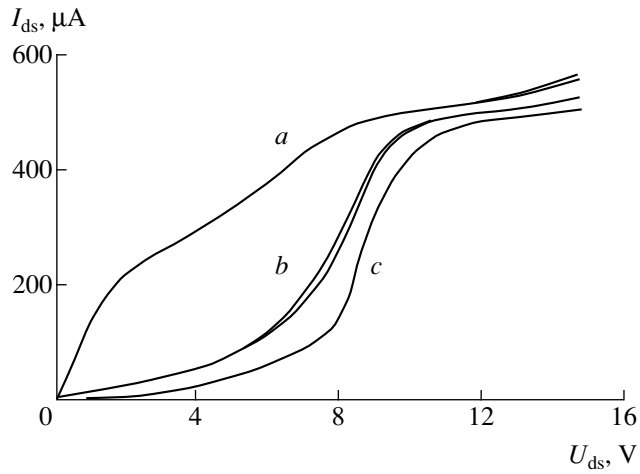


**Fig. 3.** *I–V* curves in a high electric field for heterostructures containing QDs (S1 sample) with the drair–source distance $d_{sd} \cong 2$ μm: (*a*) for the initial sample, (*b*) and (*c*) after additional etching of its surface layer.

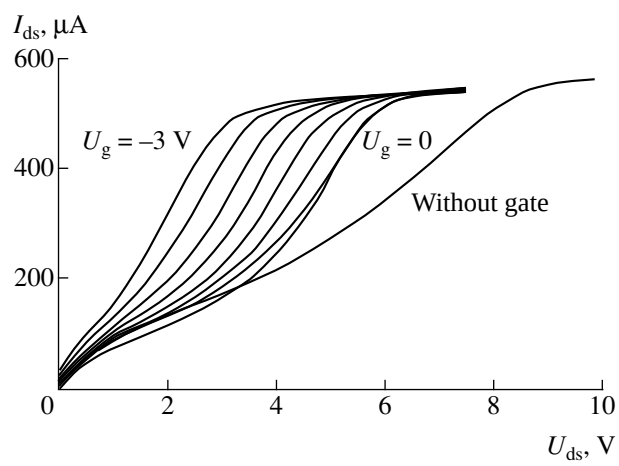


**Fig. 4.** *I–V* curves of the QD-based heterostructure transistors with the gate length $L_g$ = 0.35 μm for various values of the gate voltage $U_g$. The passage from one curve to another corresponds to the steps in the $U_g$ change equal to –0.5 V.

## CONCLUSION

In conclusion, we note that the transistors under study, which are based on modulation-doped heterostructures with QDs, differ basically from all known field-effect transistors, e.g., high electron mobility transistors (HEMTs). Their unusual characteristics stem from the fact that the charge carriers in them are "hot" electrons, i.e., electrons which have an energy higher than the depth characterizing the position of the occupied electron states in QDs. Therefore, they can be considered as a novel type of device based on hot electrons. Due to their high transconductance and small capacitance, these devices can turn out to be very promising for high-frequency applications.

## REFERENCES

1. D. Leonard, K. Pond, and P. M. Petroff, Phys. Rev. B **50**, 11 687 (1994).
2. J. M. Moison, F. Houzay, F. Barthe, *et al.*, Appl. Phys. Lett. **64**, 196 (1994).
3. G. S. Solomon, J. A. Trezza, and J. Harris, Appl. Phys. Lett. **66**, 3161 (1995).
4. J. Pozela, V. Jucine, A. Namajinas, *et al.*, J. Appl. Phys. **82**, 5564 (1997).
5. V. G. Mokerov, Yu. V. Fedorov, A. V. Guk, and Yu. V. Khabarov, Dokl. Akad. Nauk **362**, 335 (1998) [Dokl. Phys. **43**, 565 (1998)].

*Translated by T. Galkina*

*Doklady Physics, Vol. 45, No. 12, 2000, pp. 653–656. Translated from Doklady Akademii Nauk, Vol. 375, No. 6, 2000, pp. 758–761.*
*Original Russian Text Copyright © 2000 by Popryadukhin.*

**PHYSICS**

# The Revised Neoclassical Plasma Theory

**A. P. Popryadukhin**

Presented by Academician Yu.V. Gulyaev July 24, 2000

Received July 24, 2000

The neoclassical diffusion theory [1] appeared in the late 1960s. In this theory, a first attempt was made to explain the poor plasma confinement outside the framework of the Bohm theory based on the allowance for instabilities leading to turbulence. In the years following, the neoclassical theory was further developed [2, 3], and, nowadays, this is the theory that provides the best theoretical description of transport phenomena in plasma of toroidal magnetic traps. However, to date, there exists a significant discrepancy between calculated and experimental data. For ions, the disagreement factor is about three, which is assumed to be inessential. For electrons, this factor, especially as related to heat conductance, is on the order of 10 to 100, i.e., is considerably higher. Since no more adequate confinement theory exists, we can say that the basic incomprehensible fact is the quantitative misfit in the values of transport factors. As the dimensions of both stellarators and tokamaks became larger, the confinement quality was improved, and its adequate description is now given by the neoclassical theory rather than by the Bohm theory. This progress, in fact, did not succeed in explaining the phenomenon. When designing small-scale stellarators in the early 1960s, the confinement in the zero-current regime was assumed to improve in comparison with that in tokamaks, since under these conditions, no additional classes of current instabilities appeared. At the same time, the lower the number of possible types of instabilities, the better the confinement. The experiments carried out with the TOR-1 and TOR-2 stellarators in the Lebedev Physics Institute failed to confirm this assumption. In addition, the plasma density in small-scale stellarators was extremely low, namely, more than by an order of magnitude lower than that in tokamaks. A confinement comparable to tokamaks of the same dimensions was further attained with a larger Liven'-2 stellarator in the plasma-current regime. These qualitative discrepancies also call for explanation.

In the zero-current regime, the plasma in stellarators was produced by injecting from plasma guns. In this case, there appeared another puzzling feature of confinement: the lifetime of decaying plasma was inconstant [4]. Initially, when the plasma density was relatively high, the lifetime was short. The confinement time increased to values slightly exceeding the Bohm values at that discharge stage when the density decreased to an extremely low level.

At present, there is one more undesired phenomenon observed in middle-scale and large-scale toroidal confinement facilities, for which an explanation would be of great practical interest, namely, confinement degradation with additional plasma heating.

**1.** Resonant disturbances of magnetic surfaces cause the formation of magnetic islands. In this case, the resonance condition has the form

$$\iota = \frac{i}{2\pi} = \frac{n}{m}, \quad B_{mn} \neq 0, \tag{1}$$

where $\iota$ is the rotation number and $i$ is the rotation transformation angle. For drift trajectories, the closure condition is modified:

$$\iota = \iota_B + \iota_E. \tag{2}$$

The additional term

$$\iota_E = -\frac{cE_r}{v_\parallel B_z}\frac{R}{r} \tag{3}$$

is determined by the electric drift associated with a pinch charge. The fundamental fact is that expression (3) contains the particle-velocity component parallel to the direction of the magnetic field. For the Maxwellian character of the particle distribution, there always exist resonant particles that satisfy condition (1).

It is more difficult to solve the problem of a generalized perturbation $B^*_{mn}$. In [5], it was shown that electric and magnetic disturbances can compensate one another, and in this case, the disturbance in (1) is absent. This occurs when the equipotentials of the electric field coincide with the magnetic surfaces, since in this case, particles drift along the tangent to the magnetic surface. This is a situation that takes place under ideal hydrodynamic equilibrium. In [5], a question was also raised on the mixing of trajectories if disturbances

*Troitsk Institute for Innovation and Thermonuclear Research, Troitsk, Moscow oblast, 142092 Russia*

of the potential take place. We now return to this problem in its simplest formulation.

We consider a right cylinder with a current flowing along its axis (coinciding with the $z$-axis), the terms on the order of $\left(\frac{B_\theta}{B_z}\right)^2$ being ignored. We use helical symmetry to describe the disturbances (only electric-field disturbances are taken into account). In this case, the integral for the drift motion has the form [6]

$$u_0^* = u_0 + \frac{m_p c}{e} v_\parallel, \quad u_0(r) = A_z + \alpha r A_\theta,$$
$$\frac{\partial u_0}{\partial r} = B_z \frac{r}{R}\left(-\iota_B + \frac{n}{m}\right), \tag{4}$$

where $\alpha = \frac{1}{R}\frac{n}{m}$. In the static case under consideration, the longitudinal velocity depends on coordinates $r$ and $\theta_h = \theta - \alpha z$:

$$v_\parallel = \sqrt{v_\parallel' - \frac{2e}{m}(\Phi_0 - \Phi_0' + \tilde{\Phi})}. \tag{5}$$

Furthermore, we expand (4) and (5) into a series, restricting ourselves by terms of the second order in deviations $\Delta r$ from the circumference of the zero approximation corresponding to the absence of disturbance; i.e., $\tilde{\Phi} = 0$. The multiplier at the term $\Delta r$ yields condition (1), and the multiplier at $\Delta r^2$ is proportional to the generalized shear $\vartheta^*$. Equating, at the initial point of the trajectory, the expression obtained and the constant determined by the primed values, we derive the equation for $\Delta r$. We restrict ourselves by the case of simple parabolic profiles for both the current and the potential. Hence, the basic formulas needed in the calculations take the form

$$\iota_B = 2\iota_a\left(1 - \frac{r^2}{2a^2}\right), \quad \iota_E = \frac{\rho_L R}{a^2}\frac{\kappa}{\xi_\parallel'},$$
$$\vartheta_B = -\frac{2r^3}{a^2 R}\iota_a, \quad \vartheta_E = -\frac{r^3}{a^2 R}\frac{\kappa}{\xi_\parallel'^2}\iota_E, \tag{6}$$

where $\kappa = \frac{e\Phi_0}{T_e}$ is the potential at the pinch center, which is normalized to the electron temperature, $\xi_\parallel' = \frac{v_\parallel'}{v_T}$, and $v_T = \sqrt{\frac{2T}{m_p}}$. The maximum particle displacement is determined by the formula

$$\Delta r = \frac{a^2}{\kappa r}\sqrt{\frac{2e\Phi_{mn}}{T\vartheta_{(\cdot)}}}, \tag{7}$$

where the following notation is introduced:

$$\vartheta_{(\cdot)} = \left(\frac{2\iota_a}{\kappa\iota_E} + \frac{1}{\xi_\parallel'^2}\right), \quad \vartheta^* = -\frac{r^3\kappa\iota_E}{a^2 R}\vartheta_{(\cdot)}.$$

In addition, we present the formula for the width of the resonance region:

$$\Delta\xi = \sqrt{\frac{2e\Phi_{mn}}{T}\vartheta_{(\cdot)}}. \tag{8}$$

If the width of this region is large, the individual resonances may overlap, the motion becomes more complicated, and the above consideration is invalid.

In [5], the diffusion coefficient $D$ was estimated by the following method. The diffusion step was taken to be the half-width of the islands in (8), and the effective collision time was assumed to be equal to $\tau_{eff} = \tau_{ii}\Delta\xi^2$. In addition, the smallness of a number of the particles involved in the transport was also taken into account $\left[\frac{\Delta n}{n} = \frac{1}{\sqrt{\pi}}(2\Delta\xi)e^{-\xi_\parallel'^2}\right]$:

$$D = \frac{\Delta r^2}{\tau_{eff}}\frac{\Delta n}{n}.$$

We now consider, as a numerical example, a project of the T-11M small-scale tokamak with intense high-frequency heating which is characterized by the following basic parameters: $a = 19$ cm, $R = 70$ cm, $B = 1.2$ T, $T_e = 2.6$ keV, $T_i = 1.1$ keV. We choose the magnetic surface $\frac{r}{a} = 0.5$ and suppose for it that $\iota_B = 0.7047$ (this number is far from the resonances). Then, at the pinch edge, $\iota_a = 0.4027$ and at the center, $\iota_0 = 0.8054$ ($q_a = 2.483$ and $q_0 = 1.242$). We take $\kappa = 3$ for the dimensionless potential at the center and $T_e = 2.2$ and $T_i = 1.0$ keV for the temperatures on the magnetic surface. Next, we analyze the resonances $\iota = \frac{n}{m} = \frac{1}{1}, \frac{1}{2}, \frac{1}{3}$. The calculation results are given in the table. As is seen, the most dangerous resonance on the surface given corresponds to $\iota = \frac{1}{2}$. In this case, the electric shear is negative and to a large extent compensates the magnetic shear, whereas the displacements are maximal. It is important to verify the collision regime. For the relative half-width $\Delta\xi = \frac{1}{6}$, the effective collision time is by a factor of 36 shorter than the ion scattering time $\tau_{ii}$ defined by the formula

$$\tau_{ii}^* = \frac{3}{4\sqrt{\pi}}\frac{\sqrt{m_i}T_{e\infty}^{3/2}}{e^4\lambda n_i} \tag{9}$$

**Table 1**

| $\iota = \frac{n}{m}$ | $\iota_E = \iota - \iota_B$ | $\xi'_{\parallel} = \frac{\rho_L R}{a^2}\frac{\kappa}{\iota_E}$ | $\vartheta_{(\cdot)}$ | $\frac{e\Phi_{mn}}{T}$, % | $\Delta r$, cm | $D$, $10^3\ \frac{\text{cm}^2}{\text{s}}$ |
|---|---|---|---|---|---|---|
| 1 | 0.295 | 0.750 | 2.69 | 0.52 | 0.88 | 0.72 |
| $\frac{1}{2}$ | –0.202 | –1.082 | –0.46 | 3.04 | 13.64 | 13.64 |
| $\frac{1}{3}$ | –0.371 | –0.596 | 2.36 | 0.59 | 1.00 | 1.16 |

($\tau_i$ = 4.1 ms for $\lambda$ = 15). Nonetheless, for one revolution period of 10 μs, the ions execute more than 10 revolutions and can bypass a significant part of a drift island. The typical neoclassical Galeev–Sagdeev loss channel corresponds to the perturbation harmonic $\frac{n}{m} = 0$, whose consideration in the straightforward model is incorrect.

It follows from the data presented that disturbances of the potential must be small in order to avoid resonance overlap. At the same time, the diffusion coefficients can be fairly large.

**2.** Calculation of the potential is performed for the gas injection within the framework of the one-dimensional model, since the basic effect consists of plasma spreading along the magnetic field.

In the framework of two-fluid hydrodynamics, the equation of motion along the $z$-axis has the form

$$nm_i\frac{dv}{dt} = -\frac{d}{dz}[n(T_i + T_e)]. \tag{10}$$

In the same approximation,

$$E = -\frac{1}{en}\frac{d}{dz}(nT_e). \tag{11}$$

We now take into account the continuity equation

$$nv = \Gamma = \text{const}. \tag{12}$$

Since we consider the problem on the steady flow of the cold plasma from a source with an intensity $\Gamma$ at the point $z = 0$, then using the relationship $dz = vdt$ and replacing the time derivative standing in the left part of equation (1) by the derivative with respect to coordinate $z$, we have

$$\Gamma m_i\frac{dv}{dz} = -\frac{d}{dz}[n(T_i + T_e)].$$

This equation is easily integrated:

$$\begin{aligned} m_i v + \frac{1}{v}(T_i + T_t) &= C = \text{const} \\ &= m_i v_\infty + \frac{1}{v_\infty}(T_{i\infty} + T_{e\infty}). \end{aligned} \tag{13}$$

The subscript "∞" corresponds to the values of physical quantities far away from the source. The values $T_{i\infty}$ and $T_{e\infty}$ correspond to the ion and electron temperatures of the basic plasma, respectively.

After solving Eq. (13) with respect to $v$ and based on (12), we obtain an expression for the plasma density:

$$n = \frac{\Gamma\sqrt{m_i}}{\sqrt{T_{i\infty} + T_{e\infty}} - \sqrt{T_{i\infty} - T_i + T_{e\infty} - T_e}}. \tag{14}$$

Formula (14) describes the density distribution of newly arriving plasma in implicit form. If the density $n_e$ is low compared to the basic-plasma density, the temperature at the point $z$ depends only on the mean time spent by particles to reach this point; i.e., $T_i$ and $T_e$ are time-dependent functions. To obtain the spatial distribution, we may consider the time $t$ as a parameter and calculate $z$ as a time-dependent function by integrating the velocity.

In order to find the time-dependent functions $T_i(t)$ and $T_e(t)$, we use the equation describing the average energy increment for a bunch of tentative particles ($\alpha$) in a medium of field particles ($\beta$) [7]:

$$\frac{d\mathscr{E}_\alpha}{dt} = 4\pi\lambda e^4\frac{n_\beta}{m_\alpha v_\alpha}\left(\frac{m_\alpha}{m_\beta}\mu(x_{\alpha\beta}) - \mu'(x_{\alpha\beta})\right). \tag{15}$$

Here, $\lambda$ is the Coulomb logarithm and $x_{\alpha\beta} = \frac{m_\beta v_\alpha^2}{2T_\beta}$. The ions are assumed to be singly charged. Equation (15) determines the energy variation for tentative particles in the process of collision with the same kind ($\alpha$) of field particles. The energy exchange between particles with strongly different masses is known to be much slower than the same process between particles with identical masses. Therefore, we will take into account the heating of electrons and ions of arriving plasma only by the electrons and ions of the basic plasma, respectively. In the case of $\frac{m_\alpha}{m_\beta} = 1$, Eq. (15) can be

written out in the dimensionless form

$$\frac{dx}{dt} = 6\left(e^{-x} - \frac{\sqrt{\pi}}{4}\frac{\mathrm{erf}(\sqrt{x})}{\sqrt{x}}\right). \quad (16)$$

Here, time is normalized to the time of electron–ion scattering by replacing $m_i$ in (9) with $m_e$. Another approximation consists in the fact that the time dependence of the temperature and energy is assumed to be the same; i.e., $\frac{T_e}{T_{e\infty}} = x$. We denote this function as $\theta(t)$. For ions, the argument of the function is $\alpha t$, where $\alpha$ is the ratio of collision times for the electrons and ions: $\alpha = \sqrt{\frac{m_e}{m_i}}\left(\frac{T_e}{T_i}\right)^{3/2}$. The function $z(t)$ and $e\varphi(t)$ can be found provided that the function $\theta(t)$ is known.

The function $\theta(t)$ can be approximately represented in the form

$$\theta(t) = 1 - e^{-\gamma t}$$

with the fitting coefficient $\gamma = 2.6$.

We also write out the formula for the maximum potential $\varphi_0$ as

$$\frac{e\varphi(0)}{T_{e\infty}} = \varphi_0 = t_i + \frac{1}{2} - \sqrt{t_i(t_i+1)} + \ln\frac{\sqrt{t_i+1}}{\sqrt{t_i+1}-\sqrt{t_i}}.$$

For $t_i = \frac{T_i}{T_e} = 1$, the disturbance of the potential is 130%. In the toroidal system, the disturbance can decrease by several times due to the closure of counter flows.

**3.** This calculation shows that when injecting gas into plasma, the potentials develop, greatly exceeding the admissible potentials that correspond to resonant diffusion, the mixing of trajectories becoming even stronger. Confinement of particles by the electric field, which causes the appearance of electric superbananas, is also possible. Thus, the phenomena listed in the beginning of this paper can be explained by the existence of potentials violating the equipotentialization. The appearance of the new loss channels can, in the first turn, help to improve the quantitative description of the confinement.

In this approach, we can explain experiments associated with plasma decomposition after its injection from guns into a stellarator. Immediately after injection, a trap is nonuniformly being filled and the magnetic surfaces become highly nonequipotential. Therefore, at the initial moment, the diffusion is maximal. As far as the trap is being filled, the nonuniformity of the density tends to zero, the nonequipotentialization decreases, and the additional loss channels are closed. During gas breakdown in tokamaks, plasma is formed uniformly throughout the volume for a short period of time. This fact explains the better confinement in a tokamak, as well as in a stellarator with a nonzero current.

Along with the confinement time $\tau$, we should introduce a characteristic time $\tau_h$ of homogeneous filling. In small-scale stellarators, we have $\tau < \tau_h$, which explains the low plasma density. For larger facilities, an opposite expression is valid: $\tau > \tau_h$. In the case of local heating, disturbances of the potential, which can cause the degradation of the confinement, are possible. With increasing dimensions of a facility, the inequality $\tau > \tau_h$ is enhanced. In this case in particular, the conditions for local methods of heating are improved.

## ACKNOWLEDGMENTS

The author is grateful to É.A. Azizov and I.A. Kovan for their valuable discussions of the study.

## REFERENCES

1. A. A. Galeev and R. Z. Sagdeev, Zh. Éksp. Teor. Fiz. **53**, 398 (1967) [Sov. Phys. JETP **26**, 261 (1968)].
2. L. M. Kovrizhnykh, Nucl. Fusion **24**, 851 (1984).
3. F. L. Hinton and P. D. Hazeltine, Rev. Mod. Phys. **48**, 239 (1976).
4. M. A. Ivanovskiĭ, S. N. Popov, A. P. Popryadukhin, and M. S. Rabinovich, in *Proceedings of the IV International Conference on Plasma Physics and Controlled Nuclear Research, Vienna, 1971*, vol. 3, p. 63.
5. A. P. Popryadukhin, Zh. Tekh. Fiz. **40**, 1839 (1970) [Sov. Phys. Tech. Phys. **15,** 1435 (1971)].
6. A. I. Morozov and L. S. Solov'ev, Dokl. Akad. Nauk SSSR **128**, 506 (1959) [Sov. Phys.–Dokl. **4**, 1031 (1959)].
7. B. A. Trubnikov, in *Problems of Plasma Physics*, Ed. by M. A. Leontovich (Gosatomizdat, Moscow, 1963; Consultants Bureau, New York, 1963), No. 1, p. 98.

*Translated by Yu. Vishnyakov*

*Doklady Physics, Vol. 45, No. 12, 2000, pp. 657–658. Translated from Doklady Akademii Nauk, Vol. 375, No. 4, 2000, pp. 469–471.*
*Original Russian Text Copyright © 2000 by Absalyamov, Mulyukov.*

**TECHNICAL PHYSICS**

# The Stability of Hematite in Small-Size Particles

**S. S. Absalyamov* and Kh. Ya. Mulyukov****

Presented by Academician R.I. Nigmatulin March 02, 2000

Received March 23, 2000

In recent years, the properties of materials having nanocrystalline and submicron-grained structures have attracted widespread attention. These materials significantly differ in their physical properties from those of substances formed by macroscopic crystallites. For example, the materials with nanocrystalline and submicron-grained structures exhibit both improved mechanical parameters (hardness, strength, elastic modulus, etc.) [1] and modified magnetic and electric properties [2]. For example, the transition of ferromagnetic materials to the submicron and nanometer crystallite state is accompanied by changes in such fundamental characteristics of ferromagnets as the saturation magnetization and the Curie temperature [3]. In addition, the solids with submicron- and nanostructures arising under the effect of shear deformation at high pressures are characterized by a significant increase in the rate of physical and chemical processes and by a number of solid-phase reactions, which are impossible in the coarse-grained state. Under pressure, shear deformation is a powerful factor also stimulating the polymerization process in solid monomers [4]. However, the problem of stability of different crystal phases in solids formed by submicron particles is currently far from being well understood. In this connection, we investigated the stability of hematite in submicron-size particles.

In this paper, we study the temperature dependence of saturation magnetization for both coarse- and submicron-grained hematite powder. The submicron-grained powder was produced by shear deformation at Bridgman anvils by their rotation through an angle $2\pi$ under pressure $P = 200$ MPa. We used a single crystal of natural hematite as the host material. $\alpha$-$Fe_2O_3$ hematite has a corundum-type crystal structure and is a weak ferromagnet with a small misalignment of magnetic moments in its sublattices [5].

The grinding of hematite between the Bridgman anvils yields a powder consisting of crystallites of various sizes. Using a special technique, we managed to separate the fraction of hematite with the finest grains.

* *Bashkortostan State University, ul. Frunze 32, Ufa, 450074 Bashkortostan, Russia*

** *Institute of Problems of Metal Superplasticity, Russian Academy of Sciences, ul. Khalturina 39, Ufa, 450001 Bashkortostan, Russia*

The temperature dependence of the hematite saturation magnetization $\sigma_S(T)$ was recorded in a $1.5 \times 10^{-3}$ Pa vacuum in a 240 kA/m magnetic field using an automatic vacuum microbalance [6]. The temperature variation rate was 4 K/min for the measurements of the $\sigma_S(T)$ curves.

The $\sigma_S(T)$ curve for the coarse-grained hematite powder is shown in Fig. 1a. The curve was recorded both on heating and on cooling the sample. Before cooling, the sample was held for 15 minutes at 970 K. As is seen, the heating and cooling curves are identical. The Curie temperature determined by extrapolation of the steepest part of the $\sigma_S(T)$ curve onto the temperature axis equals 948 K, which corresponds to the Curie point in stoichiometric hematite [7].

The $\sigma_S(T)$ curves for the submicron-grained hematite powder recorded on heating (curve *1*) and on cooling (curve *2*) the sample in vacuum are shown in Fig. 1b. Comparison of the curves in Fig. 1 demonstrates that they are different. First, note that the value of $\sigma_S$ for the submicron-grained hematite powder is 30% smaller than that for the coarse-grained state. Second, the shape of the heating and cooling $\sigma_S(T)$ curves is different for the submicron-grained hematite powder and it also does not coincide with the corresponding curve for the coarse-grained sample. On heating the sample, $\sigma_S$ remains constant up to 600 K. Then, it steeply grows and at 750 K attains its maximum value equal to 1.13 A $m^2$/kg. On further increase in temperature, $\sigma_S$ decreases. In the vicinity of 948 K, there is a step in the temperature dependence of $\sigma_S$, but $\sigma_S$ completely vanishes only at 1033 K. Note that the $\sigma_S(T)$ curve for the hematite powder on cooling down to 770 K coincides with the heating curve. Below 770 K, the cooling curve goes above the heating curve. On further decrease in temperature, $\sigma_S$ again grows, and at room temperature, it becomes higher by a factor of 5.7 than $\sigma_S$ for the coarse-grained hematite.

Turning to a discussion of the observed effects, note first that the $\sigma_S(T)$ curves for coarse-grained hematite coincide at heating and cooling. This implies that the coarse-grained hematite is stable in vacuum up to relatively high temperatures. The decrease in $\sigma_S$ for the submicron-grained hematite powder can be related

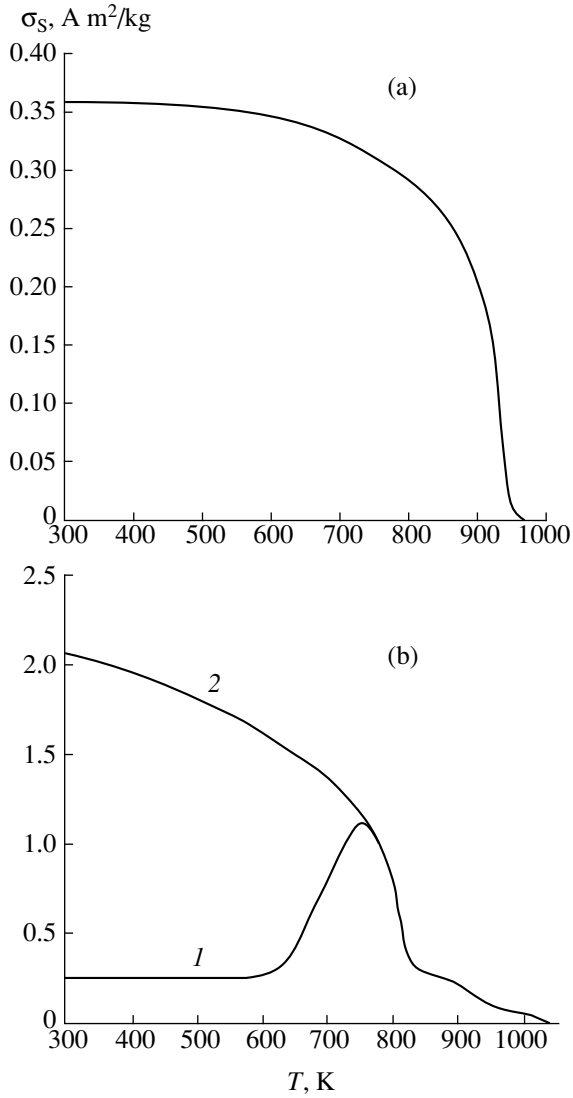


**Fig. 1.** Temperature dependence of saturation magnetization in hematite: (a) in the coarse-grained state; (b) in the submicron-grained state. (*1*) Heating curve; (*2*) cooling curve.

both to the small size of the powder particles and to the crystal lattice defects in the bulk of the particles when the crystal is crushed under high pressure. This assumption is based on theoretical studies [8, 9] demonstrating high sensitivity of the antiferromagnetic order to crystal-lattice defects.

The abrupt increase in $\sigma_S$ and the existence of the peak in the heating curve can be explained by the transformation of a certain part of the hematite powder to magnetite. This is confirmed by the fact that extrapolation of the steep portion in the $\sigma_S(T)$ curve leads to the temperature value being equal to 848 K, which coincides with the Curie point for magnetite. The small step in the $\sigma_S(T)$ curve after the peak is an indication that rather large hematite crystallites exist in the powder. As shown above, these crystallites are stable and do not transform into magnetite. To test the assumption concerning the reduction of small hematite particles to magnetite in vacuum, we measured the temperature dependence of $\sigma_S(T)$ for submicron-grained powder in ambient air. The curve obtained is similar to that shown in Fig. 1a. Thus, in air, even the smallest hematite particles do not transform into magnetite.

Nonzero magnetization, observed after the step (above 848 K), implies that a certain part of the powder (probably, that with the finest grains) is reduced to pure iron at these temperatures. This is confirmed by the fact that magnetization vanishes at 1033 K, and this temperature coincides with the Curie point of iron.

As was already mentioned, after cooling, the saturation magnetization for the submicron-grained hematite powder increases up to 2.08 A $m^2$/kg, i.e., by a factor of 8.3. Estimation based on these data shows that only a small portion (about 1.3%) of the powder transforms into magnetite. Such a small amount of magnetite cannot even be detected by X-ray analysis. The hematite–magnetite transition is likely to occur only in the finest particles. The mean size of the particle determined by a sedimentation technique in distilled water for 24 hours was equal to 0.5 μm. Hence, the major part of the powder consists of larger particles in which hematite remains stable. One could also suggest that on heating in vacuum, hematite is reduced to magnetite not only inside small particles but at the surface of crystallites as well. In this case, however, the complete coincidence of the heating and cooling curves $\sigma_S(T)$ of the coarse-grained sample (Fig. 1a) would not be observed.

Thus, heating of the submicron-grained hematite powder in vacuum leads to partial reduction of the hematite with the formation of both magnetite and iron. Hence, it follows that the $\alpha$-$Fe_2O_3$ hematite in nanocrystallites cannot exist in vacuum at elevated temperatures.

## REFERENCES

1. H. Gleiter, Nanostruct. Mater. **6**, 3 (1995).
2. A. I. Gusev, *Nanocrystalline Materials: Methods of Production and Properties* (Yekaterinburg, 1998).
3. Kh. Ya. Mulyukov, G. F. Korznikova, and S. A. Nikitin, J. Appl. Phys. **79**, 8584 (1996).
4. A. A. Zharov, Usp. Khim. **53**, 236 (1984).
5. S. V. Vonsovskiĭ, *Magnetism* (Nauka, Moscow, 1971; Wiley, New York, 1974).
6. Kh. Ya. Mulyukov, I. Z. Sharipov, and S. S. Absalyamov, Prib. Tekh. Éksp., No. 3, 149 (1998).
7. G. P. Kudryavtseva, V. K. Garanin, V. A. Zhilyaeva, and V. I. Trukhin, *Magnetism and Mineralogy of Natural Ferrimagnetics* (Mosk. Gos. Univ., Moscow, 1982).
8. A. I. Mitsek, Fiz. Met. Metalloved. **64**, 448 (1987).
9. K. Handrich and S. Kobe, *Amorphe Ferro- und Ferrimagnetika* (Akademie, Berlin, 1980; Mir, Moscow, 1982).

*Translated by Yu. Vishnyakov*

*Doklady Physics, Vol. 45, No. 12, 2000, pp. 659–662. Translated from Doklady Akademii Nauk, Vol. 375, No. 5, 2000, pp. 611–614.*
*Original Russian Text Copyright © 2000 by Doroshenko, Kravchenko.*

**TECHNICAL PHYSICS**

# Scattering of Electromagnetic Waves by an Unclosed Circular Cone

**V. A. Doroshenko* and V. F. Kravchenko****

Presented by Academician Yu.V. Gulayev December 27, 1999

Received December 29, 1999

## INTRODUCTION

It is well known that the generation of super-broadband radiation is an important problem in the modern technology of antenna-waveguide engineering. In this case, conical structures are characterized by undirected and super-broadband properties related both to the directivity pattern and consistency. These structures are widely used in radar engineering, communication, and telemetry. In this study, the problem of excitation by an electric radial dipole of a cone with periodic longitudinal slots is considered. Certain cases exhibiting this structure are of independent interest both to theory and application, e.g., a cone with a longitudinal slot and a plane angular cone with two symmetric slots (a model of the V-shaped antenna). The analysis performed in this paper is based on the Kontorovich–Lebedev integral transformation and a method applied in solving the Riemann–Hilbert problem [1–4].

## FORMULATION OF THE PROBLEM

We consider a semi-infinite ideally conductive and infinitely thin circular cone (see figure) with $N$ slots periodically notched along the generatrix of the cone, the cone axis and the cone vertex coinciding with the $0z$-axis and with the origin of coordinates, respectively. The slot structure period $l = \frac{2\pi}{N}$ and the slot width $d$ determine the values of the dihedral angles formed by the intersection of planes passing through the cone axis and the edges of the conical stripes. Then, in a spherical coordinate system $r$, $\vartheta$, $\varphi$ introduced by this manner, the cone is determined by the set of points

$$\Sigma = (r, \vartheta, \varphi) \in R^3 \colon r \in [0, +\infty), \vartheta = \gamma, \varphi \in L,$$

where

$$L = \bigcup_{s=1}^{N} L_s, \quad L_s = \left((s-1)l + \frac{d}{2}, sl - \frac{d}{2}\right).$$

Let the cone be exposed to the time-dependent field of a unit radial source $u^0(\mathbf{r}, \mathbf{r}_0)$ [located at a point $B(r_0, \vartheta_0, \varphi_0)$] which varies by the law $\exp(i\omega t)$. We denote the scattered field by $u^s(\mathbf{r})$. The total field $u = u^0 + u^s$ is assumed to satisfy four conditions: the Helmholtz equation; the Dirichlet boundary condition at both sides of the conical surface:

$$u|_\Sigma = 0;$$

the radiation condition; and the condition of a limited energy value. In this case, the problem has a unique

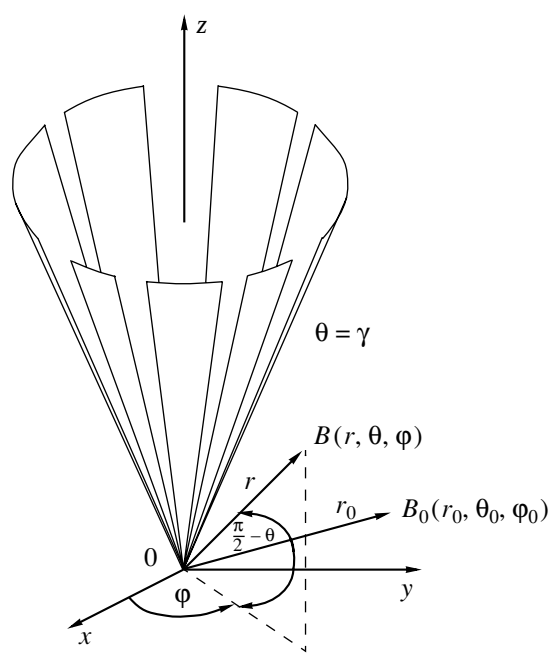


Illustration of cone geometry.

* *Kharkov Technical University of Radio Engineering and Electronics, pr. Lenina 14, Kharkov, 61726 Ukraine*

** *Institute of Radio Engineering and Electronics, Russian Academy of Sciences, ul. Mokhovaya 18, Moscow, 103907 Russia*

1028-3358/00/4512-0659$20.00 © 2000 MAIK "Nauka/Interperiodica"

solution. In solving the problem, we use the Kontorovich–Lebedev integral transformation [1]

$$F(\tau) = \int_0^{-\infty} f(r)\frac{H_{i\tau}^2(kr)}{\sqrt{r}}dr, \quad (1)$$

$$f(r) = -\frac{1}{2}\int_0^{+\infty} \tau\sinh\pi\tau e^{\pi\tau}F(r)\frac{H_{i\tau}^2(kr)}{\sqrt{r}}d\tau, \quad (2)$$

where $H_{i\tau}^2(kr)$ are the Hankel functions and $k$ is the wave number ($\mathrm{Im}k \le 0$). We represent $u^s$ in the form of the Kontorovich–Lebedev integral [2]

$$u^s = -\frac{1}{2}\int_0^{+\infty} \tau\sinh\pi\tau e^{\pi\tau}\sum_{m=-\infty}^{+\infty} b_{m\tau}U_{m\tau}^{(s)}(\vartheta, \varphi)\frac{H_{i\tau}^{(2)}(kr)}{\sqrt{r}}d\tau, \quad (3)$$

$$U_{m\tau}^{(s)} = \sum_{n=-\infty}^{+\infty} x_{m,n}(\tau)\frac{P_{-1/2+i\tau}^{m+nN}(\pm\cos\vartheta)}{P_{-1/2+i\tau}^{m+nN}(\pm\cos\gamma)}e^{i(m+nN)\varphi}. \quad (4)$$

Here, $P_\zeta^m(\cos\vartheta)$ are the Legendre functions and $b_{m\tau}$ and $x_{m,n}$ are the known and desired coefficients, respectively. In (4), the upper and lower signs correspond to the intervals $0 < \vartheta < \gamma$ and $\gamma < \vartheta < \pi$, respectively.

## METHOD FOR SOLVING THE PROBLEM

Taking into account the boundary value condition and the field conjugation conditions in the slots, we obtained a system of dual functional equations of the first kind for $x_{m,n}$:

$$\sum_{n=-\infty}^{+\infty} x_{m,n}e^{inN\varphi} = e^{im_0N\varphi}, \quad \varphi \in L; \quad (5)$$

$$\sum_{n=-\infty}^{+\infty} N(n+\nu)\frac{|n|}{n}(1-\varepsilon_{m,n})x_{m,n}e^{inN\varphi} = 0, \quad \varphi \in CL, \quad (6)$$

where $\Gamma(z)$ is the gamma function and $\zeta = -\frac{1}{2} + i\tau$, $\nu = \frac{m}{N} - m_0$, $-\frac{1}{2} \le \nu < \frac{1}{2}$, and $m_0$ is the integer closest to $\frac{m}{N}$. In the case of $N(n+\nu) \gg 1$, we have an estimate for $\varepsilon_{m,n}$:

$$\varepsilon_{m,n} = O\left(\frac{1}{N^2(n+\nu)^2}\right).$$

From the condition for the finiteness of energy, it follows that $x_{m,n}$ belong to the Hilbert space $l^2$ with the norm

$$\|\xi\|^2 = \sum_{n=-\infty}^{+\infty}(1+|n|)|\xi_n|^2.$$

Furthermore, we transform the system (5), (6) to the form adapted for regularization. We now introduce the coefficients

$$y_{m,n} = (-1)^{n-m_0}\frac{n+\nu}{m_0+\nu}\frac{|n|}{n}(1-\varepsilon_{m,n})x_{m,n}$$

and differentiate Eq. (5) with respect to $\varphi$. Hence, we arrive at the system of equations in the form

$$\sum_{n=-\infty}^{+\infty}\frac{|n|}{n}(1-\eta_{m,n})y_{m,n}e^{in\psi} = e^{im_0\psi}, \quad |\psi| < \delta, \quad (7)$$

$$\sum_{n=-\infty}^{+\infty} y_{m,n}e^{in\psi} = 0, \quad \delta < |\psi| \le \pi \quad (8)$$

with the additional condition

$$\sum_{n=-\infty}^{+\infty}\frac{1}{n+\nu}\frac{|n|}{n}(1-\eta_{m,n})y_{m,n} = \frac{1}{m_0+\nu}, \quad \psi = \pi,$$

where

$$1-\eta_{m,n} = \frac{1}{1-\varepsilon_{m,n}}, \quad \psi = N\varphi - \frac{|\varphi|}{\varphi}\pi, \quad \delta = \frac{\pi(l-d)}{l}.$$

We now represent the operator standing in the left-hand side of the system as a sum of the principal and completely continuous parts. Furthermore, we invert the principal part using the solution to the Riemann–Hilbert problem [3, 4]. As a result, we obtain an infinite system of linear algebraic Fredholm equations of the second kind with respect to $y_{m,n}$:

$$M_\nu(\nu)y_{m,0} = V^{m_0}(\nu) + \sum_{s=-\infty}^{+\infty}\frac{|s|}{s}\eta_{m,s}V^s(\nu)y_{m,s},$$
$$M_\nu(\nu) = \frac{1}{\nu}\frac{P_\nu(-\nu) - P_\nu(-\nu)}{P_{\nu-1}(-\nu) + P_\nu(-\nu)}, \quad (9)$$

$$y_{m,q} = V_{q-1}^{m_0}(\nu) + \sum_{s=-\infty}^{+\infty}\frac{|s|}{s}\eta_{m,s}y_{m,s}V_{q-1}^{s-1}(\nu) + y_{q,0}P_q(\nu), \quad q \ne 0. \quad (10)$$

Here, $\nu = \cos\delta$, while the functions $V^s(\nu)$ and $V_{n-1}^{m-1}(\nu)$ were determined and calculated in [4]. The system (9), (10) is equivalent to functional equations (7), (8) and is obtained as a result of their regularization. The coefficients $y_{m,n}$ are independent of the wave number, which is convenient for clarifying the field behavior both near the cone vertex ($kr \ll 1$) and far from it ($kr \gg 1$), as well as for constructing the solution to the unsteady prob-

lem. The solution to the infinite system of linear algebraic equations exists and is unique. For arbitrary parameters of the problem, this solution can be found by the reduction method. In the case of a semitransparent cone, when the number of slots is large and their width is commensurable to the structure period ($N \gg 1$ and $\delta \ll 1$), the cone with narrow slots ($d/l \ll 1$), and the narrow conical sectors ($\delta \ll 1$), the norm of the matrix operator is smaller than unity, making it possible to apply the iteration method for solving the infinite system of linear algebraic equations.

## THE ANALYTICAL SOLUTION

Using the iteration method and restricting ourselves by the first approximation in the case of a semitransparent cone being defined by the existence of the limit

$$\lim_{\substack{N \to +\infty \\ \delta \to 0}} \left[ -\frac{1}{N} \ln \cos \frac{2}{\delta} \right] = W > 0,$$

we derive the following expression for $u^s$ ($\gamma < \vartheta_0$):

$$u^s = -\frac{1}{2} \sum_{m=-\infty}^{+\infty} e^{im\varphi} \int_0^{+\infty} \frac{\tau \sinh \pi\tau e^{\pi\tau} b_{m\tau}}{1 + 2m(1 - \varepsilon_{m,0})W} \times \frac{H_{i\tau}^{(2)}(kr)}{\sqrt{kr}} \frac{P_{-1/2+i\tau}^{m}(-\cos\vartheta)}{P_{-1/2+i\tau}^{m}(-\cos\gamma)} d\tau,$$

$$\gamma < \vartheta < \pi.$$

This expression is valid for a source and observation points related to each other through the condition $\vartheta + \vartheta_0 > \pi + 2\gamma$, which is caused by the convergence of the above integral and corresponds to the region of the field scattered by the vertex.

This representation for $u^s$ is similar in the case of $0 < \vartheta < \gamma$ as well. On the surface of a semitransparent cone, $u^s$ satisfies the averaged boundary conditions of the form

$$u|_{\vartheta = \gamma + 0} = u|_{\vartheta = \gamma - 0},$$

$$\frac{\partial}{\partial\vartheta} u \bigg|_{\vartheta = \gamma + 0} - \frac{\partial}{\partial\vartheta} u \bigg|_{\vartheta = \gamma - 0} = 2W^{-1} \sin\gamma u|_{\vartheta = \gamma}.$$

In the case of the axisymmetric excitation of the cone ($\vartheta_0 = \pi$, $\varphi_0 = 0$), the expression for $u^s$ can be written out in the form

$$u^s = \frac{\pi^2}{2r_0\sqrt{rr_0}} \int_{-i\infty}^{+\infty} \frac{\mu \Phi_\mu(r, r_0)}{D_\mu \cos\pi\mu} \times [P_{-1/2+\mu}(\cos\gamma)]^2 P_{-1/2+\mu}(-\cos\vartheta) d\mu,$$

$$\gamma < \vartheta < \pi,$$

where

$$D_\mu = \pi P_{-1/2+\mu}(\cos\gamma) P_{-1/2+\mu}(-\cos\gamma) + 2W\cos\pi\mu,$$

$$\Phi_\mu(r, r_0) = \begin{cases} I_\mu(kr) H_\mu^{(2)}(kr_0), & r < r_0 \\ H_\mu^{(2)}(kr) I_\mu(kr_0), & r > r_0. \end{cases}$$

Applying the Cauchy theorem on residues, it is possible to represent $u$ in the form of a residue series with respect to poles of the integrand function. For the semitransparent cone, the spectrum of the boundary value problem consists of roots of the equation $D_\mu = 0$. In the particular case of a semitransparent cone, expressions for these roots can be represented as

(a) $W \ll 1$,

$$\mu_s^\pm = \alpha_s^\pm - \frac{2W\cos\pi\alpha_s^\pm}{\pi \frac{d}{d\mu}[P_{-1/2+\mu}(\cos\gamma) P_{-1/2+\mu}(-\cos\gamma)]\Big|_{\mu = \alpha_s^{\pm +}}} + O(W^2),$$

$$P_{-1/2+\alpha_s^+}(\cos\gamma) = 0, \quad P_{-1/2+\alpha_s^-}(-\cos\gamma) = 0,$$

$$s = 0, 1, 2, \ldots;$$

(b) $W \gg 1$,

$$\mu_s = \frac{1}{2} + s + \frac{1}{2Q}[P_s(\cos\gamma)]^2 + O(Q^{-2}).$$

For the cone with narrow slots ($\vartheta_0 = 0$, $\varphi_0 = 0$), the asymptotic expansion of $u$ in terms of parameter $(1 + \nu) \ll 1$ far away from the slots has the form

$$u = \frac{1}{N}(1 + \nu) \sum_{n=0}^{+\infty} c_n \cos nN\varphi \times \left\{ \sum_{s=0}^{+\infty} \frac{\mu G_\mu(\zeta_s^+, r, r_0)}{\frac{d}{d\mu} P_{-1/2+\mu}} \frac{P_{-1/2+\mu}^{-nN}(-\cos\vartheta)}{P_{-1/2+\mu}^{-nN}(-\cos\gamma)} \bigg|_{\mu = \alpha_s^+} + \sum_{q=0}^{+\infty} \frac{\mu G_\mu(\zeta_q^{nN-}, r, r_0)}{P_{-1/2+\mu}(-\cos\gamma)} \frac{P_{-1/2+\mu}^{-nN}(-\cos\vartheta)}{\frac{d}{d\mu} P_{-1/2+\mu}^{-nN}(-\cos\gamma)} \bigg|_{\mu = \alpha_q^{nN-}} \right\} + O((1 + \nu)^2 \ln(1 + \nu)),$$

$$\gamma < \vartheta < \pi,$$

$$G_\mu(\alpha, r, r_0) = \begin{cases} \left(\frac{kr}{2}\right)^{\mu - \alpha} I_\alpha(kr) H_\alpha^{(2)}(kr_0), & r < r_0 \\ \left(\frac{kr_0}{2}\right)^{\mu - \alpha} H_\alpha^{(2)}(kr) I_\alpha(kr_0), & r > r_0; \end{cases}$$

$$c_n = \frac{\pi i}{r_0\sqrt{r_0 r}} \chi_n, \quad \chi_n = \begin{cases} 1/2, & n = 0 \\ 1, & n \neq 0; \end{cases}$$

$$P_{-1/2+\alpha_s^{nN\pm}}^{-nN}(\pm\cos\gamma) = 0,$$

$$\zeta_s^{nN\pm} = \alpha_s^{nN\pm} - \frac{(1+\nu)}{2N} C_\mu^{nN}\Big|_{\mu=\alpha_s^{nN\pm}} + O((1+\nu)^2),$$

$$C_\mu^{nN} = \frac{(-1)^{nN}\cos\pi\mu}{\pi\dfrac{\Gamma(1/2+\mu+nN)}{\Gamma(1/2+\mu-nN)}\dfrac{d}{d\mu}[P_{-1/2+\mu}^{-nN}(\cos\gamma)P_{-1/2+\mu}^{-nN}(-\cos\gamma)]},$$

$$\alpha_s^{nN\pm}\Big|_{n=0} = \alpha_s^{\pm},$$

where $\alpha_q^{nN+}$ and $\alpha_q^{nN-}$ correspond to the upper and lower signs, respectively, of the Legendre-function argument.

The spectrum of eigenvalues for the boundary value problem and a cone with narrow slots coincides with the set $\{\zeta_s^{nN\pm}\}$ and represents a perturbed spectrum $\{\alpha_s^{nN\pm}\}$ of the Dirichlet boundary value problem for a continuous cone [5]. It is worth noting that the angular dimensions of the conical structure represent the spectral parameters of the boundary value problem, the minimum eigenvalue determining the field behavior near the cone vertex.

In the case of narrow conical sectors ($(1-\nu) \ll 1$), the asymptotic expansion of $u^s$ ($\vartheta_0 = 0$ and $\varphi_0 = 0$) takes the form

$$u^s = \frac{1}{2\ln(0.5(1-\nu))}\sum_{n=-\infty}^{+\infty}(-1)^n e^{inN\varphi}$$

$$\int_0^{+\infty}\tau\sinh\pi\tau e^{\pi\tau}\frac{b_{0\tau}}{F_{i\tau}}\frac{\dfrac{1}{|n|}(1-\eta_{0n})}{\widehat{D}_{i\tau}-\sum\limits_{s\neq 0}\dfrac{1}{|s|}\eta_{0s}}\frac{P_{-1/2+i\tau}^{nN}(\pm\cos\vartheta)}{P_{-1/2+i\tau}^{nN}(\pm\cos\gamma)}d\tau$$

$$+ O\left(\frac{1-\nu}{\ln(0.5(1-\nu))}\right),$$

$$\widehat{F}_{i\tau} = \frac{1}{\widehat{D}_{i\tau}-\dfrac{1}{N}\sum\limits_{s\neq 0}\dfrac{1}{|s|}\eta_{0s}} - \frac{1}{\dfrac{1}{N}\ln(0.5(1-\nu))},$$

$$\widehat{D}_{i\tau} = \frac{1}{N|n|}(1-\eta_{0n})\Big|_{n=0}.$$

The eigenvalue spectrum is determined by roots of the equation

$$\frac{\cos\pi\mu}{\pi P_{-1/2+\mu}(\cos\gamma)P_{-1/2+\mu} - \cos\pi\mu\sum\limits_{s\neq 0}\dfrac{1}{|s|}\eta_{0s}} = \frac{1}{\dfrac{1}{N}\ln(0.5(1-\nu))},$$

which are grouped in the vicinity of zeros of the function $\cos\pi\mu$. The spectrum of the boundary value problem for a single narrow conical sector ($N = 1$) represents a set $\{\mu_s\}_0^{+\infty}$:

$$\mu_s = 0.5 + s - \frac{1}{\ln(0.5(1-\nu))}[P_s(\cos\gamma)]^2 + O(\ln^{-2}(1-\nu)).$$

Thus, we proposed and rigorously substantiated a numerically analytical method for solving the boundary value problem of conical structures with radial slots. This method has the advantage that the intricate three-dimensional boundary value problem is reduced to an infinite system of linear algebraic equations with matrix coefficients independent of the wave parameter. In addition, it turns out to be possible to construct an analytical solution, as was done in [6, 7].

The above method can be used in solving unsteady boundary value problems having a more complicated geometry of the scattering surface. The results of this study were partly reported at the 2nd International Conference on Modern Trends in Computational Physics, July 24–29, 2000, Dubna, Russia [8].

## ACKNOWLEDGMENTS

The authors are grateful to Academician Yu.V. Gulyaev, Corresponding Member of the RAS L.D. Bakhrakh, Corresponding Member of the RAS V.I. Pustovoĭt, professor E.G. Zelkin, and professor Ya.S. Shifrin for their valuable discussions of the results obtained.

## REFERENCES

1. M. I. Kontorovich and N. N. Lebedev, Zh. Éksp. Teor. Fiz. **8**, 1193 (1938).
2. V. A. Doroshenko and V. Sologub, Radiotekh. Élektron. (Moscow) **35**, 2624 (1990).
3. F. D. Gakhov, *Boundary Value Problems* (Fizmatgiz, Moscow, 1963; Pergamon, Oxford, 1966).
4. V. P. Shestopalov, *Method of the Riemann–Gilbert in the Theory of Diffraction and Propagation of Electromagnetic Waves* (Kharkov Univ., Kharkov, 1971).
5. L. B. Felsen and N. Marcuvitz, in *Radiation and Scattering of Waves* (Prentice-Hall, Englewood Cliffs, 1973; Mir, Moscow, 1978), Vol. 2.
6. V. A. Doroshenko and V. F. Kravchenko, Radiotekh. Élektron. (Moscow) **45**, 792 (2000).
7. V. A. Doroshenko and V. F. Kravchenko, Radiotekh. Élektron. (Moscow) **46** (3) (2001).
8. V. A. Doroshenko, in *Abstracts of the 2nd Int. Conf. on Modern Trends in Computational Physics*, July 24–29, 2000. Dubna, Russia, p. 61.

*Translated by Yu. Vishnyakov*

*Doklady Physics, Vol. 45, No. 12, 2000, pp. 663–666. Translated from Doklady Akademii Nauk, Vol. 375, No. 5, 2000, pp. 615–618.*
*Original Russian Text Copyright © 2000 by Skripov, Starostin, Puchinskis.*

**TECHNICAL PHYSICS**

# Heat Transfer and Thermal Fracture of Polymers in Pulsed Processes

**P. V. Skripov, A. A. Starostin, and S. É. Puchinskis**

Presented by Academician V.E. Fortov April 7, 2000

Received April 7, 2000

The behavior of a high-molecular system under the effect of intense local heat release is determined by a number of different factors. These factors are the set of the system's thermal parameters in a given temperature range, the features of thermal fracturing at short characteristic times, and the position of a spinodal (the stability threshold for the condensed phase with respect to cavitation phenomena) in the $p$–$T$ diagram. At high values of both pressure $p$ and temperature $T$, high-molecular systems have a low thermal stability. Therefore, techniques needed for their experimental study must have a sufficiently fast operation speed.

The authors of [1–3] proposed an important approach that provides an opportunity to determine the temperature dependence of the thermal fracture rate in polymers and to evaluate the spinodal temperature based on this dependence. This approach includes the deposition of a thin melt film onto a hot metal substrate and the subsequent recording of the lifetime of the film until its vaporization. However, the technique involving a massive substrate, which was used in [1–3], is quasistatic in essence. Therefore, it cannot resolve the initial stage of thermal fracture in polymers and yields underestimated values of the spinodal temperature (see [4, 5]). It is important to provide a high-speed temporal control of the heater temperature $T(t)$ and to record simultaneously the small variations in the heat flow $q(t)$, which stem from structural transformations in the material.

Our goal was to reveal the features of heat transfer and to resolve the initial stage of thermal fracture in high-molecular systems under the effect of pulsed heat release.

To solve these problems, we developed a technique involving controlled pulsed heating of a thin wire probe. For processes with pulsed heat release characterized by times $t \sim 10^{-5}$–$10^{-3}$ s, this method provides a reliable basis for the study of heat transfer and thermal fracture in small amounts of a material. In the regime of thermal stabilization of the heated probe, we found the range of short-time thermal stability of the polymer melt at elevated temperatures. This type of stability manifests itself in nearly constant values of the thermal parameters. The stability range terminates when the spontaneous vaporization of volatile products occurs, which accompanies the initial stage of thermal fracture. It is found that the characteristic time of the phase transition giving rise to a reproducible signal is much shorter than the characteristic time of a thermal fracture.

The study of the heat transfer in a substance retaining its individual features implies a low degree of thermal fracture of the latter, i.e., a short time duration of the process. We applied the method of pulsed Joule heating using a platinum wire probe for resistance thermometers 20 μm in diameter [6, 7]. This choice of the method was based on its fast response, the small thickness of its warmed-up layer, the possibility of varying pressure in the system, and the convenience in implementing a computer. It is convenient to demonstrate the advantages of the method in the regime of gradual heating of the probe ($\dot{T} \approx$ const) in the polymer melt. In the experiment, we recorded the time dependence of the temperature $T(t)$ at a given impact function, such as probe current $I(t)$. The key point in the heating curve is the moment of spontaneous vaporization $T(t^*) = T^*$ (Fig. 1). Spontaneous vaporization is accompanied by thermal fracture of the substance at fast heating ($\dot{T} \geq 10^5$ K/s). Similar to the spontaneous boiling of low-molecular liquids, the typical response signal recorded in the polymer melt is reproducible and has a narrow time distribution (Fig. 1), i.e., the features intrinsic to a spontaneous mechanism. Consequently, at a sufficiently high average heating rate, the superheating of ordinary and high-molecular liquids is close to its ultimate value corresponding to a high rate of bubble nucleation. The reproducibility of the heat transfer conditions throughout the pulse duration implies that there exists a reproducibility of the relaxation processes responsible for the initiation and development of the phase transition in the high-molecular system.

*Institute of Thermal Physics, Ural Division, Russian Academy of Sciences, ul. Pervomaĭskaya 91, Yekaterinburg, 620219 Russia*

1028-3358/00/4512-0663$20.00 © 2000 MAIK "Nauka/Interperiodica"

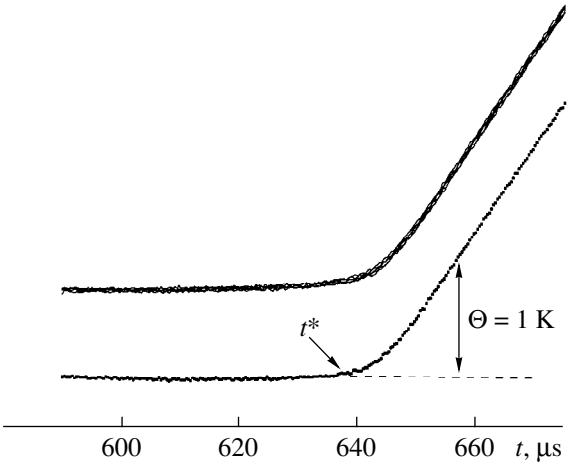


**Fig. 1.** Signal corresponding to the spontaneous vaporization in a polymer melt, which was resolved in the course of probe heating at a rate of 1 K/μs. Θ is the temperature perturbation of the probe related to the vaporization. The upper curve is plotted for the superposition of five successive pulses.

Specific features of the object under study are related to the fact that macromolecules virtually never transform into the vapor phase without decomposition. The absence of potential vapor nuclei in the parent substance determines the appearance of the dependence $T^*(\dot{T})$. Since it is difficult to describe quantitatively thermal fracture of a polymer, we have modeled this dependence using a volatile admixture (carbon dioxide) preliminary introduced into the melt. A relatively low concentration of carbon dioxide ($c \sim 0.01$ wt %) lowers temperature $T^*$ by the value that takes place when decreasing $\dot{T}$ by an order of magnitude. Thus, we can consider the polymer to retain its structure until the onset of vaporization.

We estimate here the effect of the phase transition in the melt on the characteristics of the heat transfer based on the temperature perturbation $\Theta(t - t^*)$ of the probe (Fig. 1) caused by the vaporization. Doing this, we also consider the results of experiments carried out at the given impact function with the probe in vacuum and with a shorter probe in the substance under study. Then, this perturbation can be related to the calculated fraction of the thermally insulated probe surface $s = S_v/S$, where $S_v$ is the surface area covered by vapor with a very low heat conductivity. In our experiments with polymers, the value of $s$ varied within the range 0.005 to 0.05 depending on the pressure and heating regime used.

To study in detail the behavior of a substance in a thermally unstable region, we developed a technique allowing us to specify the necessary regime (of an arbitrary type, in general) of probe heating in the substance. According to it, the heating path $T(t)$, the pressure in the substance, and the concentration of the low-molecular admixture modeling products of the thermal fracture were varied systematically, and the heat flow in the substance was determined. As a result, we obtain the database necessary for analysis of heat transfer and vaporization in a polymer within the range of its thermal instability. In this paper, we consider the regime corresponding to the thermal stabilization of the probe. In processes with rapid temperature variation, this allows us to create the temperature plateau regions $T(t > t_{pl}) = T_{pl}$ at an arbitrary intermediate temperature and to monitor the state of the system at the plateau on the basis of the "instantaneous" thermal properties of the system.

The technique we used is briefly described below. Variation of the probe temperature $T(t)$ is determined by the power consumed for its heating $P(t) = I^2(t)R_T$. Function $I(t)$ determining the current is formed by a computer on the basis of both the model of the process and the results of preliminary experiments. A voltage proportional to the deviation of the function $T(t)$ from the given form is generated at the output of a temperature-monitoring circuit. For the regime of thermal stabilization under consideration, we developed a numerical algorithm for the minimization of the integral deviation of $T(t)$ from the given value $T_{pl}$. An iterating model $I(t)$ is used in order to find its optimum form $I_f(t)$ using two fitting parameters: $I_f(t) = \alpha I(\beta t)$. At the given temperature difference $\Delta T$, $\alpha = f(\lambda)$, and $\beta = f(a)$, where $\lambda(p, T)$ and $a(p, T)$ are the effective values of thermal conductivity and thermal diffusivity of the substance, respectively. According to the conditions of the problem, after the necessary adjustment has been performed, we can generate the additional perturbations $\delta T(t)$ required.

The regime of thermal stabilization in itself includes the stage of rapid heating of the probe ($t_{pl} \sim 10$ μs) up to the chosen temperature $T_{pl}$ and the stage with constant temperature ($t - t_{pl} \sim 10^2$–$10^3$ μs). To find the form of function $I(t - t_{pl})$ at a given probe configuration $(r, l)$, we use the relationship

$$q(t) = \frac{I^2 R_T}{2\pi r l} = \frac{4\lambda T}{\pi^2 r}\int_0^\infty e^{-au^2 t}\frac{du}{u[J_0^2(ru) + Y_0^2(ru)]}, \quad (1)$$

where $J_0$ and $Y_0$ are the Bessel and Neumann functions, respectively. This yields the heat flux at the surface of an ideal heat conducting cylinder with radius $r$ if $T(r) =$ const and the initial temperature of the medium is equal to zero [8]. At the appropriate choices of values of $\lambda$ and $a$, several iterations were sufficient to construct function $I(t)$, providing an acceptable temperature plateau $\left(\frac{|T(t) - T_{pl}|}{T_{pl}} < 10^{-2}\right)$ for $T_{pl} \sim (900 \pm 100)$ K. Note that $\lambda$ and $a$ are the structure-sensitive parameters. The observed correspondence of model (1) to the experimental conditions at $\lambda$ and $a$ independent of the time $t - t_{pl}$ suggests the absence of qualitative structural

changes in the material during the specified time interval. Actually, at a given temperature $T_{pl}$, these parameters undergo significant changes due to pressure variation or dissolution of the low-molecular admixture in the substance.

In a certain range of $T_{pl}$ values, there is a clearly resolved signal related to the spontaneous vaporization, which is similar to that observed in the regime of continuous heating (Fig. 2). Upon increase in $T_{pl}$, the average polymer lifetime at the plateau till the beginning of the phase transition becomes shorter. This result agrees with data on the complete vaporization of thin polymer films from heated substrates [1–3]. Taking into account the small value of the temperature perturbation $\Theta$ and the scale of decrease in $T^*(t^*)$ caused by the dissolution of the model products (Fig. 3), we assume that the time moment of spontaneous vaporization corresponds to the beginning of the initial stage of the thermal fracture. The following conclusions can be drawn based on the results of experiments with polydimethyl siloxanes and caoutchoucs (SKD-KTR oligobutadiene and SKN-10KTR oligobutadiene nitrile):

The polymers are characterized by a short-term thermal stability at temperatures far exceeding those corresponding to the onset of their thermal fracture in the quasi-static process.

The temperature of spontaneous vaporization depends on the heating path and is related to the accumulation kinetics of volatile products and their composition.

The thermal conductivity and thermal diffusivity of the polymers under study decrease with growing temperature and lowering pressure.

We now discuss the experimental results on the spontaneous vaporization of SKN-10KTR oligobutadiene nitrile at different heating regimes (Fig. 3). At each pressure ($p \sim 0.1$–$2.0$ MPa), the growth of temperature $T_{pl}$ in the regime of thermal stabilization or the increase in the heating rate in the linear regime always causes a decrease in the average lifetime of the polymer. For short pulses ($t^* < 100$ μs), only linear heating was used. The shortest time $t^*$ at which the vaporization signal was still resolved was equal to 10 μs at the average heating rate of $8 \times 10^7$ K/s. The value of $T^*$ extrapolated to zero heating time, i.e., to zero degree of thermal fracture, was taken as an approximation for the spinodal temperature of the polymer at a given pressure. According to the concepts developed in [4, 9], the critical polymer pressure is positive and close to zero. Therefore, the spinodal temperature was evaluated for zero pressure. We found that $T_{sp}(p = 0) = 1111$ K for SKN-10KTR and $T_{sp}(p = 0) = 1097$ K for SKD-KTR. In the variation range of the variables ($T \sim 900$–$1100$ K and $t \sim 10$–$1000$ μs), the heat transfer between the pulse-heated probe and the polymer is impeded by spontaneous vaporization, which changes the time dependence of the heat flow by several percent.

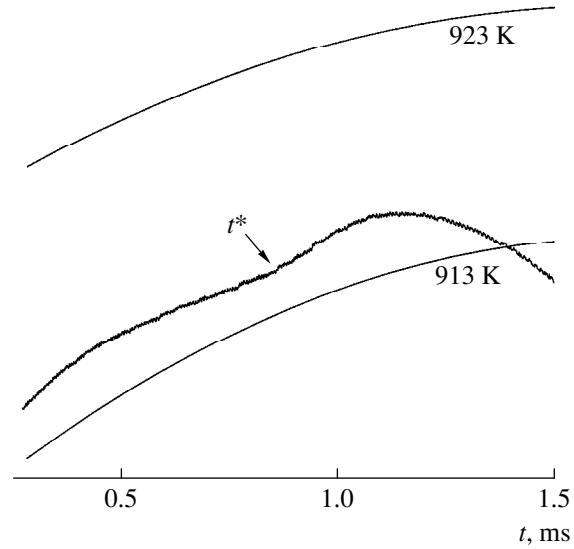


**Fig. 2.** Frequency of the heating curve for probe heating in a polymer melt in the regime of thermal stabilization. The arrow indicates the time moment of spontaneous vaporization. Two calibration isotherms (at 913 and 923 K) show the scale of temperature variation.

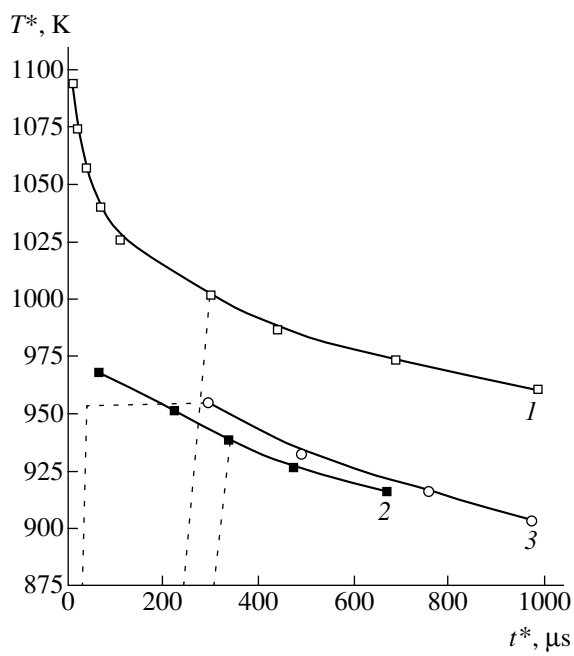


**Fig. 3.** Temperature of spontaneous vaporization for SKN-10KTR caoutchouc (curves *1* and *3*) and for carbon dioxide solution (~1 wt %) in caoutchouc (curve *2*) as a function of the heating time at a pressure of 0.3 MPa. The heating regime is either linear (*1* and *2*) or that of thermal stabilization (*3*) at $t_{pl} \approx 40$ μs. Dashed lines show heating paths.

Thus, we proposed a new approach to the analysis of the behavior of high-molecular systems in processes with rapid temperature variation. The approach turned out to be convenient for application in high-pressure facilities [10].

## ACKNOWLEDGMENTS

This work was supported by the Russian Foundation for Basic Research, projects nos. 98-02-17284 and 00-15-96719.

## REFERENCES

1. K. V. Khishchenko, I. V. Lomonosov, V. E. Fortov, and O. F. Shlenskiĭ, Dokl. Akad. Nauk **349**, 322 (1996) [Phys.–Dokl. **41**, 304 (1996)].
2. K. V. Khishchenko, D. A. Rogatkin, D. N. Yundev, *et al.*, Teplofiz. Vys. Temp. **36**, 227 (1998).
3. O. F. Shlenskiĭ, N. V. Afanas'ev, and A. G. Shashkov, *Thermal Fracture of Materials* (Énergoatomizdat, Moscow, 1996).
4. P. A. Pavlov and P. V. Skripov, Teplofiz. Vys. Temp. **36**, 448 (1998).
5. P. V. Skripov and S. É. Puchinskis, Teplofiz. Vys. Temp. **37**, 614 (1999).
6. P. A. Pavlov, *Boiling Dynamics of Strongly Overheated Liquids* (Sverdlovsk, 1988).
7. D. V. Volosnikov, A. V. Sivtsov, P. V. Skripov, and A. A. Starostin, Prib. Tekh. Éksp., No. 1, 146 (2000).
8. H. S. Carslaw and J. C. Jaeger, *Conduction of Heat in Solids*, 2nd ed. (Clarendon Press, Oxford, 1959; Nauka, Moscow, 1964).
9. P. A. Pavlov and E. D. Nikitin, Dokl. Akad. Nauk **337**, 187 (1994) [Phys.–Dokl. **39**, 497 (1994)].
10. A. A. Starostin, Author's Abstracts of Candidate's Dissertation in Mathematical Physics (Ural. Gos. Tekh. Univ., Yekaterinburg, 2000).

*Translated by Yu. Verevochkin*

*Doklady Physics, Vol. 45, No. 12, 2000, pp. 667–671. Translated from Doklady Akademii Nauk, Vol. 375, No. 6, 2000, pp. 762–766.*
*Original Russian Text Copyright © 2000 by Bulychev.*

**TECHNICAL PHYSICS**

# Determination of the Young's Modulus and Hysteresis by the Indentation Method

**S. I. Bulychev**

Presented by Academician K.V. Frolov March 10, 2000

Received March 10, 2000

The development of nondestructive tests is based on continuously recording an indentation diagram (i.e., the load $P$ applied to an indenter as a function of the dent depth $h$) [1–7]. In this case, the relation between the conventional (recovered) hardness $H$ and nonrecovered hardness $H_h$ becomes vitally important. These quantities are measured through the transverse size of an unloaded dent and the depth $h$ of a loaded dent, respectively. Both further progress in nondestructive testing (based on the indentation method) of the stress–strain and the structural characteristics of materials and in forecasting the reliability and service life for constructions under various operating conditions depend on the possibility of accurately analytically evaluating the relationship between $H$ and $H_h$. This relationship was first established in [3] and depends on the elastic and plastic properties of materials. The allowance for elastic strains in a dent is possible only by accurately measuring the contact elastic modulus $E_r$. A technique for such a method of measuring according to the $P$–$h$ diagram was first proposed in [2] and then developed in a series of papers [3–7]. It was shown in [2] (see Fig. 1) that the slope angle for an initial segment of the unloading branch for the $P$–$h$ diagram is independent of the parameter $m = \frac{w}{w_1}$ determining the mean pressure HM distribution over the dent area. In this case, the accuracy of determining the modulus relates to the measurement accuracy of this angle. The initial part of the unloading branch is close to a straight-line segment [2, 6]; however, more accurate measurements [5] testify to the necessity of allowing for its deviation from linear behavior.

To describe the dent unloading branch, we replace the symbol $h$ with $w$ and set the origin at the final point with coordinates $h_m$ and $P_r = P_m - \Delta P_r$ [4], where $\Delta P_r$ is the load applied to an elastic-contact belt in the periphery of the plastic dent. If the Young's moduli $E$ and $E_i$ of a material and an indenter, respectively, satisfy the condition $E_i \gg E$, then the initial stage of the unloading can be described by the model of an indenter with a flat end, because all the points on the plastic-dent surface are recovered by the same value $\Delta w$ equal to the indenter lift. The area $A$ of the indenter end does not vary and is equal to the area of the unloaded plastic dent. Under purely elastic unloading, the linear dependence

$$\Delta P = E_r d \Delta w_1 \tag{1}$$

holds in the region $P_r$–$\Delta P$. Here, $\Delta P$ is the load decrement; $d = 2a$ is the transverse size of the dent; and $w_1$ is the contact-strain constant providing the minimum elastic strain $w$ for all possible distributions of HM over the area $A$ [1, 3, 4] with the values of HM and $d$ given.

Under unloading, the opposite-pressure distribution is determined by the formula

$$p_x = \frac{\Delta P}{2\pi a^2}. \tag{2}$$

Here, $A = \pi a^2$, with the change $\pi a^2 = (\sqrt{A})^2$ being valid for a square dent with side $\sqrt{A}$, and $p_x$ is the

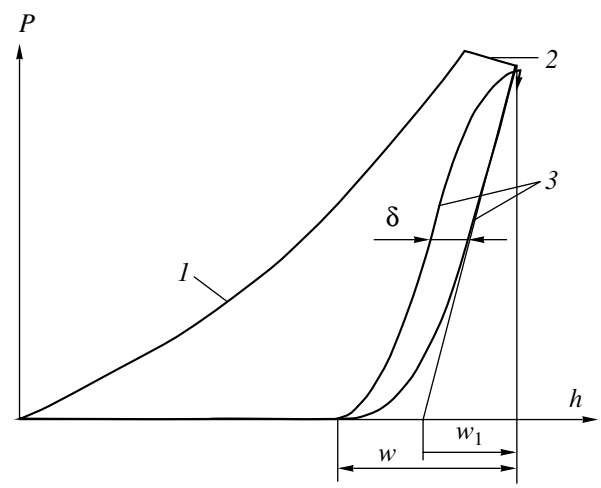


**Fig. 1.** Typical indentation diagram with three branches: (*1*) loading; (*2*) holding under loading; (*3*) unloading and repeated loading accompanied by recording the hysteresis loop of the width δ.

*Moscow State Industrial University,*
*ul. Avtozavodskaya 16, Moscow, 109280 Russia*

opposite pressure on a contour of radius $r$ defined by parameter $x$:

$$x^2 = 1 - \frac{r^2}{a^2}. \quad (3)$$

Formula (2) suggests that no elastic process is realized under the unloading of a plastic dent. After decreasing the load $P_m$ by $\Delta P_r$, the opposite pressure along the perimeter of the plastic dent increases at once to the limiting value $p_x = q$ and opposite plastic strains arise. In the course of unloading, the width of the belt $\Delta r_b = a - r$, in which the pressure is uniform and equal to $q$, increases. The experimental dependence $P(w)$ turns out to be determined by a combination of two processes: an increase in the belt width $\Delta r_b$ with growing $\Delta P$ and a decrease in the area $\pi r^2$ (for which the model of a flat indenter holds) with dropping $P$.

In the case of uniform pressure distribution, the dependence $\Delta P(w)$ for $d$ = const is linear and differs from (1) only in its constant coefficient; namely,

$$\Delta P = E_r d \Delta w_e, \quad (4)$$

where $w_e = \frac{4}{\pi} w_1$. Thus, plastic-dent unloading turns out to be described by a combination of two elastic models, namely, by that of an indenter with a flat end of area $A$ and of a model of uniform pressure distributed over the same area. In an actual unloading process governed by (1) and (4), it is necessary to take into account that the parameter $x$ defining the domains of validity of these models varies simultaneously with $\Delta w_e$ and $\Delta w_1$.

On the internal boundary of the belt $\Delta r_z$, the opposite pressure $p_x$ is equal to $q$. Under this condition and with regard to (3), formula (2) (after multiplying it by $\pi a^2$) takes the form

$$q\pi a^2 = \frac{\Delta P}{2\left(1 - \frac{r^2}{a^2}\right)^{1/2}} = \frac{1}{2}\Delta P A_e^{-1/2},$$

where $A_e$ is the belt area normalized to the area of $\pi a^2$. Taking into account that $q\pi a^2 = P_r$, with $P_r$ being the load applied to the plastic-dent area [4], and introducing the diameter $y = 2r$, we write out these equalities in the following form:

$$\frac{1}{2}\frac{\Delta P}{P_r} = \left[\left(1 - \frac{y^2}{d^2}\right)\right]^{1/2} = A_e^{1/2}. \quad (5)$$

We denote two summands of the resulting strain for the areas $A_e$ and $\frac{y^2}{d^2}$, respectively, by $\delta w_e = f(\Delta w_e)$ and $\delta w_1 = f(\Delta w_1)$:

$$\Delta w = \delta w_e + \delta w_1. \quad (6)$$

The contributions of the quantities $\Delta w_e$ and $\Delta w_1$ to the resulting unloading process must satisfy boundary conditions. At the initial moment of unloading, the contribution of $\Delta w_e$ vanishes, because, in a purely elastic process, relationship (1) remains valid up to complete unloading. Furthermore, if the pressure becomes uniform over the entire area of a plastic dent with size $2\Delta r_z = 2a = d$ (as a result of opposite plastic strains), the strain takes the form $w_e = \frac{4}{\pi} w_1$. In this case, the contribution of $\Delta w_1$ vanishes. Thus, for $d = 2\Delta r_b$ with expressions (4), (1) taken into account, we arrive at

$$\delta w_e = \frac{4}{\pi}\Delta w_1\left(1 - \frac{y}{d}\right), \quad \delta w_1 = \Delta w_1 \frac{y}{d}.$$

Under unloading, the elastic relaxation completely transforms into the work of the plastic tensile deformation of area $A_e$. Therefore, omitting the factor 1/2 in equality (5), we obtain

$$\frac{y}{d} = \left[1 - \left(\frac{\Delta P}{P_r}\right)^2\right]^{1/2}.$$

The pressure onto area $A_e$ remains constant, while the area varies as $\left(\frac{y}{d}\right)^2$, but the pressure onto the residual elastic-contact area drops as $\frac{y}{d}$. Therefore, the total contribution of the two processes to the strain $\Delta w$ depends on the parameter $\frac{y}{d}$. The substitution of the above expressions into expression (1) yields the quantity $\Delta w$. After normalizing $\frac{\Delta w}{\Delta w_1}$, we arrive at the following correction:

$$\frac{\Delta w}{\Delta w_1} = \frac{4}{\pi} - \left(\frac{4}{\pi} - 1\right)\left[1 - \left(\frac{\Delta P}{P_r}\right)^2\right]^{1/2}. \quad (7)$$

Relationship (7) allows us to reliably determine the modulus $E_r$. To do this, we draw a straight line through the end points of the segment $\Delta P = P_r - P$ of the unloading curve and substitute the values obtained for the derivative $\frac{\Delta P}{\Delta w}$ into the conventional dependences presently used [1–7]. As a result, we obtain the value of $E_w$. The actual value $E_r$ of the modulus is determined by the relationship

$$\frac{E_r}{E_w} = \frac{\Delta w}{\Delta w_1}. \quad (8)$$

The correction found is valid only for the first unloading cycle, because the surfaces of the dent and indenter are becoming self-congruent while the number

of repeated cycles is increased. As a result, the hysteresis loop is contracted and the model of the flat indenter should be modified.

The corrections $\Pi = \frac{\Delta w}{\Delta w_1} - 1$ evaluated by formula (7) are presented in Fig. 2. They are compared with those found experimentally for a series of materials by measuring the variation of the slope $\frac{\Delta P}{\Delta w}$ for the straight line connecting the end points $P_r$ and $P$ of the segment $\Delta P$. Deviations of the experimental points from a linear dependence are virtually absent on segments with lengths up to $0.2\frac{\Delta P}{P_r}$. In the case of further unloading, the deviations from the calculated curve increase. Under complete unloading, these deviations are natural and indicate the character of the pressure distribution over the dent surface. For the Vickers and Berkovich pyramids, the deviations are within the limits of the values of $m$ from 1.3 to 1.5 [1, 3, 4] and from 1.2 to 1.6 [5], respectively.

Relationship (7) differs from the formula proposed in [4] since the former allows for the fact that the pressure distributions over areas $A_e$ and $\left(\frac{y}{d}\right)^2$ are different. Formula (7) makes it possible to take characteristic features of the unloading process into account. They are associated with both the manifestation of the Bauschinger effect and the difference in the normalized sizes of the plastic zone under the dent, which depend on the strain-hardening coefficient of the material. The influence of these effects results in the experimental data being poorly consistent with the calculated curve. The deviation measured allows the properties of materials to be estimated quantitatively according to the shape of the hysteresis loop recorded under repeated loading. The hysteresis loop increases with decreasing normalized size of the plastic zone under the dent, hence, with the resistance of the zone to opposite plastic strains. In this case, the loop width $\delta$ increases with dent unloading. After a certain number of repeated loads, plastic fatigue of the material arises. Thus, the hysteresis loop width is an important parameter in determining the kinetics of fatigue and wear and the above model for unloading a plastic dent elucidates the character of this parameter.

It becomes necessary to express the dimensional quantity $\delta$ in terms of the dimensionless strain $\varepsilon$. In a loaded dent, the strain is determined by elastic and plastic components differing in their physical nature. Elastic and plastic strains relate to variation in the body's volume and shape, respectively. If the total

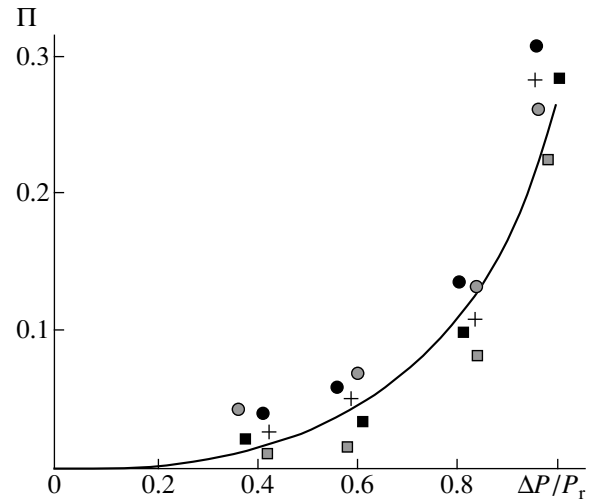


**Fig. 2.** Correction $\Pi$ to the Young's modulus as a function of the linear-segment length $\frac{\Delta P}{P_r}$. Experimental data are presented for (●) Ti, (+) Mo, (■) Cu, (●) L62 brass, and (■) D16T duralumin alloy.

strain in a dent of depth $h$ is equal to $\varepsilon$, then the strain $\delta$ should be expressed in the linear approximation as a fraction $\frac{\delta}{h}$ of $\varepsilon$.

In the presence of friction, the similar parameter $\frac{\delta}{w_1}$ becomes the stable characteristic of hysteresis, since the strain $h$ of the microridges on the surface is irregular (see Fig. 1). This stability is caused by the very strained state of the material in the surface layer. In this case, the $\sigma$–$\varepsilon$ diagram is close to a smooth plateau and crushing of the microridges takes place under the conditions when their hardness and elastic strain $\varepsilon_w$ remain constant. If the elastic strain is $\varepsilon_w$, then the strain $\varepsilon_{\delta w}$ proportional to $\delta$ should be expressed as a fraction $\frac{\delta}{w_1}$ of $\varepsilon_w$, with the relation between $w_1$ and $\varepsilon_w$ being linear.

The elastic strain is given by equations [1–4]

$$\varepsilon_w = \frac{2}{\sqrt{\pi}}\frac{w_1}{\sqrt{A}} = \frac{HM}{E_r}, \tag{9}$$

$$\frac{w_1}{\sqrt{A}} = \frac{\sqrt{\pi}}{2}\frac{HM}{E_r}. \tag{10}$$

Both the increase in the opening angle of a dent and the fraction of its plastic strain under unloading depend on the modulus of $w_1$ and on the relationship between $w_1$ and the elastic strain $w_s$ along the dent perimeter. The ratio $\frac{w_s}{w_1}$ weakly depends on the parameter $m = \frac{w}{w_1}$

(see Fig. 1) determining the mean pressure HM distribution over the area $A$.

For geometrically similar dents, $\varepsilon$ is independent of $h$. Taking into account that $\varepsilon_\delta < \varepsilon$, we have, in the linear approximation, that $\frac{\varepsilon_\delta}{\varepsilon} = \frac{\delta}{h}$ or

$$\varepsilon_\delta = \varepsilon\frac{\delta}{h}. \tag{11}$$

We then rewrite (11) in terms of the transverse size $\sqrt{A}$ (instead of $h$) of the unloaded dent and introduce the geometrical coefficient $c_A = \frac{\sqrt{A}}{h_\mathrm{d}}$ of the indenter shape, where $h_\mathrm{d}$ is the instrumental dent depth [1–4]. Taking into account that for the Vickers pyramid, $c_A = 4.95$, $\varepsilon = 0.08$, and $c_A\varepsilon = 0.40$, we arrive at

$$\varepsilon_\delta = 0.40\frac{\delta}{\sqrt{A}}. \tag{12}$$

If the strain $\varepsilon$ in a dent of area $A$ is proportional to its normalized volume $\left(\text{i.e., } \varepsilon = \frac{k}{c_A}\right)$, then the proportionality coefficient $k$ for the material given is, in fact, constant: $\varepsilon = \frac{kh}{\sqrt{A}} = \frac{k}{c_A} = 0.08$ and $k = \varepsilon c_A = 0.08 \times 4.95 \cong 0.40$. This value of $k$ holds for arbitrary opening angles of the plastic dent.

By virtue of the linear relation between $w_1$ and $\varepsilon_w$, the hysteresis strain is exactly expressed in terms of the elastic strain:

$$\varepsilon_{\delta w} = \varepsilon_w\frac{\delta}{w_1}. \tag{13}$$

Dividing the numerator and denominator in (13) by $\sqrt{A}$, we obtain, with regard to (9),

$$\varepsilon_{\delta w} = \frac{2}{\sqrt{\pi}}\frac{\delta}{\sqrt{A}}. \tag{14}$$

Equation (14) differs from (12) only in the factor which is determined by the different nature of the elastic and plastic strains. Comparison of these expressions yields the equality

$$\frac{\varepsilon_{\delta w}}{\varepsilon_\delta} = 2.8 \simeq \frac{HM}{\sigma} = 3, \tag{15}$$

where $\sigma$ is the corresponding tensile stress. Due to the nonlinear behavior of the strain-hardening coefficient $\frac{d\sigma}{d\varepsilon}$, which decreases with increasing strain, the inequality holds: $\frac{\varepsilon_{\delta w}}{\varepsilon_\delta} < \frac{\mathrm{HM}}{\sigma}$. Therefore, the factor $k$ in (12) must decrease with increasing $c_A$.

When analyzing processes of fatigue and wear, true plastic strain $\varepsilon_\delta$ should be used. To calculate its value, we should pass from the quantity $h$ to the actual size $\sqrt{A}$ of the contact area. The relation between $h$ and $\sqrt{A}$ has been considered in [1, 3, 4]. For large values of $c_A$,

$$\frac{\sqrt{A}}{c_A} = h_\mathrm{d} = h - w_s \simeq h - 0.78w_1. \tag{16}$$

In the linear approximation, $\frac{w_s}{w_1} = 0.81 - 0.26(m - 1.27)$ [4]. In a region of quasi-elastic contact, it is advisable to express the relation between $m$ and $\frac{w_s}{w_1}$ as a power series. For rapid estimates, this is less convenient but more accurate than the linear approximation proposed in [4]. The dependence $\frac{w_s}{w_1}(m)$ is approximated by the following function:

$$1 - \frac{w_s}{w_1} = -0.1201(m-1)^4 + 0.7607(m-1)^3 - 1.3842(m-1)^2 + 1.017(m-1).$$

In the interval of $m$ from $\frac{4}{\pi}$ to 1.5, it is reasonable to use the simplified expression $\frac{w_s}{w_1} = 1 - 0.334(m-1)^{0.433}$.

Formula (12) remains valid in the entire range of variation from fully plastic contacts to quasi-elastic contacts; the latter can be realized with indenters having proper shapes. Therefore, using a set of indenters which realize various contact conditions, we can find strain $\varepsilon_\delta$ as a function of specific pressure $p$ in the tribound or of stress $\sigma$ under fatigue conditions. It is evident that the dependence $\varepsilon_\delta(p)$ is correlated with wear resistance and fatigue.

The experimental data for the accumulation rate of the recoverable plastic strain in various materials under local loading by the Vickers pyramid ($\varepsilon \simeq 0.08$) are given in the table. For metal alloys, this quantity, as a rule, decreases with increasing number $N$ of unloading cycles and becomes stable after 10 to 12 cycles. For large $N$, either cyclic hardening or cyclic softening of the material takes place.

It is seen from the table that, in contrast to the Meyer index $n$, the hysteresis strain ranges within a limit of one order of magnitude and depends on two material characteristics: the strain-hardening coefficient and the normalized hardness $\frac{\mathrm{HM}}{E_\mathrm{r}}$. In this connection, a more

The hysteresis strain $\varepsilon_\delta$ compared to other stress–strain properties of materials

| No. | Material | $\frac{HV_h}{HV}$ | $E$, GPa | $\frac{HM}{E}$ | $E_r$, GPa | $\frac{\delta}{W_1}$, % | $\varepsilon_\delta$, % |
|---|---|---|---|---|---|---|---|
| 1 | Mo | 1.02 | 330 | 0.006 | 268 | 10.0 | 0.02 |
| 2 | 30KhGSA steel | 1.08 | 210 | 0.013 | 187 | 14.0 | 0.065 |
| 3 | 12Kh18N9T steel | 1.04 | 204 | 0.0085 | 182 | 7.0 | 0.02 |
| 4 | Steel 45 | 1.12 | 195 | 0.014 | 165 | 14.0 | 0.07 |
| 5 | L62 brass | 1.08 | 98 | 0.0146 | 99 | 9.0 | 0.045 |
| 6 | D16T duralumin alloy | 1.06 | 80 | 0.022 | 79.5 | 4.5 | 0.035 |
| 7 | Titanium alloy | 1.08 | 130 | 0.0206 | 123 | 7.0 | 0.05 |
| 8 | Ni–Al–Cr | 0.94 | 210 | 0.037 | 187 | 6.0 | 0.08 |
| 9 | Glass | 0.85 | 74 | 0.091 | 73.7 | 10 | 0.32 |
| 10 | KV glass | 0.68 | 71 | 0.106 | 70.7 | 10 | 0.38 |
| 11 | $FeAl_3$ | 0.77 | 110 | 0.071 | 106 | 1.0 | 0.025 |

Note: When evaluating $E_r$, we assume for diamond that $E$ = 1140 GPa and that the Poisson's ratio $\nu$ is 0.07.

accurate and rapid method for determining hardness properties becomes possible, which is based on the empirical dependences $n \sim \frac{\delta}{w_1} \sim \frac{\Delta h}{h}$, where $\Delta h$ is the height of a material ridge extruded from a dent. Therefore, the parameters $H_h$ and $\frac{\delta}{w_1}$ of the $P$–$h$ diagram quantitatively determine the tensile diagram within the range before uniform strain.

Thus, the plastic-dent unloading described by a combination of the two models makes it possible to determine the degree of nonlinearity for the unloading curve. To do this, we approximate the curved segment by a straight line and then determine its slope with the correction depending on the linear-segment length. Such a description of the unloading of the plastic dent in a material allows us to estimate the strain-hardening coefficient according to the magnitude and shape of the hysteresis loop. Both the Bauschinger effect and the effect of cyclic hardening or cyclic softening are also related to the strain hardening. Moreover, the above method makes it possible to develop new, more accurate techniques for determining mechanical properties through hardness measurements.

## REFERENCES


1. S. I. Bulychev and V. P. Alekhin, *Testing of Materials by Continuous Depression of an Indenter* (Mashinostroenie, Moscow, 1990).
2. S. I. Bulychev, V. P. Alekhin, M. Kh. Shorshorov, *et al.*, Zavod. Lab. **41**, 1137 (1975).
3. V. P. Alekhin and S. I. Bulychev, Fiz. Khim. Obrab. Mater., No. 3, 134 (1978).
4. S. I. Bulychev, Zh. Tekh. Fiz. **69**, 42 (1999) [Tech. Phys. **44**, 775 (1999)].
5. W. C. Oliver and G. M. Pharr, J. Mater. Res. **7**, 1564 (1992).
6. M. J. F. Doerner and W. D. Nix, J. Mater. Res. **1**, 601 (1986).
7. E. Soderlund and D. J. Rowcliffe, J. Hard Mater. **5** (4), 149 (1994).


*Translated by V. Chechin*

*Doklady Physics, Vol. 45, No. 12, 2000, pp. 672–675. Translated from Doklady Akademii Nauk, Vol. 375, No. 5, 2000, pp. 619–621.*
*Original Russian Text Copyright © 2000 by Konkina, Markov, Mikisha, Rykhlova.*

ASTRONOMY, ASTROPHYSICS, AND COSMOLOGY

# On the Problem of Constructing Intermediate Trajectories in the Theory of Elastic-Earth Rotation around a Center of Mass

**L. I. Konkina, Yu. G. Markov, A. M. Mikisha, and L. V. Rykhlova**

Presented by Academician A.A. Boyarchuk February 21, 2000

Received November 21, 1999

The development of the exact theory of Earth rotation is a rather complicated mathematical problem and requires the elimination of a number of simplifications in the accepted theory [2]. In spite of the exceptionally high level of modern observations, researchers have failed to attain a complete understanding of such dynamic effects as the free nutation of the Earth-rotation axis and the variation of latitudes, both of which are extremely necessary in constructing a highly accurate theory of rotational motion for the deformable Earth.

We attempted to study certain fine regularities in the theory of Earth rotation around its center of mass from more general positions, namely, translational–rotational movement. As a starting theoretical model, we used the intermediate two-body problem of the Earth–Moon system, which made it possible to take into account the barycentric distance. In this intermediate motion, the Earth uniformly rotates and deforms under the action of centrifugal forces of inertia and the lunar gravitation field. The deformations are considered to proceed quasi-statically (the inertia terms can be ignored). In other words, the motion of the three-axis elastic Earth as a whole around its center of mass can be represented as the motion of a planet with an equilibrium configuration and "frozen" deformations. Furthermore, on the basis of the intermediate model problem, it is of interest to consider the dynamics of evolutionary processes, but already using perturbed motion with allowance for dissipative factors and lunar–solar perturbations.

In our opinion, when developing the theory of the Earth's rotation around its center of mass, an important argument is the fact that the Earth–Moon dynamic system is assigned to the class of systems with a slow evolution in which it is possible to trace multistage dynamic processes with various characteristic times. Thus, it is possible to compare the characteristic times of the Earth's own rotation around its axis, of the precession of the kinetic-moment vector for the deformable Earth, and of the evolution of the rotation-axis inclination to the plane of the ecliptic. In such a system, the natural separation of motions into fast and slow motions takes place and these motions are described by their corresponding parameters. Under certain conditions, it is possible to isolate a set of slow parameters (variables) whose rate of variation is asymptotically slow (with respect to a certain small parameter), and the evolutionary equations describing this variation are separated from the remaining equations of the set [5]. Equations averaged over the fast variables for the translational–rotational motions of the Earth–Moon system in the solar gravitational field are studied independently. In the majority of cases, these equations turn out to be a good approximation to the original equations for a long (in the asymptotic sense) time interval. The equations for the remaining variables form a fast component of the Earth–Moon system and involve the evolutionary-system variables as slowly varying parameters. It should be noted that, from the standpoint of evolutionary processes, the qualitative picture of the fast motions of the system is a background against which the slow evolution of the orbital–rotational motion occurs.

**1.** The choice of intermediate trajectories for the Earth's motion is based on the spatial variant of the two-body (planet–satellite) problem and, namely, the deformable-Earth–Moon system (the Moon is taken as a mass point) and is analyzed from the positions of a double planet. This automatically presumes the presence of a barycentre and allows for its position in subsequent calculations. The model problem under consideration is formulated as follows: let a deformable planet (the Earth) and its satellite (the Moon) participate in the mutual translational–rotational motion around their common center of mass (barycentre). The satellite orbit is inclined at an arbitrary angle to the planet's equator. The Earth is represented by a two-layer model with a solid core and a viscoelastic mantle [1, 7], which are individually continuous. We introduce the inertial sys-

*Institute of Astronomy, Russian Academy of Sciences, ul. Pyatnitskaya 48, Moscow, 109017 Russia*

1028-3358/00/4512-0672$20.00 © 2000 MAIK "Nauka/Interperiodica"

tem of coordinates $C\xi_1\xi_2\xi_3$ with the origin in the barycenter of the planetary system. Let **G** be the Earth's own kinetic moment and **Λ** be the orbital angular momentum for the lunar center of mass $C_1$ and the terrestrial center of mass $C_2$. The angular momentum $\mathbf{K} = \mathbf{G} + \mathbf{\Lambda}$ of the entire planetary system is immobile in the inertial space and coincides with the axis $C\xi_3$ (see the figure).

The radii vectors for the points $C_1$ and $C_2$ in the $C\xi_1\xi_2\xi_3$ coordinate system are given in the form

$$\begin{gathered}\mathbf{R}_i = R_i\mathbf{R}_i^0, \quad R_i = \tilde{c}_i R_{21}, \quad i = 1, 2,\\ \mathbf{R}_i^0 = \Gamma_3(h)\Gamma_1(i)(\cos\vartheta, \sin\vartheta, 0), \quad \mathbf{R}_2^0 = -\mathbf{R}_1^0, \\ \tilde{c}_1 = m_2 m^{-1}, \quad \tilde{c}_2 = m_1 m^{-1}, \quad m = m_1 + m_2.\end{gathered} \tag{1}$$

Here, $h$, $i$, and $\vartheta$ are the ascending-node longitude, the inclination, and the orbit true anomaly, respectively; $\mathbf{R}_{21} = R_{21}\mathbf{R}_{21}^0$ is the radius vector drawn from the point $C_2$ to the point $C_1$, so that $\mathbf{R}_{21} = \mathbf{R}_1^0$. The $C_2x_1x_2x_3$ Cartesian coordinate system is rigidly related to the solid core of the planet. The axes of this system are directed along the principal axes of inertia $A$, $B$, and $C$ of the planet. For this coordinate system, we may write out

$$\begin{gathered}O^{-1}(t)\vec{\mathbf{R}}_{21}^0 = (\gamma_1, \gamma_2, \gamma_3),\\ O^{-1}(t) = \Gamma_3^{-1}(\varphi_1)\Gamma_1^{-1}(\delta_2)\Gamma_3^{-1}(\varphi_2)\Gamma_1^{-1}(\delta_1)\Gamma_3^{-1}(\varphi_3),\end{gathered} \tag{2}$$

where $O(t)$ is the matrix specifying the passage from the body axes to the inertial axes and is expressed in Andoyer canonical variables: $L$, $I_2 = |\vec{\mathbf{G}}|$, $I_3$, $\varphi_1$, $\varphi_2$, and $\varphi_3$; and $\cos\delta_1 = I_3/I_2$, $\cos\delta_2 = L/I_2$ [5, 6].

We describe the mutual orbital motion of mass centers in the $\Lambda$, $H$, $\vartheta$, $h$ Delone canonical variables, where $H$ is the projection of $\Lambda$ onto the $C\xi_3$-axis, $\Lambda = |\vec{\mathbf{\Lambda}}|$, and $\cos i = H/\Lambda$.

After a number of simple transformations and averaging over the fast variables $\varphi_2$ and $\vartheta$, the Routh functional of the intermediate problem is reduced to the form (with an accuracy to an insignificant constant)

$$\Re = \frac{I_2^2 - L^2}{2}\left[\frac{\sin^2\varphi_1}{\tilde{A}} + \frac{\cos^2\varphi_1}{\tilde{B}}\right] + \frac{L^2}{2\tilde{C}} + \text{const}, \tag{3}$$

where $\tilde{A}$, $\tilde{B}$, and $\tilde{C}$ are the elastic-Earth principal moments of inertia modified under the action of the centrifugal forces induced by the Earth's rotation. With

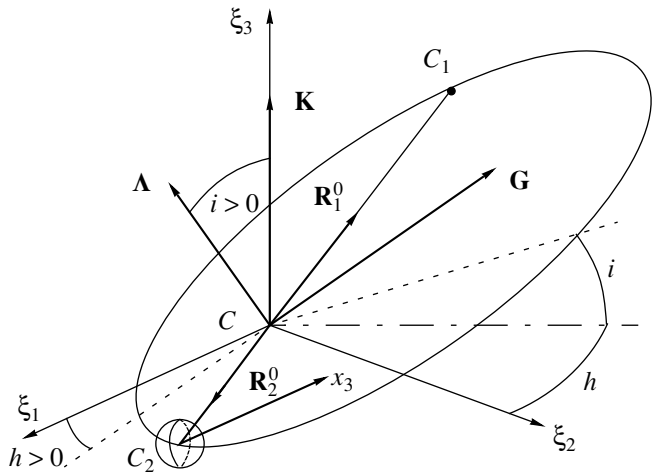


Coordinate system and orientation of vectors.

allowance for the barycentric distance, they take the form

$$\begin{gathered}\tilde{A} = \frac{J_{11}[\vec{\mathbf{u}}]I_2^2}{I_2^2 + 3\mu_1 R_{21}^{-3} d J_{11}^2[\vec{\mathbf{u}}]},\\ \tilde{B} = \frac{J_{22}[\vec{\mathbf{u}}]I_2^2}{I_2^2 + 3\mu_1 R_{21}^{-3} d J_{22}^2[\vec{\mathbf{u}}]},\\ \tilde{C} = \frac{J_{33}[\vec{\mathbf{u}}]I_2^2}{I_2^2 + 3\mu_1 R_{21}^{-3} d J_{33}^2[\vec{\mathbf{u}}]},\\ d = \cos^2\tilde{h} + \cos^2 i\sin^2\tilde{h}\\ + \cos^2\delta_1(\sin^2\tilde{h} + \cos^2 i\cos^2\tilde{h}) + \sin^2 i\sin^2\delta_1,\\ \tilde{h} = \varphi_3 - h, \quad \mu_1 = f m_1.\end{gathered} \tag{4}$$

Here, $f$ is the gravitation constant; $J_{ii}[\mathbf{u}] = \mathrm{diag}\{J_{11}[\mathbf{u}], J_{22}[\mathbf{u}], J_{33}[\mathbf{u}]\}$ is the inertia-tensor components dependent on the vector **u** of the elastic translation for the deformed planet in the planetary coordinate system; and $J[0] = \mathrm{diag}\{A, B, C\}$ for $\mathbf{u} = 0$. Structural form (3) coincides exactly with the traditional expression for the Routh function of a perfectly rigid body in the Andoyer variables and is a basis for introducing the action–angle variables $I_i$ and $w_i$ ($i = 1, 2, 3$). It should be noted that the action–angle variables compose the Hamiltonian part of the variables, whereas the generalized coordinates (modal variables) describing the deformations of the shell compose the Lagrangian part of the variables.

Thus, we introduce the following principal dynamic parameters:

$$\kappa^2 = \frac{\tilde{C}(\tilde{A} - \tilde{B})}{\tilde{A}(\tilde{B} - \tilde{C})}, \quad \lambda^2 = \kappa^2\frac{2E\tilde{C} - I_2^2}{I_2^2 - 2E\tilde{A}}, \tag{5}$$

where $E$ is the energy constant.

The relation between the action–angle variables and the Andoyer variables is given by the following formulas [3, 4] (for brevity, we restrict ourselves by the case $0 \le \lambda < 1$):

$$I_1 = \frac{2I_2}{\pi\kappa}\sqrt{\frac{1+\kappa^2}{\lambda^2+\kappa^2}}\left[(\lambda^2+\kappa^2)\Pi\left(\frac{\pi}{2}, \kappa^2, \lambda\right) - \lambda^2 K(\lambda)\right],$$

$$I_2 = I_2, \quad I_3 = I_3,$$

$$w_1 = \pm\frac{\pi}{2}\left[\frac{F(\xi, \lambda)}{K(\lambda)}\right], \quad \xi = \pm am(u, \lambda), \quad \mathbf{u} = \frac{2K(\lambda)}{\pi}w_1, \tag{6}$$

$$w_2 = \varphi_2 \pm \left\{\frac{1}{\kappa}\sqrt{(1+\kappa^2)(\kappa^2+\lambda^2)}\right.$$

$$\left.\times\left[\Pi(\xi, \kappa^2, \lambda) - \Pi\left(\frac{\pi}{2}, \kappa^2, \lambda\right)\frac{F(\xi, \lambda)}{K(\lambda)}\right]\right\},$$

$$\cot\varphi_1 = -\sqrt{1+\kappa^2}\tan\xi, \quad w_3 = \varphi_3.$$

Here, $K(\lambda)$, $\Pi(\pi/2, \kappa^2, \lambda)$ are the complete elliptic integrals of the first and third kinds; and $F(\xi, \lambda)$, $\Pi(\xi, \kappa^2, \lambda)$ are the elliptic integrals of the first and third kinds.

In this case, Routh functional (3) can be written out as

$$\Re = \frac{I_2^2}{2\tilde{A}}\left(1 - \frac{\tilde{C}-\tilde{A}}{\tilde{C}}\frac{\kappa^2}{(\lambda^2+\kappa^2)}\right). \tag{7}$$

The general solution to the intermediate problem with functional (7) has the form

$$I_i = I_i(0), \quad i = 1, 2, 3, \quad w_1 = n_{w_1}t + w_{10},$$

$$w_2 = n_{w_2}t + w_{20},$$

$$n_{w_1} = \frac{I_2(\tilde{A}-\tilde{C})}{2\tilde{A}\tilde{C}}\frac{\pi\kappa}{\sqrt{(1+\kappa^2)(\kappa^2+\lambda^2)}K(\lambda)}, \tag{8}$$

$$n_{w_2} = \frac{I_2}{\tilde{C}}\left(1 - \frac{\tilde{A}-\tilde{C}}{\tilde{A}}\frac{\Pi(\pi/2, \kappa^2, \lambda)}{K(\lambda)}\right),$$

where $w_{10}$ and $w_{20}$ are the initial values of the angular variables.

Solving the first equation of set (6) with respect to $\lambda$ with an accuracy to $\lambda^2$ inclusively, we obtain

$$\lambda^2 = \frac{2\kappa^2(I_2 - I_1)}{I_2\sqrt{1+\kappa^2}}, \quad 0 \le \lambda < 1. \tag{9}$$

Using (9), we can represent the frequencies of intermediate motion (8) in the form ($0 \le \lambda < 1$)

$$n_{w_1} = \frac{I_2}{\kappa_1}\frac{\tilde{A}-\tilde{C}}{\tilde{A}\tilde{C}}\left(1 - \frac{2+\kappa^2}{2\kappa_1}\frac{I_2 - I_1}{I_2}\right), \quad \kappa_1 = \sqrt{1+\kappa^2},$$

$$n_{w_2} = \frac{I_2}{\tilde{C}}\left[1 + \frac{\tilde{C}-\tilde{A}}{\kappa_1\tilde{A}}\left(1 + \frac{I_2 - I_1}{2\kappa_1 I_2}(2\kappa_1 - 2 - \kappa^2)\right)\right]. \tag{10}$$

**2.** As an example, we consider the Chandler wobble of the Earth's poles. The wobble is determined as a motion of the rotation axis with respect to the figure axis [8]:

$$x_p = \frac{\omega_x}{\omega} = \frac{I_2\lambda}{\tilde{A}\omega\sqrt{\kappa^2+\lambda^2}}\mathrm{cn}\mathbf{u},$$

$$y_p = -\frac{\omega_y}{\omega} = -\frac{\lambda I_2\sqrt{1+\kappa^2}}{\tilde{B}\omega\sqrt{\kappa^2+\lambda^2}}\mathrm{sn}\mathbf{u}, \tag{11}$$

$$\omega = \frac{I_2}{\tilde{A}\sqrt{\kappa^2+\lambda^2}}\sqrt{\lambda^2 + \frac{\tilde{A}^2}{\tilde{C}^2}\kappa^2 - \lambda^2\left(1 + \frac{\tilde{A}^2}{\tilde{C}^2}\kappa^2\right)\mathrm{sn}^2\mathbf{u}}.$$

Here, sn**u** and cn**u** are the Jacobi elliptic functions, which are represented by the expansions in the Fourier trigonometric series [3, 4]. In (11), according to the accepted convention [8], $y_p$ is directed along the 90° meridian of the western longitude.

The period of the Chandler wobble is determined by the following expression:

$$T = \frac{2\pi}{n_{W_1}}. \tag{12}$$

Formula (12) relates the period of the Chandler wobble with the principal dynamic parameters introduced by the authors: the energy constant, the kinetic-moment modulus, and the Earth's principal moments of inertia.

The analytical expressions obtained in this study for the moments of inertia of the Earth with allowance for its elasticity and the translational type of its motion is a basis for both constructing a highly accurate theory of the Chandler wobble and for a comparison of this theory with long-term astronomical observations and estimates for the period of this vibration. It should be especially emphasized that, on the basis of the derived averaged differential equations, we can trace the evolution of both the pole vibrational motion and the moments of inertia for the Earth.

## ACKNOWLEDGMENTS

This work was supported by the "Astronomy" State Scientific and Applied Program, project no. 1.8.1.2.

## REFERENCES

1. Yu. G. Markov, L. V. Rykhlova, and I. V. Skorobogatykh, Dokl. Akad. Nauk **370**, 613 (2000) [Dokl. Phys. **45**, 70 (2000)].
2. N. Moritz and A. Mueller, *Earth Rotation: Theory and Observation* (Ungar, New York, 1987; Naukova Dumka, Kiev, 1992).
3. Yu. A. Sadov, Prikl. Mat. Mekh. **34**, 962 (1970).
4. Yu. V. Barkin, Astron. Astrophys. Trans. **17**, 179 (1998).
5. V. G. Vil'ke, *Analytical and Qualitative Methods in Mechanics of Systems with an Infinite Number of Degrees of Freedom* (Mosk. Gos. Univ., Moscow, 1986).
6. Yu. G. Markov, Astron. Zh. **73**, 748 (1996) [Astron. Rep. **40**, 681 (1996)].
7. V. V. Bondarenko, Yu. G. Markov, and I. V. Skorobogatykh, Astron. Vestn. **32**, 340 (1998).
8. H. Kinoshita, Celest. Mech. **15**, 277 (1977).

*Translated by V. Bukhanov*

*Doklady Physics, Vol. 45, No. 12, 2000, pp. 676–679. Translated from Doklady Akademii Nauk, Vol. 375, No. 4, 2000, pp. 472–475.*
*Original Russian Text Copyright © 2000 by Mikhaĭlova.*

**MECHANICS**

# A State with Bulk Stresses Arising in an Ideally Plastic Layer under Compression by Rough Plates

**M. V. Mikhaĭlova**

Presented by Academician A.Yu. Ishlinskiĭ March 6, 2000

Received March 14, 2000

L. Prandtl [1] presented an asymptotic solution to the problem of a flat slab compressed by rough plates. In [2–4], this solution was extended to cases with bulk stresses. Below, we consider the stressed state of a bulk layer made of an ideally plastic material compressed by curved and inclined rough plates under conditions of perfect plasticity [5].

**1.** Under conditions of perfect plasticity, the stressed state of a bulk layer with thickness $2h$ compressed along the $z$-axis by rough parallel plates (the figure) is determined by the relationships [3]

$$\begin{gathered}\tau_{xz} = az, \quad \tau_{yz} = bz, \quad a, b\text{—const},\\ \sigma_x = -ax - by - \frac{abz^2}{\tau_{xy}} + c + \frac{a}{b}\tau_{xy},\\ \sigma_y = -ax - by - \frac{abz^2}{\tau_{xy}} + c + \frac{b}{a}\tau_{xy},\\ \sigma_z = -ax - by + c, \quad c\text{—const},\\ \tau_{xy} = \frac{ab}{a^2+b^2}\left(k \pm \sqrt{k^2 - (a^2+b^2)z^2}\right),\end{gathered} \tag{1}$$

where $\sigma_{ij}$ are components of the stress tensor and $k$ is the shear yield point.

We consider the problem concerning a plastic layer compressed by two concentric spherical surfaces.

In the spherical coordinate system, the equilibrium equations have the form

$$\begin{gathered}\frac{\partial\sigma_\rho}{\partial\rho} + \frac{1}{\rho}\frac{\partial\tau_{\rho\theta}}{\partial\theta} + \frac{1}{\rho\sin\theta}\frac{\partial\tau_{\rho\varphi}}{\partial\varphi}\\ + \frac{1}{\rho}(2\sigma_\rho - \sigma_\theta - \sigma_\varphi + \tau_{\rho\theta}\cot\theta) = 0,\\ \frac{\partial\tau_{\rho\theta}}{\partial\rho} + \frac{1}{\rho}\frac{\partial\sigma_\theta}{\partial\theta} + \frac{1}{\rho\sin\theta}\frac{\partial\tau_{\theta\varphi}}{\partial\varphi}\\ + \frac{1}{\rho}(3\tau_{\rho\theta} + (\sigma_\theta - \sigma_\varphi)\cot\theta) = 0,\\ \frac{\partial\tau_{\rho\varphi}}{\partial\rho} + \frac{1}{\rho}\frac{\partial\tau_{\theta\varphi}}{\partial\theta} + \frac{1}{\rho\sin\theta}\frac{\partial\sigma_\varphi}{\partial\varphi}\\ + \frac{1}{\rho}(3\tau_{\rho\varphi} + 2\tau_{\theta\varphi}\cot\theta) = 0.\end{gathered} \tag{2}$$

Following [3], we can write the condition of perfect plasticity using the following relationships:

$$\begin{gathered}\sigma_\rho = \sigma - \frac{2k}{3} + \frac{\tau_{\rho\theta}\tau_{\rho\varphi}}{\tau_{\theta\varphi}}, \quad \sigma_\theta = \sigma - \frac{2k}{3} + \frac{\tau_{\rho\theta}\tau_{\theta\varphi}}{\tau_{\rho\varphi}},\\ \sigma_\varphi = \sigma - \frac{2k}{3} + \frac{\tau_{\rho\varphi}\tau_{\theta\varphi}}{\tau_{\rho\theta}},\\ \frac{\tau_{\rho\theta}\tau_{\rho\varphi}}{\tau_{\theta\varphi}} + \frac{\tau_{\rho\theta}\tau_{\theta\varphi}}{\tau_{\rho\varphi}} + \frac{\tau_{\rho\varphi}\tau_{\theta\varphi}}{\tau_{\rho\theta}} = 2k,\\ \sigma = \frac{1}{3}(\sigma_\rho + \sigma_\theta + \sigma_\varphi).\end{gathered} \tag{3}$$

Further on, we use dimensionless variables; i.e., we normalize the stress components by dividing them by the value of shear yield point $k$ and measure the length in units of $h$.

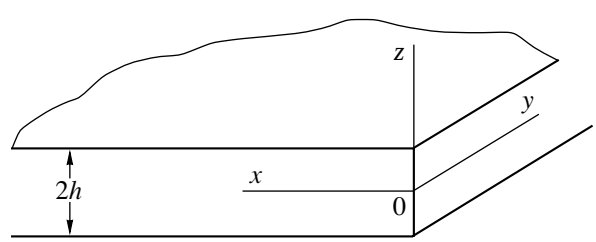


**Figure.**

*Chuvash State Pedagogical University,*
*ul. Karla Marksa 38, Cheboksary, 428000 Russia*

1028-3358/00/4512-0676$20.00 © 2000 MAIK "Nauka/Interperiodica"

We introduce the change of variables

$$\rho = R + z, \quad R\left(\theta - \frac{\pi}{2}\right) = y, \qquad (4)$$
$$R\varphi = x, \quad R\text{—const}$$

and represent (4) in the form

$$\frac{1}{\rho} = \frac{\delta}{1+\delta z}, \ \theta = \frac{\pi}{2} + \delta y, \ \varphi = \delta x, \ \delta = \frac{1}{R}, \qquad (5)$$

where $\delta$ is a small dimensionless parameter.

Then, we use relationships (5) to pass to variables $x$, $y$, and $z$ in equilibrium equations (2). This yields the system

$$\begin{aligned}
&\frac{\partial\sigma_z}{\partial z} + \frac{1}{1+\delta z}\frac{\partial\tau_{yz}}{\partial y} + \frac{1}{(1+\delta z)\cos(\delta y)}\frac{\partial\tau_{xz}}{\partial x} \\
&+ \frac{\delta}{1+\delta z}(2\sigma_z - \sigma_y - \sigma_x - \tau_{yz}\tan(\delta y)) = 0, \\
&\frac{\partial\tau_{yz}}{\partial z} + \frac{1}{1+\delta z}\frac{\partial\sigma_y}{\partial y} + \frac{1}{(1+\delta z)\cos(\delta y)}\frac{\partial\tau_{xy}}{\partial x} \\
&+ \frac{1}{1+\delta z}(3\tau_{yz} - (\sigma_y - \sigma_x)\tan(\delta y)) = 0, \\
&\frac{\partial\tau_{xz}}{\partial z} + \frac{1}{1+\delta z}\frac{\partial\tau_{xy}}{\partial y} + \frac{1}{(1+\delta z)\cos(\delta y)}\frac{\partial\sigma_x}{\partial x} \\
&+ \frac{1}{1+\delta z}(3\tau_{xz} - 2\tau_{xy}\tan(\delta y)) = 0.
\end{aligned} \qquad (6)$$

At $\delta = 0$, equations (6) are transformed into equations describing the equilibrium in the Cartesian coordinate system $x$, $y$, $z$.

The solution is sought in the form

$$\sigma_{ij} = \sigma_{ij}^0 + \delta\sigma'_{ij}. \qquad (7)$$

We use solution (1) as an initial zeroth approximation. Based on (6), (7), and (3), we find the first approximation:

$$\begin{aligned}
&\frac{\partial\sigma'_x}{\partial x} + \frac{\partial\tau'_{xy}}{\partial y} + \frac{\partial\tau'_{xz}}{\partial z} = \frac{\partial\sigma_x^0}{\partial x}z + \frac{\partial\tau_{xy}^0}{\partial y}z - 3\tau_{xz}^0, \\
&\frac{\partial\tau'_{xy}}{\partial x} + \frac{\partial\sigma'_y}{\partial y} + \frac{\partial\tau'_{yz}}{\partial z} = \frac{\partial\tau_{xy}^0}{\partial x}z + \frac{\partial\sigma_y^0}{\partial y}z - 3\tau_{yz}^0, \\
&\frac{\partial\tau'_{xz}}{\partial x} + \frac{\partial\tau'_{yz}}{\partial y} + \frac{\partial\sigma'_z}{\partial z} = \frac{\partial\tau_{xz}^0}{\partial x}z + \frac{\partial\tau_{yz}^0}{\partial y}z - 2\sigma_z^0 + \sigma_x^0 + \sigma_y^0;
\end{aligned} \qquad (8)$$

$$\begin{aligned}
&\sigma'_x = \sigma' + \frac{(\tau'_{xy}\tau_{xz}^0 + \tau_{xy}^0\tau'_{xz})\tau_{yz}^0 - \tau_{xy}^0\tau_{xz}^0\tau'_{yz}}{(\tau_{yz}^0)^2}, \\
&\sigma'_y = \sigma' + \frac{(\tau'_{xy}\tau_{yz}^0 + \tau_{xy}^0\tau'_{yz})\tau_{xz}^0 - \tau_{xy}^0\tau_{yz}^0\tau'_{xz}}{(\tau_{xz}^0)^2}, \\
&\sigma'_z = \sigma' + \frac{(\tau'_{xz}\tau_{yz}^0 + \tau_{xz}^0\tau'_{yz})\tau_{xy}^0 - \tau_{xz}^0\tau_{yz}^0\tau'_{xy}}{(\tau_{xy}^0)^2};
\end{aligned} \qquad (9)$$

$$\begin{aligned}
&\frac{(\tau'_{xy}\tau_{xz}^0 + \tau_{xy}^0\tau'_{xz})\tau_{yz}^0 - \tau_{xy}^0\tau_{xz}^0\tau'_{yz}}{(\tau_{yz}^0)^2} \\
&+ \frac{(\tau'_{xy}\tau_{yz}^0 + \tau_{xy}^0\tau'_{yz})\tau_{xz}^0 - \tau_{xy}^0\tau_{yz}^0\tau'_{xz}}{(\tau_{xz}^0)^2} \\
&+ \frac{(\tau'_{xz}\tau_{yz}^0 + \tau_{xz}^0\tau'_{yz})\tau_{xy}^0 - \tau_{xz}^0\tau_{yz}^0\tau'_{xy}}{(\tau_{xy}^0)^2} = 0.
\end{aligned} \qquad (10)$$

Here,

$$\tau_{xz}^0 = az, \quad \tau_{yz}^0 = bz,$$
$$\tau_{xy}^0 = \frac{ab}{a^2+b^2}\left(1 \pm \sqrt{1-(a^2+b^2)z^2}\right).$$

From (1) and (8), we find

$$\begin{aligned}
&\frac{\partial\sigma'_x}{\partial x} + \frac{\partial\tau'_{xy}}{\partial y} + \frac{\partial\tau'_{xz}}{\partial z} = -4az, \\
&\frac{\partial\tau'_{xy}}{\partial x} + \frac{\partial\sigma'_y}{\partial y} + \frac{\partial\tau'_{yz}}{\partial z} = -4bz, \\
&\frac{\partial\tau'_{xz}}{\partial x} + \frac{\partial\tau'_{yz}}{\partial y} + \frac{\partial\sigma'_z}{\partial z} = -4 + 3\left(\frac{a}{b} + \frac{b}{a}\right)\tau_{xy}^0.
\end{aligned} \qquad (11)$$

Following the approach of Prandtl [1], we set

$$\tau'_{xz} = \tau'_{xz}(z), \ \tau'_{yz} = \tau'_{yz}(z). \qquad (12)$$

Then, according to (12), (10), and (1), we have $\tau'_{xy} = \tau'_{xy}(z)$. A solution to system (11) has the form

$$\begin{aligned}
&\tau'_{xz}(z) = a_1 z - 2az^2 + c_1, \quad a_1, c_1\text{—const}, \\
&\tau'_{yz}(z) = b_1 z - 2bz^2 + c_2, \quad b_1, c_2\text{—const};
\end{aligned} \qquad (13)$$

$$\begin{aligned}
&\sigma'_x = -a_1 x - b_1 y + c - f_3(z) + f_1(z) + F(z), \\
&\sigma'_y = -a_1 x - b_1 y + c - f_3(z) + f_2(z) + F(z), \\
&\sigma'_z = -a_1 x - b_1 y + c + F(z), \\
&F(z) = -z \pm 3\sqrt{a^2+b^2} \\
&\times\left[\frac{z}{2}\sqrt{\frac{1}{a^2+b^2} - z^2} \pm \frac{1}{2(a^2+b^2)}\arcsin\left(z\sqrt{a^2+b^2}\right)\right], \\
&f_1(z) = \frac{(\tau'_{xy}\tau_{xz}^0 + \tau_{xy}^0\tau'_{xz})\tau_{yz}^0 - \tau_{xy}^0\tau_{xz}^0\tau'_{yz}}{(\tau_{yz}^0)^2},
\end{aligned} \qquad (14)$$

$$f_2(z) = \frac{(\tau'_{xy}\tau^0_{yz} + \tau^0_{xy}\tau'_{yz})\tau^0_{xz} - \tau^0_{xy}\tau^0_{yz}\tau'_{xz}}{(\tau^0_{xz})^2},$$

$$f_3(z) = \frac{(\tau'_{xz}\tau^0_{yz} + \tau^0_{xz}\tau'_{yz})\tau^0_{xy} - \tau^0_{xz}\tau^0_{yz}\tau'_{xy}}{(\tau^0_{xy})^2}.$$

Function $\tau'_{xy}(z)$ is determined by (10) and (13).

For curved plates, the compression pressure $\sigma_z$ at $z = \pm 1$, calculated in the first approximation, remains linear according to (14), whereas the distribution of tangential stresses $\tau_{xz}$ and $\tau_{yz}$ over the layer thickness becomes nonlinear. In this approximation, the sand-pile analogy established in [6] also remains valid for curved plates.

**2.** In the case of a plate formed by conic sections ($\theta$ = const), we can introduce the change of variables

$$\rho = R + y, \quad R\left(\theta - \frac{\pi}{2}\right) = z, \qquad (15)$$
$$R\varphi = x, \quad R\text{—const}$$

and represent expressions (15) in the form

$$\frac{1}{\rho} = \frac{\delta}{1 + \delta y}, \quad \theta = \frac{\pi}{2} + \delta z, \qquad (16)$$
$$\varphi = \delta x, \quad \delta = \frac{1}{R}.$$

In the first approximation, like in (6) and (8), relationships (16), (7), (2), and (1) yield the equations

$$\frac{\partial\sigma'_x}{\partial x} + \frac{\partial\tau'_{xy}}{\partial y} + \frac{\partial\tau'_{xz}}{\partial z} = \frac{\partial\sigma^0_x}{\partial x}y + \frac{\partial\tau^0_{xz}}{\partial z}y - 3\tau^0_{xy},$$
$$\frac{\partial\tau'_{xy}}{\partial x} + \frac{\partial\sigma'_y}{\partial y} + \frac{\partial\tau'_{yz}}{\partial z} = \frac{\partial\tau^0_{xy}}{\partial x}y + \frac{\partial\tau^0_{yz}}{\partial z}y - 2\sigma^0_y + \sigma^0_z + \sigma^0_x, \qquad (17)$$
$$\frac{\partial\tau'_{xz}}{\partial x} + \frac{\partial\tau'_{yz}}{\partial y} + \frac{\partial\sigma'_z}{\partial z} = \frac{\partial\tau^0_{xz}}{\partial x}y + \frac{\partial\sigma^0_z}{\partial z}y - 3\tau^0_{yz}$$

and relationships (9) and (10) remain valid.

From (1) and (17), we find

$$\frac{\partial\sigma'_x}{\partial x} + \frac{\partial\tau'_{xy}}{\partial y} + \frac{\partial\tau'_{xz}}{\partial z} = -3\tau^0_{xy},$$
$$\frac{\partial\tau'_{xy}}{\partial x} + \frac{\partial\sigma'_y}{\partial y} + \frac{\partial\tau'_{yz}}{\partial z} = by + 2 - \frac{3b}{a}\tau^0_{xy}, \qquad (18)$$
$$\frac{\partial\tau'_{xz}}{\partial x} + \frac{\partial\tau'_{yz}}{\partial y} + \frac{\partial\sigma'_z}{\partial z} = -3bz.$$

In this case, the solution takes the form

$$\sigma'_x = -a_1x - b_1y + \frac{b}{2}y^2 + c - \frac{3b}{2}z^2 - f_3(z) + f_1(z),$$
$$\sigma'_y = -a_1x - b_1y + \frac{b}{2}y^2 + c - \frac{3b}{2}z^2 - f_3(z) + f_2(z),$$
$$\sigma'_z = -a_1x - b_1y + \frac{b}{2}y^2 + c - \frac{3b}{2}z^2,$$
$$\tau'_{xz}(z) = a_1z - 3\int\tau^0_{xy}dz + c_1, \quad c_1\text{—const}, \qquad (19)$$
$$\tau'_{yz}(z) = b_1z + 2z - \frac{3b}{a}\int\tau^0_{xy}dz + c_2, \quad c_2\text{—const},$$
$$\int\tau^0_{xy}dz = \frac{ab}{2(a^2+b^2)}\left(2z \pm z\sqrt{1-(a^2+b^2)z^2}\right.$$
$$\left. + \frac{1}{\sqrt{a^2+b^2}}\arcsin\left(z\sqrt{a^2+b^2}\right)\right).$$

According to (19), the plate curvature leads, in the first approximation, to the $by^2/2$ term characterizing the deviation from linearity for the compression stress $\sigma_z$. Linearity is implied by the sand-pile analogy [6].

**3.** In the case of an inclined plate formed by sections $\varphi$ = const, we introduce the change of variables

$$\rho = R + x, \quad R\left(\theta - \frac{\pi}{2}\right) = y, \qquad (20)$$
$$R\varphi = z, \quad R\text{—const}$$

and represent expressions (20) in the form

$$\frac{1}{\rho} = \frac{\delta}{1 + \delta y}, \quad \theta = \frac{\pi}{2} + \delta z, \qquad (21)$$
$$\varphi = \delta x, \quad \delta = \frac{1}{R}.$$

In the first approximation, like in (6) and (8), relationships (21), (7), (2), and (1) yield the equations

$$\frac{\partial\sigma'_x}{\partial x} + \frac{\partial\tau'_{xy}}{\partial y} + \frac{\partial\tau'_{xz}}{\partial z} = \frac{\partial\tau^0_{xy}}{\partial y}x + \frac{\partial\tau^0_{xz}}{\partial z}x - 2\sigma^0_x + \sigma^0_y + \sigma^0_z,$$
$$\frac{\partial\tau'_{xy}}{\partial x} + \frac{\partial\sigma'_y}{\partial y} + \frac{\partial\tau'_{yz}}{\partial z} = \frac{\partial\sigma^0_y}{\partial y}x + \frac{\partial\tau^0_{yz}}{\partial z}x - 3\tau^0_{xy}, \qquad (22)$$
$$\frac{\partial\tau'_{xz}}{\partial x} + \frac{\partial\tau'_{yz}}{\partial y} + \frac{\partial\sigma'_z}{\partial z} = \frac{\partial\tau^0_{yz}}{\partial y}x + \frac{\partial\sigma^0_z}{\partial z}x - 3\tau^0_{xz},$$

and relationships (9) and (10) remain valid.

From (1) and (22), we find that

$$\frac{\partial\sigma'_x}{\partial x} + \frac{\partial\tau'_{xy}}{\partial y} + \frac{\partial\tau'_{xz}}{\partial z} = ax + 2 - \frac{3a}{b}\tau^0_{xy},$$

$$\frac{\partial\tau'_{xy}}{\partial x} + \frac{\partial\sigma'_y}{\partial y} + \frac{\partial\tau'_{yz}}{\partial z} = -3\tau^0_{xy}, \qquad (23)$$

$$\frac{\partial\tau'_{xz}}{\partial x} + \frac{\partial\tau'_{yz}}{\partial y} + \frac{\partial\sigma'_z}{\partial z} = -3az.$$

In this case, the solution takes the form

$$\sigma'_x = -a_1x - b_1y + \frac{a}{2}x^2 + c - \frac{3a}{2}z^2 - f_3(z) + f_1(z),$$

$$\sigma'_y = -a_1x - b_1y + \frac{a}{2}x^2 + c - \frac{3a}{2}z^2 - f_3(z) + f_2(z),$$

$$\sigma'_z = -a_1x - b_1y + \frac{a}{2}x^2 + c - \frac{3a}{2}z^2, \qquad (24)$$

$$\tau'_{xz}(z) = a_1z + 2z - \frac{3a}{b}\int\tau^0_{xy}dz + c_1, \quad c_1\text{—const},$$

$$\tau'_{yz}(z) = b_1z - 3\int\tau^0_{xy}dz + c_2, \quad c_2\text{—const}.$$

According to (24), the plate curvature leads, in the first approximation, to the $bx^2/2$ term characterizing the deviation from linearity for compression stress $\sigma_z$. Linearity is implied by the sand-pile analogy [6].

## REFERENCES


1. L. Prandtl, in *Plasticity Theory* (Inostrannaya Literatura, Moscow, 1948).
2. R. Hill, *Mathematical Theory of Plasticity* (Clarendon Press, Oxford, 1950; Gostekhizdat, Moscow, 1956).
3. D. D. Ivlev, Izv. Akad. Nauk, Mekh. Tverd. Tela, No. 1, 5 (1998).
4. M. A. Zadoyan, *Three-Dimensional Problems of Plasticity Theory* (Nauka, Moscow, 1992).
5. A. Yu. Ishlinskiĭ, Uch. Zap. Mosk. Gos. Univ. **117**, 90 (1946).
6. A. A. Il'yushin, Prikl. Mat. Mekh. **19** (8) (1955).


*Translated by Yu. Verevochkin*

*Doklady Physics, Vol. 45, No. 12, 2000, pp. 680–684. Translated from Doklady Akademii Nauk, Vol. 375, No. 4, 2000, pp. 476–480.*
*Original Russian Text Copyright © 2000 by Polyanin.*

**MECHANICS**

# Partial Separation of Variables in Unsteady Problems of Mechanics and Mathematical Physics

**A. D. Polyanin**

Presented by Academician D.M. Klimov March 2, 2000

Received March 6, 2000

We describe a wide class of linear partial differential equations that have exact solutions in the form of a product of functions of partially separated variables (in contrast to the time coordinate, the spatial coordinates are separated). Problems in which the Green's function admits partial separation of variables are considered. We construct solutions to a number of linear unsteady boundary value problems of the first, second, and third kinds for heat- and mass-transfer equations with variable coefficients. We demonstrate examples of nonlinear equations in mechanics and mathematical physics whose exact solutions depend on partially separated variables.

**1. Preliminary remarks.** The method of separation of variables is one of many widespread methods used for solving linear equations in mathematical physics. This method is based on a search for particular solutions to linear homogeneous equations, which take the form of a product of functions for different variables:

$$w(\mathbf{x}, t) = \varphi_1(x_1)\ldots\varphi_n(x_n)\psi(t), \quad \mathbf{x} = \{x_1, \ldots, x_n\}.$$

Here, $x_1, \ldots, x_n$ are the spatial variables (generalized coordinates) and $t$ is time. The functions $\varphi_1 = \varphi_1(x_1)$, $\ldots$, $\varphi_n = \varphi_n(x_n)$, and $\psi = \psi(t)$ are governed by ordinary differential equations (for details see, e.g., [1–6]). The generalization of this method is based on the search for particular solutions in the form $w(\mathbf{x}, t) = \varphi(\mathbf{x})\psi(t)$.

In this paper, we deal with equations of mechanics and mathematical physics whose particular solutions depend on partially separated variables,

$$w(\mathbf{x}, t) = \varphi_1(x_1, t)\ldots\varphi_n(x_n, t); \tag{1}$$

i.e., the solution is separated with respect to the spatial variables $x_1, \ldots, x_n$, but is not separated with respect to time. In a more general case, we consider solutions having the form

$$w(\mathbf{x}, t) = \varphi(x_1, \ldots, x_k, t)\varphi_k(x_{k+1}, \ldots, x_n, t).$$

*Institute of Problems in Mechanics,*
*Russian Academy of Sciences,*
*pr. Vernadskogo 101, Moscow, 117526 Russia*

**2. Linear equations in partially separated variables.** We consider the linear homogeneous partial differential equation

$$\frac{\partial w}{\partial t} - \sum_{k=1}^{n} L_{k,t}[w] = 0, \tag{2}$$

where

$$L_{k,t}[w] = \sum_{s=0}^{m_k} a_{ks}(x_k, t)\frac{\partial^s w}{\partial x_k^s}, \quad k = 1, \ldots, n. \tag{3}$$

Equations (2) and (3) have particular solutions with partially separated variables in the form of (1), with the functions $\varphi_k = \varphi_k(x_k, t)$ described by one-dimensional partial differential equations:

$$\frac{\partial \varphi_k}{\partial t} - L_{k,t}[\varphi_k] = \lambda_k(t)\varphi_k. \tag{4}$$

The right-hand sides of Eqs. (4) depend on the arbitrary functions $\lambda_1(t), \ldots, \lambda_n(t)$ that satisfy the relationship

$$\sum_{k=1}^{n} \lambda_k(t) = 0.$$

**3. Cauchy problem ($\mathbf{x} \in \mathcal{R}^n$, $t \geq 0$).** The solution to the Cauchy problem for the linear nonhomogeneous equation

$$\frac{\partial w}{\partial t} - \sum_{k=1}^{n} L_{k,t}[w] = \Phi(\mathbf{x}, t) \tag{5}$$

with the initial condition

$$w = f(\mathbf{x}) \quad \text{at} \quad t = 0 \tag{6}$$

can be written out in the form [7]

$$w(\mathbf{x}, t) = \int_0^t \int_{\mathcal{R}^n} \Phi(\mathbf{y}, \tau)\mathcal{E}(\mathbf{x}, \mathbf{y}, t, \tau)d\mathbf{y}d\tau + \int_{\mathcal{R}^n} f(\mathbf{y})\mathcal{E}(\mathbf{x}, \mathbf{y}, t, 0)d\mathbf{y}. \tag{7}$$

Here, $\mathcal{E} = \mathcal{E}(\mathbf{x}, \mathbf{y}, t, \tau)$ is the fundamental solution that, for $t > \tau \geq 0$, satisfies the linear homogeneous equation

$$\frac{\partial \mathcal{E}}{\partial t} - \sum_{k=1}^{n} L_{k,t}[\mathcal{E}] = 0 \tag{8}$$

with a nonhomogeneous initial condition having the particular form

$$\mathcal{E} = \delta(\mathbf{x} - \mathbf{y}) \quad \text{at} \quad t = \tau. \tag{9}$$

Here, $\delta(\mathbf{x})$ is the $n$-dimensional Dirac delta function; the quantities $\tau$ and $\mathbf{y} = \{y_1, \ldots, y_n\}$ serve as free parameters ($\mathbf{y} \in \mathcal{R}^n$). In formula (7), we use the shortened notation $d\mathbf{y} = dy_1 \ldots dy_n$.

Taking into account the explicit form of differential operators (3) and the equality $\delta(\mathbf{x} - \mathbf{y}) = \delta(x_1 - y_1)\ldots\delta(x_n - y_n)$, we can prove that the fundamental solution described by $n$-dimensional equation (8) with initial condition (9) can be written out in the form of the product

$$\mathcal{E}(\mathbf{x}, \mathbf{y}, t, \tau) = \prod_{k=1}^{n} \mathcal{E}_k(x_k, y_k, t, \tau). \tag{10}$$

Here, $\mathcal{E}_k = \mathcal{E}_k(x_k, y_k, t, \tau)$ are the fundamental solutions that satisfy the one-dimensional equations

$$\frac{\partial \mathcal{E}_k}{\partial t} - L_{k,t}[\mathcal{E}_k] = 0, \quad k = 1, \ldots, n,$$

with the initial conditions

$$\mathcal{E}_k = \delta(x_k - y_k) \quad \text{at} \quad t = \tau.$$

In this case, fundamental solution (10) depends on partially separated variables (the solution is separated with respect to the spatial variables but is not separated with respect to time).

**Example 1.** The fundamental solution to the equation

$$\frac{\partial w}{\partial t} = \sum_{k=1}^{n} a_k(t)\frac{\partial^2 w}{\partial x_k^2}, \quad 0 < a_k(t) < \infty$$

is given by formula (10), where

$$\mathcal{E}_k(x_k, y_k, t, \tau) = \frac{1}{2\sqrt{\pi T_k}} \exp\left[-\frac{(x_k - y_k)^2}{4T_k}\right],$$

$$T_k = \int_\tau^t a_k(\eta)d\eta.$$

**Example 2.** The fundamental solution to the three-dimensional Schrödinger equation

$$i\hbar\frac{\partial w}{\partial t} = -\frac{\hbar^2}{m^2}\left(\frac{\partial^2 w}{\partial x_1^2} + \frac{\partial^2 w}{\partial x_2^2} + \frac{\partial^2 w}{\partial x_3^2}\right) + [U_1(x_1, t) + U_2(x_2, t) + U_3(x_3, t)]w$$

also operates with partially separated variables; i.e., it can be represented in the form of a product of three one-dimensional fundamental solutions [see formula (10) for $n = 3$)].

**4. Unsteady boundary value problems of heat- and mass transfer.** The equations

$$\frac{\partial w}{\partial t} - \sum_{k=1}^{n}\left[a_k(x_k, t)\frac{\partial^2 w}{\partial x_k^2} + b_k(x_k, t)\frac{\partial w}{\partial x_k} + c_k(x_k, t)w\right] = \Phi(\mathbf{x}, t), \tag{11}$$

with $0 < a_k(x_k, t) < \infty$, are widely met in the theory of heat- and mass transfer [5, 6, 8].

We consider the domain $V = \{\alpha_k \leq x_k \leq \beta_k, k = 1, \ldots, n\}$, which is an $n$-dimensional parallelepiped. On the faces of this parallelepiped, nonhomogeneous boundary conditions are imposed:

$$\begin{aligned} \sigma_k^{(1)}\frac{\partial w}{\partial x_k} + \nu_k^{(1)}(t)w &= g_k^{(1)}(\mathbf{x}, t), \text{ for } x_k = \alpha_k, \\ \sigma_k^{(2)}\frac{\partial w}{\partial x_k} + \nu_k^{(2)}(t)w &= g_k^{(2)}(\mathbf{x}, t), \text{ for } x_k = \beta_k, \end{aligned} \tag{12}$$

where

$$\left|\sigma_k^{(1,2)}\right| + \left|\nu_k^{(1,2)}(t)\right| > 0,$$

$$\sigma_k^{(1)}\nu_k^{(1)}(t) \leq 0, \quad \sigma_k^{(2)}\nu_k^{(2)}(t) \geq 0.$$

Setting appropriate values of the coefficients $\sigma_k^{(i)}$ and the functions $\nu_k^{(i)} = \nu_k^{(i)}(t)$ ($i = 1, 2$), we can arrive at the boundary conditions of the first, second, and third kinds on each face.

The solution to Eq. (11) with initial condition (6) and homogeneous boundary conditions (12) [for $g_k^{(1)} = g_k^{(2)} = 0$] can be written out in the form

$$w(\mathbf{x}, t) = \int_0^t \int_V \Phi(\mathbf{y}, \tau) G(\mathbf{x}, \mathbf{y}, t, \tau) d\mathbf{y} d\tau + \int_V f(\mathbf{y}) G(\mathbf{x}, \mathbf{y}, t, 0) d\mathbf{y}, \tag{13}$$

where $d\mathbf{y} = dy_1 \ldots dy_n$ and $V = \{\alpha_k \le y_k \le \beta_k, k = 1, \ldots, n\}$. For $t > \tau \ge 0$, the Green's function $G(\mathbf{x}, \mathbf{y}, t, \tau)$ in solution (13) satisfies the linear homogeneous equation

$$\frac{\partial G}{\partial t} - \sum_{k=1}^{n} \left[ a_k(x_k, t) \frac{\partial^2 G}{\partial x_k^2} + b_k(x_k, t) \frac{\partial G}{\partial x_k} + c_k(x_k, t) G \right] = 0 \tag{14}$$

with a nonhomogeneous initial condition of the particular form

$$G = \delta(\mathbf{x} - \mathbf{y}), \text{ for } t = \tau \tag{15}$$

and the homogeneous boundary conditions

$$\sigma_k^{(1)} \frac{\partial G}{\partial x_k} + \nu_k^{(1)}(t) G = 0, \text{ for } x_k = \alpha_k,$$
$$\sigma_k^{(2)} \frac{\partial G}{\partial x_k} + \nu_k^{(2)}(t) G = 0, \text{ for } x_k = \beta_k. \tag{16}$$

The Green's function can be shown to admit partially separated variables:

$$G(\mathbf{x}, \mathbf{y}, t, \tau) = \prod_{k=1}^{n} G_k(x_k, y_k, t, \tau). \tag{17}$$

Here, $G_k = G_k(x_k, y_k, t, \tau)$ are the auxiliary Green's functions that satisfy the one-dimensional equations

$$\frac{\partial G_k}{\partial t} - a_k(x_k, t) \frac{\partial^2 G_k}{\partial x_k^2} - b_k(x_k, t) \frac{\partial G_k}{\partial x_k} - c_k(x_k, t) G_k = 0,$$
$$k = 1, \ldots, n,$$

with the initial condition

$$G_k = \delta(x_k - y_k), \text{ for } t = \tau$$

and the homogeneous boundary conditions

$$\sigma_k^{(1)} \frac{\partial G_k}{\partial x_k} + \nu_k^{(1)}(t) G_k = 0, \text{ for } x_k = \alpha_k,$$
$$\sigma_k^{(2)} \frac{\partial G_k}{\partial x_k} + \nu_k^{(2)}(t) G_k = 0, \text{ for } x_k = \beta_k.$$

Expressions for the auxiliary (one-dimensional) Green's functions for a large number of problems can be found, for example, in [3, 5, 6, 8–10].

The solution to Eq. (11) with initial condition (6) and nonhomogeneous boundary conditions (12) has the form

$$w(\mathbf{x}, t) = \int_0^t \int_V \Phi(\mathbf{y}, \tau) G(\mathbf{x}, \mathbf{y}, t, \tau) d\mathbf{y} d\tau + \int_V f(\mathbf{y}) G(\mathbf{x}, \mathbf{y}, t, 0) d\mathbf{y}$$
$$+ \sum_{k=1}^{n} \int_0^t \int_{S^{(k)}} a_k(\alpha_k, \tau) [g_k^{(1)}(\mathbf{y}, \tau) \Lambda_k^{(1)}(\mathbf{x}, \mathbf{y}, t, \tau)]_{y_k = \alpha_k} dS_y^{(k)} d\tau - \sum_{k=1}^{n} \int_0^t \int_{S^{(k)}} a_k(\beta_k, \tau) [g_k^{(2)}(\mathbf{y}, \tau) \Lambda_k^{(2)}(\mathbf{x}, \mathbf{y}, t, \tau)]_{y_k = \beta_k} dS_y^{(k)} d\tau.$$

Here, we used the following notation ($i = 1, 2$):

$$d\mathbf{y} = dy_1 \ldots dy_n, \quad dS_y^{(k)} = dy_1 \ldots dy_{k-1} dy_{k+1} \ldots dy_n,$$

$$S^{(k)} = \{\alpha_m \le y_m \le \beta_m, \text{ for } m = 1, \ldots, k-1, k+1, \ldots, n\},$$

$$\Lambda_k^{(i)}(\mathbf{x}, \mathbf{y}, t, \tau) = \begin{cases} \dfrac{\partial}{\partial y_k} G(\mathbf{x}, \mathbf{y}, t, \tau) & \text{for } \sigma_k^{(i)} = 0, \ \nu_k^{(i)}(t) = 1 \\ -G(\mathbf{x}, \mathbf{y}, t, \tau) & \text{for } \sigma_k^{(i)} = 1, \text{ and } \nu_k^{(i)}(t) \text{ is arbitrary.} \end{cases}$$

**5. Linear equations. Certain generalizations.** We consider the equation of the form

$$\frac{\partial w}{\partial t} - L_{1,\ldots,s;\,t}[w] - M_{s+1,\ldots,n;\,t}[w] = 0, \qquad (18)$$

where $L_{1,\ldots,s;\,t}[w]$ and $M_{s+1,\ldots,n;t}[w]$ are linear differential operators (of an arbitrary order) related to the variables $x_1, \ldots, x_s$, and $x_{s+1}, \ldots, x_n$, respectively. The operator coefficients depend on the corresponding sets of variables and time $t$.

Equation (18) has particular solutions with partially separated variables, which take the form

$$w(\mathbf{x}, t) = \varphi(x_1, \ldots, x_s, t)\psi(x_{s+1}, \ldots, x_n, t).$$

The fundamental solution to the Cauchy problem for Eq. (18) also depends on partially separated variables.

**6. Nonlinear equations. Hamilton–Jacobi equation.** We now describe the nonlinear partial differential equations that have exact solutions with partially separated variables.

The nonlinear equations

$$\frac{\partial w}{\partial t} + \sum_{k=1}^{n} F_k\left(x_k, t, \frac{\partial w}{\partial x_k}, \ldots, \frac{\partial^m w}{\partial x_k^m}\right) + g(t)w = 0 \qquad (19)$$

have exact solutions in the form of a sum,

$$w(\mathbf{x}, t) = \sum_{k=1}^{n} w_k(x_k, t), \qquad (20)$$

where the functions $w_k = w_k(x_k, t)$ satisfy simpler equations in one spatial variable:

$$\frac{\partial w_k}{\partial t} + F_k\left(x_k, t, \frac{\partial w_k}{\partial x_k}, \ldots, \frac{\partial^m w_k}{\partial x_k^m}\right) + g(t)w_k = \lambda_k(t). \qquad (21)$$

Here, $\lambda_k(t)$ are arbitrary functions interrelated by the equality $\sum_{k=1}^{n} \lambda_k(t) = 0$.

**Example 3.** We consider in more detail the equation of the first order (Hamilton–Jacobi equation) which corresponds to the case $m = 1$ in (19). We seek the complete solution to this equation in the form of (20), where the functions $w_k = w_k(x_k, t)$ satisfy Eqs. (21) with $\lambda_k(t) = 0$. It is easy to verify that the complete solutions to Eqs. (21) take the form

$$w_k = u_k(x_k, t, C_k) + A_k \exp\left[-\int g(t)dt\right],$$
$$k = 1, 2, \ldots, n,$$

where $A_k$ and $C_k$ are arbitrary constants. Substituting these expressions into (20), we arrive at the solution

$$w = \sum_{k=1}^{n} u_k(x_k, t, C_k) + C_{n+1}\exp\left[-\int g(t)dt\right],$$

$$C_{n+1} = \sum_{k=1}^{n} A_k;$$

this solution depends on $n + 1$ arbitrary constants.

**7. Nonlinear equations. Heat- and mass-transfer equations.** Nonlinear partial differential equations

$$\frac{\partial w}{\partial t} + w\sum_{k=1}^{n} F_k\left(x_k, t, \frac{1}{w}\frac{\partial w}{\partial x_k}, \ldots, \frac{1}{w}\frac{\partial^m w}{\partial x_k^m}\right) + g(t)w\ln w = 0 \qquad (22)$$

have exact solutions in the form of a product:

$$w(\mathbf{x}, t) = \prod_{k=1}^{n} w_k(x_k, t). \qquad (23)$$

Here, the functions $w_k = w_k(x_k, t)$ satisfy simpler equations having one spatial variable:

$$\frac{\partial w_k}{\partial x} + w_k F_k\left(x_k, t, \frac{1}{w_k}\frac{\partial w_k}{\partial x_k}, \ldots, \frac{1}{w_k}\frac{\partial^m w_k}{\partial x_k^m}\right) + g(t)w_k\ln w_k + \lambda_k(t)w_k = 0, \qquad (24)$$

where $\lambda_k(t)$ are arbitrary functions interrelated by the equality $\sum_{k=1}^{n} \lambda_k(t) = 0$.

**Example 4.** A particular anisotropic case of Eq. (22) for $n = m = 2$ yields a nonlinear unsteady equation (of heat- and mass-transfer theory or combustion theory) with a source of a logarithmic type for an arbitrary coordinate dependence of the principal thermal-diffusivity coefficients:

$$\frac{\partial w}{\partial t} = \frac{\partial}{\partial x}\left[f_1(x)\frac{\partial w}{\partial x}\right] + \frac{\partial}{\partial y}\left[f_2(y)\frac{\partial w}{\partial y}\right] + \beta w\ln w. \qquad (25)$$

Equation (25) has exact solutions of the form

$$w(x, y, t) = u(x, t)v(y, t).$$

Here, the functions $u(x, t)$ and $v(y, t)$ are determined by two independent one-dimensional nonlinear differential parabolic equations:

$$\frac{\partial u}{\partial t} = \frac{\partial}{\partial x}\left[f_1(x)\frac{\partial u}{\partial x}\right] + \beta u\ln u + C(t)u,$$

$$\frac{\partial v}{\partial t} = \frac{\partial}{\partial y}\left[f_2(y)\frac{\partial v}{\partial y}\right] + \beta v\ln v - C(t)v,$$

where $C(t)$ is an arbitrary function.

It is worth noting that, in the case of the constant coefficients in Eq. (25) [i.e., $f_1(x) = a$ and $f_2(y) = b$], there are exact solutions in the form of a product of traveling waves:

$$w(x, y, t) = U(\xi)V(\eta), \quad \xi = x + c_1 t, \quad \eta = y + c_2 t,$$

where $c_1$ and $c_2$ are arbitrary constants.

## ACKNOWLEDGMENTS

This work was performed under the financial support of the Russian Foundation for Basic Research, projects nos. 00-02-18033 and 00-03-32055.

## REFERENCES

1. A. N. Tikhonov and A. A. Samarskiĭ, *Equations of Mathematical Physics*, 4th ed. (Nauka, Moscow, 1972; Pergamon, Oxford, 1964).
2. V. S. Vladimirov, *Equations of Mathematical Physics* (Nauka, Moscow, 1988; Marcel Dekker, New York, 1971).
3. S. G. Mikhlin, *Linear Equations of Mathematical Physics* (Nauka, Moscow, 1964; Holt, Rinehart and Winston, New York, 1967).
4. G. N. Polozhiĭ, *Equations of Mathematical Physics* (Vysshaya Shkola, Moscow, 1964).
5. H. S. Carslaw and J. C. Jaeger, *Conduction of Heat in Solids* (Clarendon, Oxford, 1959; Nauka, Moscow, 1964).
6. A. V. Lykov, *Theory of Heat Conductivity* (Vysshaya Shkola, Moscow, 1967).
7. *Mathematical Encyclopedia* (Sov. Éntsiklopediya, Moscow, 1977), Vol. 1, p. 1130.
8. A. D. Polyanin, A. V. Vyaz'min, A. I. Zhurov, and D. A. Kazenin, *Handbook for Exact Solutions of Heat- and Mass-Transfer Equations* (Faktorial, Moscow, 1998).
9. V. F. Zaĭtsev and A. D. Polyanin, *Handbook on Partial Differential Equations: Exact Solutions* (Mezhdunarodnaya Progr. Obrazovaniya, Moscow, 1996).
10. A. G. Butkovskiĭ, *Green's Functions and Transfer Functions Handbook* (Nauka, Moscow, 1979; Horwood, Chichester, England, 1982).

*Translated by V. Chechin*

*Doklady Physics, Vol. 45, No. 12, 2000, pp. 685–689. Translated from Doklady Akademii Nauk, Vol. 375, No. 5, 2000, pp. 622–626.*
*Original Russian Text Copyright © 2000 by Vorotnikov.*

**MECHANICS**

# Theory of Stability with Respect to a Part of the Variables and the Problem of Coordinate Synchronization for Dynamical Systems

**V. I. Vorotnikov**

Presented by Academician V.V. Rumyantsev April 10, 2000

Received April 10, 2000

A growing number of studies has recently been devoted to the problem of synchronization of motions [1], which stems back to Huygens and is important in modern applications. Among them, the problem of coordinate synchronization for dynamical systems was considered in a fairly general mathematical form [2–4]. In this case, an asymptotic coincidence for a part of (or for all) the phase-space vector coordinates related to two or more dynamical (among them, controllable) systems must be provided. This problem has been exciting keen interest since coordinate synchronization was proven to be possible for chaotic processes as well as for regular ones and closely related to the problem of safe communication.

For example, let there be two interrelated systems

$$\dot{\mathbf{x}}^i = \mathbf{X}^i(t, \mathbf{x}^1, \mathbf{x}^2, \mathbf{u}) \quad i = 1, 2, \tag{1}$$

where $\mathbf{x}^i = (\mathbf{y}^{i\mathrm{T}}, \mathbf{z}^{i\mathrm{T}})^\mathrm{T}$ are the phase-space vectors (the symbol T stands for transposition), $\dim(\mathbf{y}^1) = \dim(\mathbf{y}^2)$, and $\mathbf{u}$ is a control vector.

The problem of controlled coordinate synchronization is reduced to choosing a control vector [2–4],

$$\mathbf{u} = \mathbf{u}(t, \mathbf{x}^1, \mathbf{x}^2), \tag{2}$$

in set (1) such that the relationship

$$\left\|\mathbf{y}^1(t;\, t_0, \mathbf{x}_0^1, \mathbf{x}_0^2) - \mathbf{y}^2(t;\, t_0, \mathbf{x}_0^1, \mathbf{x}_0^2)\right\| \longrightarrow 0 \quad (\text{as } t \longrightarrow \infty)$$

would be satisfied for all $\mathbf{y}^i$th components of the solutions $\mathbf{x}^i(t;\, t_0,\, \mathbf{x}_0^1,\, \mathbf{x}_0^2)$ that originate within the given range of the initial values $\mathbf{x}_0^i$.

Using the substitution $\mathbf{w} = \mathbf{y}^1 - \mathbf{y}^2$, we can reduce this problem to a corresponding problem for the convergence of motions with respect to a part of the variables ($\mathbf{w}$-convergence) which is related to the combined system of differential equations

$$\dot{\mathbf{w}} = \mathbf{X}^*(t, \mathbf{w}, \mathbf{x}^1, \mathbf{x}^2, \mathbf{u}), \quad \dot{\mathbf{x}}^i = \mathbf{X}^i(t, \mathbf{x}^1, \mathbf{x}^2, \mathbf{u}), \quad i = 1, 2. \tag{3}$$

In other words, we need to choose control vector (2) in set (3) such that the relationship $\|\mathbf{w}\| \longrightarrow 0$ as $t \longrightarrow \infty$ would be satisfied for all the solutions that originate in a given range of the initial values $\mathbf{w}_0$ and $\mathbf{x}_0^i$.

Modifications of this problem are possible. For example, the requirement of $\mathbf{w}$-convergence can be substituted by a stronger requirement of asymptotic (in particular, uniform) stability for the $\mathbf{y}^i$th-components of the solutions to set (1) and (2). Thus, the corresponding problem of the asymptotic $\mathbf{w}$-stability for set (3) can be posed. Studying such problems is necessitated by the character in itself of the initial problem for coordinate synchronization. These problems can be solved within the framework of the theory of stability with respect to a part of the variables (partial stability) [6–11].

In this paper, both the notion and conditions of partial asymptotic stability are modified, so that the problems of coordinate synchronization for two dynamical systems can be analyzed both in part and as a whole. As an example, we consider coordinate synchronization as a whole for angular motions of two solid bodies.

**1. Statement of the problem.** The specific nature of the problem of synchronization is responsible for certain peculiarities in the formulation of the problems of partial asymptotic stability and partial convergence of motions.

Introducing the notation $\mathbf{y} = \mathbf{w}$ and $\mathbf{z} = (\mathbf{x}^{1\mathrm{T}}, \mathbf{x}^{2\mathrm{T}})^\mathrm{T}$, we reduce set (3) to the form

$$\dot{\mathbf{x}} = \mathbf{X}(t, \mathbf{x}), \quad \mathbf{x} = (\mathbf{y}^\mathrm{T}, \mathbf{z}^\mathrm{T})^\mathrm{T} \in R^n, \tag{4}$$

which is conventional in the theory of partial stability ($\mathbf{y}$-stability), see [6–11].

The synchronization in part can be studied on the basis of one of the possible modified notions of partial

*Nizhniĭ Tagil Institute of Ural State Technical University, ul. Krasnogvardeĭskaya 59, Nizhniĭ Tagil, 622031 Russia*

asymptotic stability, namely, the asymptotic **y**-stability of the set $\mathbf{x} = \mathbf{0}$ in part for large $\mathbf{z}_0$ [10, 11]. However, it is quite possible that this set is not the solution to Eqs. (4). This property of partial asymptotic stability ensures that the solutions $\mathbf{x}^i = \mathbf{x}(t; t_0, \mathbf{x}_0^i)$ to sets (1) will be close to and synchronized with them under sufficiently close initial conditions; whereas, the initial conditions $\mathbf{x}_0^i$ may differ by an arbitrary finite value $\Delta > 0$.

The synchronization as a whole can be studied within the framework of the problem of asymptotic **y**-stability as a whole of the set $\mathbf{x} = \mathbf{0}$. However, in contrast to the results of [6–11], the global convergence to the set $\mathbf{x} = \mathbf{0}$ must be combined with the **y**-stability of this set for large $\mathbf{z}_0$.

We now make the corresponding definitions more precise.

**Definition 1.** *The set* $\mathbf{x} = \mathbf{0}$ *is referred to as an asymptotically* **y**-*stable set for large* $\mathbf{z}_0$ *if it is* **y**-*stable for large* $\mathbf{z}_0$ {*i.e., for each* $\varepsilon > 0$ *and* $t_0 \geq 0$ *there exists a quantity* $\delta(\varepsilon, t_0) > 0$, *such that* $\|\mathbf{y}(t; t_0, \mathbf{x}_0)\| < \varepsilon$ *for all* $t \geq t_0$ *provided that* $\|\mathbf{y}_0\| < \delta$ *and* $\|\mathbf{z}_0\| \leq \Delta < \infty$}, *and, in addition, this set is* **y**-*attracting for large* $\mathbf{z}_0$; *i.e.,*

$$\lim\|\mathbf{y}(t; t_0, \mathbf{x}_0)\| = 0, \quad t \longrightarrow \infty, \tag{5}$$

*for all* $t_0$ *and* $\mathbf{x}_0$ *in the domain* $S$: $\{t_0 \geq 0, \|\mathbf{y}_0\| < \delta, \|\mathbf{z}_0\| \leq \Delta < \infty\}$.

*The set* $\mathbf{x} = \mathbf{0}$ *is referred to as uniformly asymptotically* **y**-*stable for large* $\mathbf{z}_0$ *if it is uniformly* **y**-*stable for large* $\mathbf{z}_0$ (*with* $\delta$ *being independent of* $t_0$) *and relationship* (5) *is satisfied uniformly with respect to* $t_0$ *and* $\mathbf{x}_0$ *in the domain* $S$.

**Definition 2.** *The set* $\mathbf{x} = \mathbf{0}$ *is referred to as* (*uniformly*) **y**-*attracting as a whole if relationship* (5) *is satisfied* (*uniformly with respect to* $t_0 \geq 0$ *and* $\mathbf{x}_0 \in K$, *where* $K$ *is an arbitrary compact set of the space* $\mathbf{x} \in R^n$) *for all* $t_0$ *and* $\mathbf{x}_0$ *in the domain* $t_0 \geq 0$ *and* $\|\mathbf{x}_0\| < \infty$.

Furthermore, we employ a modified method of the Lyapunov functions for solving the problems of partial asymptotic stability in the sense of Definitions 1 and 2.

**2. Conditions for synchronization in part within the framework of the method of the Lyapunov functions.** One of the modified methods of the Lyapunov functions was proposed in [11, 12]. It is reduced to adjusting the structure of the domain in which the Lyapunov functions are constructed. As applied to the problem under consideration, the method is reduced to restricting the domain

$$t \geq 0, \quad \|\mathbf{y}\| \leq h, \quad \|\mathbf{z}\| < \infty \tag{6}$$

($h > 0$ is a sufficiently small number), which is conventionally used when studying the **y**-stability for the set $\mathbf{x} = \mathbf{0}$ of Eqs. (4). This domain is substituted by the domain

$$t \geq 0, \quad \|\mathbf{y}\| + \|\mathbf{W}(t, \mathbf{x})\| \leq h, \quad \|\mathbf{z}\| < \infty, \tag{7}$$

where $\mathbf{W}(t, \mathbf{x})$ is the vector function. In this case, the assumption introduced, $\|\mathbf{y}\| + \|\mathbf{W}(t, \mathbf{x})\| \leq h$, should be naturally confirmed in the course of solving the problem.

Studying the problem of **y**-stability in domain (7) is advisable because, in fact, the **y**-stable set $\mathbf{x} = \mathbf{0}$ for Eqs. (4) is also stable with respect to certain functions $W_i = W_i(t, \mathbf{x})$. Because the $W_i$-functions are not always predetermined, they are naturally treated as components of an additional vector Lyapunov **W**-function. This function is introduced to make the substitution of domain (6) by domain (7) the most efficient possible. In this case, the derivative of the **W**-function along the trajectories of set (4) need not be analyzed; this is an additional argument in favor of the approach under consideration.

We employ this method for solving the problem of the asymptotic **y**-stability of the set $\mathbf{x} = \mathbf{0}$ of Eqs. (4) for large $\mathbf{z}_0$.

We assume that set (4) is continuous in domain (6) and its solutions are unique and **z**-extendible. These assumptions are conventional in the theory of stability with respect to a part of the variables. We will consider two classes of functions:

($1^0$.) The functions $a_i(r)$: $R^1 \longrightarrow R^1$ ($i = \overline{1, 3}$) that are continuous, increase monotonically for $r \in [0, h]$, and satisfy the condition $a_i(0) = 0$.

($2^0$.) The scalar function $V(t, \mathbf{x})$: $R^{n+1} \longrightarrow R^1$, $V(t, \mathbf{0}) \equiv 0$ and two vector functions $\mathbf{W}(t, \mathbf{x})$: $R^{n+1} \longrightarrow R^q$, $\mathbf{W}(t, \mathbf{0}) \equiv \mathbf{0}$, and $\mathbf{U}(t, \mathbf{x})$: $R^{n+1} \longrightarrow R^s$, $\mathbf{U}(t, \mathbf{0}) \equiv \mathbf{0}$, with $\mathbf{U} = (U_1, \ldots, U_s)$, where $q$ and $s$ are positive numbers assigned in accordance with the particular problem to be solved.

**Theorem 1.** *Let there exist a scalar function* $V$ *and two vector functions* **U** *and* **W** *such that the following conditions are satisfied in domain* (7):

(*1*) $V(t, \mathbf{x}) \geq a_1(\|\mathbf{y}\| + \|\mathbf{W}(t, \mathbf{x})\|)$;

(*2*) $V(t, \mathbf{x}) = 0$, *for* $\mathbf{y} = \mathbf{0}$;

(*3*) $\dot{V}(t, \mathbf{x}) \leq -a_2(\|\mathbf{U}(t, \mathbf{x})\|)$; $\|\mathbf{U}(t, \mathbf{x})\| \geq a_3(\|\mathbf{y}\|)$;

(*4*) *a number* $M(t_0, \mathbf{x}_0) > 0$ *can be found such that either* $\dot{U}_i \geq M$ *or* $\dot{U}_i \geq -M$ *for each of the functions* $\dot{U}_i$.

*Then, the set* $\mathbf{x} = \mathbf{0}$ of *set* (4) *is asymptotically* **y**-*stable for large* $\mathbf{z}_0$.

**Proof.** For each $\varepsilon > 0$ and $t_0 \geq 0$, by virtue of both the fact that $V(t, \mathbf{0}) \equiv 0$ and condition (*2*) of Theorem 1, the function $\delta(\varepsilon, t_0) > 0$ can be found such that $V(t_0, \mathbf{x}_0) < a_1(\varepsilon)$ if $\|\mathbf{y}_0\| < \delta$ and $\|\mathbf{z}_0\| \leq \Delta < \infty$. Therefore, for any

solution $\mathbf{x}(t;\, t_0, \mathbf{x}_0)$ to set (4), with $\|\mathbf{y}_0\| < \delta$ and $\|\mathbf{z}_0\| \le \Delta$ for all $t \ge t_0$, we have

$$a_1(\|\mathbf{y}(t;\, t_0, \mathbf{x}_0)\| + \|\mathbf{W}(t, \mathbf{x}(t;\, t_0, \mathbf{x}_0))\|)$$
$$\le V(t, \mathbf{x}(t;\, t_0, \mathbf{x}_0)) \le V(t_0, \mathbf{x}_0) < a_1(\varepsilon).$$

Allowing for the properties of function $a_1(r)$, we conclude that $\|\mathbf{y}(t;\, t_0, \mathbf{x}_0)\| + \|\mathbf{W}(t;\, t_0, \mathbf{x}_0)\| < \varepsilon$ for $t \ge t_0$ if $\|\mathbf{y}_0\| < \delta$ and $\|\mathbf{z}_0\| \le \Delta$. Therefore, the set $\mathbf{x} = \mathbf{0}$ of Eqs. (4) is $\mathbf{y}$-stable for large $\mathbf{z}_0$.

We now prove that $\lim\|\mathbf{U}(t, \mathbf{x}\ (t;\, t_0, \mathbf{x}_0))\| = 0$ as $t \longrightarrow \infty$ if $\|\mathbf{y}_0\| < \delta$ and $\|\mathbf{z}_0\| \le \Delta$. Employing the method described in [7, 13], we use the proof by contradiction: Let there exist a number $l > 0$, a value $\mathbf{x}_*$ with $\|\mathbf{y}_*\| < \delta$ and $\|\mathbf{z}_*\| \le \Delta$, and a sequence $t_k \longrightarrow \infty$ with $t_k - t_{k-1} \ge \alpha > 0$, $k = 1, 2, 3, \ldots$, such that

$$\|\mathbf{U}(t_k, \mathbf{x}(t_k;\, t_0, \mathbf{x}_*))\| \ge l, \quad k = 1, 2, 3, \ldots. \tag{8}$$

If condition (*4*) of Theorem 1 is satisfied, we can find a number $\beta$ $(0 < \beta < \alpha)$, such that

$$\frac{1}{2}l \le \|\mathbf{U}(t, \mathbf{x}(t;\, t_0, \mathbf{x}_*))\| \le h,$$
$$t \in T_k = [t_k - \beta, t_k + \beta] \tag{9}$$

for all $k = 1, 2, 3, \ldots$ if $\|\mathbf{y}_*\| < \delta$ and $\|\mathbf{z}_*\| \le \Delta$.

Then, by virtue of (9) and condition (*3*) of Theorem 1, provided that $\|\mathbf{y}_*\| < \delta$ and $\|\mathbf{z}_*\| \le \Delta$, the inequalities

$$\dot{V}(t, \mathbf{x}) \le -a_2(\|\mathbf{U}\|) \le -a_2\left(\frac{1}{2}l\right), \quad t \in T_k$$

are valid along the solutions $\mathbf{x} = \mathbf{x}(t;\, t_0, \mathbf{x}_*)$. Hence,

$$0 \le V(t_k + \beta, \mathbf{x}(t_k + \beta, t_0, \mathbf{x}_0)) \le V(t_0, \mathbf{x}_0)$$
$$+ \sum_{i=1}^{k} \int_{t_i - \beta}^{t_i + \beta} \dot{V}(\tau, \mathbf{x}(\tau; t_0, \mathbf{x}_*))d\tau \le V(t_0, \mathbf{x}_0) - 2k\beta a_2\left(\frac{1}{2}l\right);$$

these inequalities cannot be valid for a sufficiently large $k$.

Thus, assumption (8) is incorrect. Therefore, $\lim a_3(\|\mathbf{y}(t;\, t_0, \mathbf{x}_0)\|) = 0$ as $t \longrightarrow \infty$ and relationship (5) is valid for all $t_0 \ge 0$, $\|\mathbf{y}_0\| < \delta$, and $\|\mathbf{z}_0\| \le \Delta$. The theorem is proven.

**Remarks to Theorem 1.** (i) If condition (*2*) of Theorem 1 is excluded, then Theorem 1 coincides with the corresponding result of [12], which strengthens Theorem 22.2 in [7] for $\mathbf{W} = \mathbf{0}$ and is based on concepts [13] stemming back to the classical Marachkov theorem. In this connection, we emphasize that the nonuniformity of the asymptotic $\mathbf{y}$-stability is typical for theorems of the Marachkov type [7], which follow from Theorem 1 provided that $\mathbf{U} = \mathbf{y}$, $\mathbf{W} = \mathbf{0}$, and condition (*2*) is rejected.

(ii) For $\mathbf{W} \ne \mathbf{0}$, the quantity $\|\mathbf{U}\|$, as well as $V$ and $\dot{V}$, could not be of fixed sign either with respect to $\mathbf{y}$ [6, 7] or in the Lyapunov sense. Moreover, condition (*4*) is verified in domain (7) but not in domain (6), thereby extending the possibility of employing the theorem.

**Corollary.** *Let there exist the scalar function $V$ and the vector function* $\mathbf{U}$, *such that for all the solutions* $\mathbf{x}(t;\, t_0, \mathbf{x}_0)$ *to set* (4) *which originate in the domain* $t_0 \ge 0$, $\|\mathbf{y}_0\| < \delta$, *and* $\|\mathbf{z}_0\| \le \Delta < \infty$ *conditions* (*3*) *and* (*4*) *of Theorem* 1 *are satisfied and, moreover,*

$$V(t, \mathbf{x}(t;\, t_0, \mathbf{x}_0)) \ge -A \quad (A = \text{const} > 0). \tag{10}$$

*Then, the set* $\mathbf{x} = \mathbf{0}$ *of Eqs.* (4) *is* $\mathbf{y}$-*attracting for large* $\mathbf{z}_0$.

**Proof.** We prove by contradiction that relationship (8) is valid. Using the proof scheme of Theorem 1, we have, by virtue of conditions (*3*) and (*4*) of this theorem, for $t_0 \ge 0$, $\|\mathbf{y}_0\| < \delta$ and $\|\mathbf{z}_0\| \le \Delta$:

$$-A \le V(t_0, \mathbf{x}_0) - 2k\beta a_2\left(\frac{1}{2}l\right). \tag{11}$$

This inequality is impossible for sufficiently large $k$. The corollary is proven.

The condition of uniform synchronization in part can be obtained by employing the method of Lyapunov functions together with the differential inequalities given in [14].

**Theorem 2.** *Let there exist the scalar function $V$ and the vector function* $\mathbf{W}$, *such that in domain* (7):

(I) *conditions* (*1*) *and* (*2*) *of Theorem* 1 *are satisfied and, moreover,* $V(t, \mathbf{x}) \le a_2(\|\mathbf{x}\|)$;

(II) $\dot{V} \le \omega(t, V)$, *with the zero solution* $v = 0$ *to the comparison set* $\dot{v} = \omega(t, v)$, *is uniformly asymptotically stable.*

*Then, the set* $\mathbf{x} = \mathbf{0}$ *of Eqs.* (4) *is uniformly asymptotically* $\mathbf{y}$-*stable for large* $\mathbf{z}_0$.

The theorem is proven in the same way as in [14] and with regard to the first part of the proof of Theorem 1.

**Conditions of synchronization as a whole within the framework of the method of Lyapunov functions.** The conditions given can also be obtained on the basis of concepts associated with employing the Marachkov-type theorems and differential inequalities.

**Theorem 3.** *Let there exist the scalar function $V$ and the vector function* $\mathbf{U}$, *such that for all the solutions* $\mathbf{x}(t;\, t_0, \mathbf{x}_0)$ *to set* (4) *which are initiated in the domain* $t_0 \ge 0$ *with* $\|\mathbf{x}_0\| < \infty$ *condition* (10) *as well as conditions* (*3*) *and* (*4*) *of Theorem* 1 *are satisfied.*

*Then, the set* $\mathbf{x} = \mathbf{0}$ *of Eqs.* (4) *is* $\mathbf{y}$-*attracting as a whole.*

**Proof.** We prove by contradiction that relationship (8) holds. Using the proof scheme of Theorem 1, with arbitrary $\mathbf{x}_0$ and $t_0 \geq 0$, and by virtue of condition (*2*) of Theorem 1, we arrive at inequalities (11), which are contradictory for sufficiently large *k*. Hence, relationship (5) holds for all $\mathbf{x}_0$ and $t_0 \geq 0$. The theorem is proven.

**Remarks to Theorem 3.** (*1⁰*) *For* $\mathbf{U} = \mathbf{y}$, *condition* (*4*) *of Theorem* 1 *turns into a requirement imposed on set* (4), *i.e., that its right-hand sides corresponding to a* **y**-*component of the vector* **x** *should be bounded for all* $\mathbf{x}_0$ *and* $t_0 \geq 0$.

(*2⁰*) *Combining the hypotheses of Theorem* 3 *and the conditions of* **y**-*stability for large* $\mathbf{z}_0$ [10, 11], *we can obtain the conditions of asymptotic* **y**-*stability for large* $\mathbf{z}_0$ *and, simultaneously, of* **y**-*attraction as a whole.*

**Theorem 4.** *Let there exist a scalar function V, such that in the domain* $t \geq 0$ *and* $\|\mathbf{x}\| < \infty$, *the following conditions hold*:

(*a*) $V(t, \mathbf{x}) \geq a_1(\|\mathbf{y}\|)$; $V(t, \mathbf{x}) \leq a_2(\|\mathbf{x}\|)$;

(*b*) $V(t, \mathbf{x}) = 0$, *for* $\mathbf{y} = \mathbf{0}$;

(*c*) $\dot{V} \leq -\alpha V$, $\alpha = \text{const} > 0$.

*Then, the set* $\mathbf{x} = \mathbf{0}$ *of Eqs.* (4) *is asymptotically* **y**-*stable for large* $\mathbf{z}_0$ *and, simultaneously, uniformly* **y**-*attracting as a whole.*

**4. Synchronization of angular motions of two solid bodies.** We consider the problem of coordinate synchronization of angular motions of two solid bodies. In this case, the equations of motion take the form ($i = 1, 2$)

$$\begin{aligned} A_1\dot{x}_1^i &= (A_2 - A_3)x_2^i x_3^i + u_1^i, \\ A_2\dot{x}_2^i &= (A_3 - A_1)x_1^i x_3^i + u_2^i, \\ A_3\dot{x}_3^i &= (A_1 - A_2)x_1^i x_2^i + u_3^i. \end{aligned} \tag{12}$$

Here, $A_j$ ($j = \overline{1, 3}$) are the principal central moments of inertia for these bodies (identical for both bodies); $x_j^i$ are the components of the instantaneous angular velocity, which are taken along the principal central axes of inertia (they are combined into the vectors $\mathbf{x}^1$ and $\mathbf{x}^2$); and $u_j^i$ are the control moments applied to the first ($i = 1$) and second ($i = 2$) bodies and combined into the vectors $\mathbf{u}^1$ and $\mathbf{u}^2$.

We need to find the control vectors $\mathbf{u}^1$ and $\mathbf{u}^2$, such that the limiting relationship

$$\mathbf{x}^1(t) \longrightarrow \mathbf{x}^2(t), \quad t \longrightarrow \infty \tag{13}$$

would be valid for all motions $\mathbf{x}^i(t) = \mathbf{x}^i(t;\ t_0,\ \mathbf{x}_0^i)$ of these bodies (with arbitrary initial values $\mathbf{x}_0^1$ and $\mathbf{x}_0^2$).

We now prove that the simplest control vectors (coupled synchronization)

$$\begin{gathered} u_j^1 = \alpha_j(x_j^1 - x_j^2), \quad u_j^2 = \alpha_j(x_j^2 - x_j^1), \\ \alpha_j = \text{const} < 0, \quad j = \overline{1, 3} \end{gathered} \tag{14}$$

represent the solution to this problem.

To prove this, we use the Lyapunov function

$$V = \frac{1}{2}\left[\sum A_j(x_j^1 - x_j^2)^2 + \sum A_j(x_j^1 + x_j^2)^2\right], \tag{15}$$

whose derivative $\dot{V}$ by virtue of closed set (12) and (14) takes the form

$$\dot{V} = \sum A_j\alpha_j(x_j^1 - x_j^2)^2,$$

where the summation over *j* from 1 to 3 is implied.

Since $V = \frac{1}{2}\left\{\sum A_j[(x_j^1)^2 + (x_j^2)^2]\right\}$, with $V \longrightarrow \infty$ as $\|\mathbf{x}^1\| + \|\mathbf{x}^2\| \longrightarrow \infty$, then all solutions to set (12) and (14) are bounded. Introducing the notation $y_j = x_j^1 - x_j^2$ and $\mathbf{y} = (y_1, y_2, y_3)^T$, we can easily verify that the function *V* (15) satisfies the hypotheses of Theorem 3 for $\mathbf{U} = \mathbf{y}$. Whence it follows that relationship (13) is satisfied for set (12), (14).

**5. Conclusions.** In this paper, we employed the theory of stability with respect to a part of the variables for solving the problems of coordinate synchronization for dynamical systems. To consider these problems, we modified both the notion of asymptotic stability with respect to a part of the variables and a number of theorems concerning the method of Lyapunov functions and determining the conditions for this stability.

A different approach to the problem of coordinate synchronization for dynamical systems, which is also based on the notions of stability with respect to a part of the variables, was proposed in [15].

## ACKNOWLEDGMENTS

This work was supported by the Russian Foundation for Basic Research, project no. 99-01-00965.

## REFERENCES

1. I. I. Blekhman, *Synchronization in Science and Technology* (ASME Press, New York, 1988).
2. K. Cuomo, A. Oppenhaim, and S. Strogatz, Int. J. Bifurcation Chaos Appl. Sci. Eng. **3**, 1629 (1993).
3. I. I. Blekhman, P. S. Landa, and M. G. Rozemblum, Appl. Mech. Rev. **48**, 733 (1995).

4. H. Nijmeijer, I. I. Blekhman, A. L. Fradkov, and A. Yu. Pogromski, Syst. Control Lett. **31**, 299 (1997).
5. L. M. Pecora and T. L. Carroll, Phys. Rev. Lett. **64**, 821 (1990).
6. V. V. Rumyantsev, Vestn. Mosk. Univ., Ser. Mat., Mekh., Astron., Fiz., Khim., No. 4, 9 (1957).
7. V. V. Rumyantsev and A. S. Oziraner, *Motion Stability and Stabilization with Respect to a Part of the Variables* (Nauka, Moscow, 1987).
8. L. Hatvani, Alkalm. Mat. Lap. **15** (1/2), 1 (1990/1991).
9. A. S. Andreev, Prikl. Mat. Mekh. **55**, 539 (1991).
10. V. I. Vorotnikov, *Stability of Dynamical Systems with Respect to a Part of the Variables* (Nauka, Moscow, 1991).
11. V. I. Vorotnikov, *Partial Stability and Control* (Birkhauser, Boston, 1998).
12. V. I. Vorotnikov, Prikl. Mat. Mekh. **63**, 736 (1999).
13. L. Salvadori, Ann. Soc. Sci. Bruxelles, Ser. 1 **88**, 183 (1974).
14. C. Corduneanu, Rev. Roum. Math. Pures Appl. **9**, 229 (1964).
15. C. W. Wu and L. O. Chua, Int. J. Bifurcation Chaos Appl. Sci. Eng. **4**, 979 (1994).

*Translated by V. Chechin*

*Doklady Physics, Vol. 45, No. 12, 2000, pp. 690–693. Translated from Doklady Akademii Nauk, Vol. 375, No. 5, 2000, pp. 627–630.*
*Original Russian Text Copyright © 2000 by Kholostova.*

**MECHANICS**

# A Case of Periodic Motion for a Lagrange Gyroscope with a Vibrating Suspension

**O. V. Kholostova**

Presented by Academician D.M. Klimov March 10, 2000

Received March 28, 2000

## 1. SETTING UP THE PROBLEM

We consider a motion of a Lagrange gyroscope whose suspension fixing point $O$ executes vertical harmonic vibrations according to the law $a_* \cos\Omega t$. Investigation of such a motion necessitates analysis of a reduced system with a single degree of freedom described by the Hamiltonian function [1]

$$H = \frac{1}{2}(p - \varepsilon \sin\tau \sin\theta)^2 + \frac{(a - b\cos\theta)^2}{2\sin^2\theta} + d\cos\theta. \quad (1)$$

Here, the following notation is used: $\theta$ is the angle of the gyroscope-axis deviation from the vertical line (nutation angle) and $p$ is the corresponding (dimensionless) momentum. The quantities $a$ and $b$ are the values of constant cyclic integrals corresponding to cyclic coordinates, i.e., to angles of precession and proper rotation:

$$\tau = \Omega t, \quad \varepsilon = \frac{a_*}{l}, \quad d = \frac{g}{\Omega^2 l},$$

where $l = \dfrac{A}{mz_G}$ is the reduced length of a body considered as a physical pendulum and $z_G = OG$ is the distance between the gyroscope center of mass $G$ and the suspension point. The angular velocities of the precession and proper rotation of the gyroscope are determined by the formulas

$$\psi' = \frac{a - b\cos\theta}{\sin^2\theta}, \quad \varphi' = \frac{A}{C}b - \frac{(a - b\cos\theta)\cos\theta}{\sin^2\theta}. \quad (2)$$

Here, $A$ and $C$ are the equatorial moment of inertia and the moment of inertia about the axis, respectively, and the prime denotes differentiation with respect to $\tau$.

The case $\varepsilon = 0$ corresponds to the classical Lagrange gyroscope with a fixed point [2–4]. If $|a| \neq |b|$, then a single regular precession of the gyroscope corresponds to each pair of values $(a, b)$. For $a = b \neq 0$, a regular precession exists only under the condition $a^2 < 4c$; for $a = -b$, regular precessions of the gyroscope are lacking.

In the case of an oscillating suspension point, we assume the following: (i) the vibration amplitude is small ($\varepsilon \ll 1$); (ii) the eigenfrequency $\sqrt{g/l}$ of small vibrations of the body as a physical pendulum is much lower than the frequency $\Omega$ of oscillations for the point $O$ ($d \ll 1$); and (iii) the angular velocities for both the precession and proper rotation of the gyroscope are small. In addition, we assume that

$$d = \varepsilon^4\gamma, \quad a = \varepsilon^2\alpha, \quad b = \varepsilon^2\beta. \quad (3)$$

We take $\theta = x$ and $p = \varepsilon X$. Then, performing the replacement of variables $x, X \longrightarrow y, Y$, which is $2\pi$-periodic in $\tau$ and close to the identical canonical change, we rearrange Hamiltonian (1) with allowance for relation (3) to a form not involving $\tau$ in terms with an order smaller than or equal to the third order in $\varepsilon$. Next, by means of the canonical change $y, Y \longrightarrow u, v$ specified by the formulas $u = \cos y$, $Y = -v\sin y$, we reduce the Hamiltonian obtained to the algebraic form [1]

$$K = \frac{1}{2}\varepsilon v^2(1 - u^2) + \varepsilon^3\Pi(u) + O(\varepsilon^4), \quad (4)$$

$$\Pi(u) = \frac{1}{4}(1 - u^2) + \gamma u + \frac{(\alpha - \beta u)^2}{2(1 - u^2)}. \quad (5)$$

We now assume that the parameters $\alpha$ and $\beta$ are bound by the relation $|\alpha| = |\beta| \neq 0$. In the present paper, the problem of the existence, number, and stability of the high-frequency (with a period equal to that for oscillations of the suspension point) motions of a gyroscope, which closely resemble regular precessions, is solved. The results are qualitatively different from those found for the classical problem of motion of a gyroscope with a fixed point.

## 2. THE CASE OF $\alpha = \beta$

**Equilibrium positions for an approximate system.** Let $\alpha = \beta$. Omitting the term $O(\varepsilon^4)$ in (4), we

*Moscow Institute of Aviation,*
*Volokolamskoe sh. 4, Moscow, 125080 Russia*

obtain a truncated Hamiltonian to which we put in correspondence an autonomous system of differential equations in the following form:

$$\frac{du}{d\tau} = \varepsilon v(1-u^2), \quad \frac{dv}{d\tau} = \varepsilon u v^2 - \varepsilon^3 \frac{d\Pi}{du}. \qquad (6)$$

Here, the function $\Pi(u)$ defined in (5) is calculated for $\alpha = \beta$.

In the equilibrium positions for system (6), $v = 0$, while $u$ satisfies the equation $\frac{d\Pi}{du} = 0$ or

$$\frac{\alpha^2}{(1+u)^2} = \gamma - \frac{1}{2}u. \qquad (7)$$

In the plane of parameters $(\alpha, \gamma)$ $(\alpha \neq 0, \gamma > 0)$, Fig. 1 shows the domains for which, in the interval $u \in (-1, 1)$, Eq. (7) has either two solutions (regions *2*), a single solution (regions *1*), or no solution (regions *0*). In the same domains, system (6) has two, one, or no equilibrium position, respectively. The boundaries of the domains in Fig. 1 are the parabola $\gamma_1(\alpha) = 0.5 + 0.25\alpha^2$, two segments of the curve $\gamma_2(\alpha) = 0.25[3(2|\alpha|)^{2/3} - 2]$ for $\frac{\sqrt{6}}{9} < |\alpha| < \sqrt{2}$, and segments of the straight line $\gamma = 0$ for $|\alpha| < \frac{\sqrt{6}}{9}$ and the straight line $\alpha = 0$ for $0 < \gamma < 0.5$.

The motion of the gyroscope when its center of mass is above the horizontal plane passing through the suspension point corresponds to the positive roots of Eq. (7), while the motion when the gyroscope center of mass is under that plane corresponds to negative ones. For the parabola $\gamma = \alpha^2$, shown in Fig. 1 by a broken line, Eq. (7) has a zero root. In domains *1*, a single root of Eq. (7) is negative in the subdomains *a* and positive in the subdomains *b*. In domains *2*, two roots of Eq. (7) either have opposite signs (subdomains *c*), are both positive (subdomains *d*), or are both negative (subdomains *e*).

**Gyroscope periodic motions close to regular precessions.** According to the Poincaré theory of periodic motions [5], for reasonably small values of $\varepsilon$, each equilibrium position of approximate system (6) [the points of the boundary curve $\gamma = \gamma_2(\alpha)$ are excluded from consideration] generates a single solution to the system with complete Hamiltonian (4) (for $\alpha = \beta$). This solution is analytical in $\varepsilon$ and $2\pi$-periodic in $\tau$ and has the form

$$u_* = u_0 + O(\varepsilon^4), \quad v_* = O(\varepsilon^4),$$

where $u_0$ is the equilibrium value of $u$ for approximate system (6). The following solution of the system with

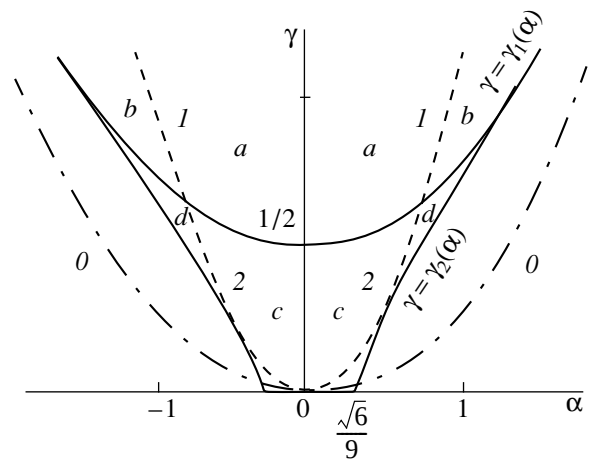


**Fig. 1.** Regions with various numbers of types of motion closely resembling regular precession ($\alpha = \beta$).

Hamiltonian (1), which is $2\pi$-periodic in $\tau$, corresponds to this solution:

$$\theta = \arccos u_0 + \varepsilon^2 \sqrt{1-u_0^2}\cos\tau + O(\varepsilon^4), \qquad (8)$$
$$p = O(\varepsilon^4).$$

Taking into consideration that $\alpha = \beta$, we obtain from (2) and (3) the following expressions for the angular velocities of the precession and proper rotation:

$$\psi' = \frac{\varepsilon^2\alpha}{1+\cos\theta}, \quad \varphi' = \varepsilon^2\alpha\left[\frac{A}{C} - \frac{\cos\theta}{1+\cos\theta}\right]. \qquad (9)$$

Relationships (8) and (9) specify motions for the Lagrange gyroscope with a vibrating suspension point which closely resemble regular precessions. In this case, the tilt angle $\theta$ of the gyroscope axis to the vertical line differs from the constant by a value on the order of $\varepsilon^2$. The angular velocities $\psi'$ and $\varphi'$, being small values on the order of $\varepsilon^2$, differ from the constant by a value on the order of $\varepsilon^4$. These corrections are $2\pi$-periodic in $\tau$. Depending on the values of parameters $\alpha$ and $\gamma$, two (regions *2* in Fig. 1), one (regions *1*), or no (regions *0*) such motions can exist.

The result obtained qualitatively differs from that for the classical problem of the motion of a gyroscope with a fixed point (in the case $a = b$). In the classical problem, a single regular precession exists for the points $(\alpha, \gamma)$ lying above the parabola $\gamma = \alpha^2/4$, shown by the dashed-dotted line in Fig. 1. (In the same region, depending on the values of $\alpha$ and $\gamma$, a single motion, two motions, or no motion close to a regular precession for a gyroscope with a vibrating suspension point can exist.) Regular precessions are absent for points below the parabola indicated (gyroscope motions similar to regular precessions are also missing at the same points).

**Stability of periodic motions.** We consider the issue of stability for motions (8), (9) with respect to the variables $\theta$ and $p$. For this purpose, we should initially solve the problem of stability of the periodic solution $u = u_*$, $v = v_*$ for a system with Hamiltonian (4) (for the case $\alpha = \beta$). Let $u = u_* + x$, $v = v_* + y$. We then expand the Hamiltonian for a perturbed motion as a power series in $x$ and $y$:

$$\Gamma = \Gamma_2 + \Gamma_3 + \Gamma_4 + \ldots, \tag{10}$$

where $\Gamma_k$ is a $k$-power form with respect to $x$ and $y$ and

$$\Gamma_2 = \frac{1}{2}\varepsilon(1 - u_0^2)y^2 + \frac{1}{2}\varepsilon^3\left[f(u_0) - \frac{1}{2}\right]x^2 + O(\varepsilon^4),$$

$$f(u_0) = \frac{2\alpha^2}{(1 + u_0)^3}.$$

If $f(u_0) > \frac{1}{2}$, then the periodic motion under consideration is stable in a linear approximation; if $f(u_0) < \frac{1}{2}$, it is unstable.

Analysis of the function $f(u)$ with relation (7) taken into account shows that, in the case of a single equilibrium position for approximate system (6), the corresponding periodic solution is stable in the linear approximation. In the case of two equilibrium positions, the periodic solution corresponding to the lower equilibrium value of $u$ is stable, whereas the solution corresponding to the higher value of $u$ is unstable in the linear approximation. The latter solution remains unstable in a nonlinear problem as well. This conclusion follows from the Lyapunov theorem on stability in the first approximation [6].

To rigorously resolve the issue of stability for periodic solutions stable in the linear approximation, we perform a nonlinear analysis using the results of the Kolmogorov–Arnol'd–Moser (KAM) theory [7].

With a canonical transformation $x, y \longrightarrow X, Y$ of the Birkhoff-transformation type, Hamiltonian (10) can be reduced to the normal form

$$\Gamma = \frac{1}{2}\omega(X^2 + Y^2) + \frac{1}{4}c(X^2 + Y^2)^2 + O_5. \tag{11}$$

Here, $O_5$ corresponds to a set of terms which is $2\pi$-periodic in $\tau$ and whose powers in $X$ and $Y$ are not lower than fifth one, while the constant coefficients $\omega$ and $c$ have the form

$$\begin{gathered}\omega = \varepsilon^2\sqrt{(1 - u_0^2)\left(-\frac{1}{2} - \frac{df(u_0)}{du_0}\right)} + O(\varepsilon^4),\\ c = -\varepsilon\frac{c_1}{4(1 - u_0)[4\alpha^2 - (1 + u_0)^3]^2} + O(\varepsilon^2),\end{gathered} \tag{12}$$

$$c_1 = 4(7 - u_0)\alpha^4 + 4(1 + u_0)^2(2u_0^2 - 9u_0 + 1)\alpha^2 + (1 + 2u_0^2)(1 + u_0)^5.$$

The quantity $c_1$ is positive for $u_0 \in (-1, 1)$ for an arbitrary value of parameter $\alpha$. Therefore, we have $c < 0$ for reasonably small values of $\varepsilon$. Consequently, $c \neq 0$ and the periodic solution under consideration is stable, which follows from the Arnol'd–Moser theorem [7].

The inferences on the stability of periodic solutions for a system described by Hamiltonian (4) (for $\alpha = \beta$) can be extended to the corresponding motion of the Lagrange gyroscope, which is similar to regular precession. Such a stable motion exists for points $(\alpha, \gamma)$ lying in domains *1* in Fig. 1. For the points $(\alpha, \gamma)$ lying in domains *2*, there exist two such types of motion. One of them is stable, while the other is unstable.

## 3. THE CASE OF $\alpha = -\beta$

Now, let $\alpha = -\beta$. We omit the term $O(\varepsilon^4)$ in Hamiltonian (4). Then we obtain a truncated Hamiltonian to which the approximate system of equations of form (6) corresponds, where the function $\Pi(u)$ defined in (5) is calculated for $\alpha = -\beta$.

The equilibrium positions for this system are given by the equations $v = 0$ and the equation

$$\frac{\alpha^2}{(1 - u)^2} = \frac{1}{2}u - \gamma. \tag{13}$$

In the interval $u_0 \in (-1, 1)$, Eq. (13) has either two solutions [for points $(\alpha, \gamma)$ lying in domains *2* in Fig. 2] or none (domains *0*). The equation for the boundary curve separating domains *0* and *2* has the form $\gamma(\alpha) = 0.25[2 - 3(2|\alpha|)^{2/3}]$ $\left(|\alpha| < \frac{\sqrt{6}}{9}\right)$. Analysis shows that both equilibrium values of $u$ are positive in domains *2*.

The $2\pi$-periodic (in $\tau$) solution to the initial system with Hamiltonian (1) (for $\alpha = -\beta$) corresponds to each equilibrium position of the approximate system; the solution has the form

$$\begin{gathered}\theta = \arccos u_0 + \varepsilon^2\sqrt{1 - u_0^2}\cos\tau + O(\varepsilon^4),\\ p = O(\varepsilon^4).\end{gathered} \tag{14}$$

In this case, the angular velocities for the precession and proper rotation are calculated from the formulas

$$\psi' = \frac{\varepsilon^2\alpha}{1 - \cos\theta}, \quad \varphi' = -\varepsilon^2\alpha\left[\frac{A}{C} + \frac{\cos\theta}{1 - \cos\theta}\right]. \tag{15}$$

Relationships (14) and (15) specify motions for a Lagrange gyroscope with a vibrating suspension point, which are close to regular precessions.

We should particularly emphasize that, whereas regular precessions are absent for a Lagrange gyroscope with a fixed suspension point in the case where $a = -b$,

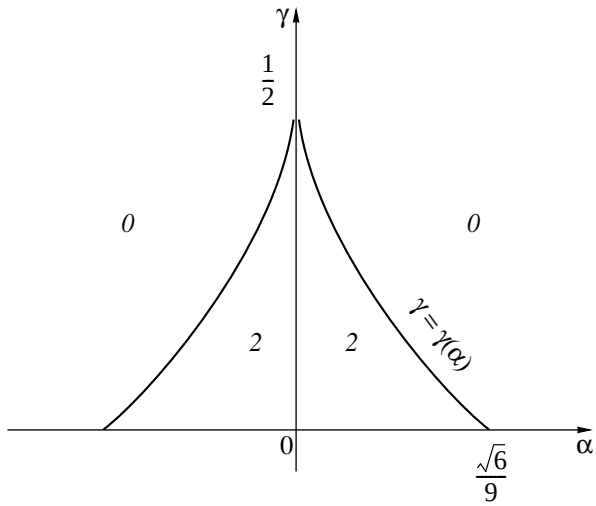


**Fig. 2.** Regions with various numbers of types of motion closely resembling regular precession ($\alpha = -\beta$).

the assumptions made about the nature of a vibration for a suspension point and for gyroscope motion bring about a radically new situation. In this case, a certain domain of variation for the parameters $\alpha$ and $\gamma$ appeared in which there existed two gyroscope motions closely resembling regular precessions.

As was done in Sections 2 and 3, we expand the Hamiltonian for a perturbed motion into a series of form (10), where

$$\Gamma_2 = \frac{1}{2}\varepsilon(1-u_0^2)y^2 + \frac{1}{2}\varepsilon^3\left[g(u_0) - \frac{1}{2}\right]x^2 + O(\varepsilon^4),$$

$$g(u_0) = \frac{2\alpha^2}{(1-u_0)^3}.$$

In the linear approximation when $g(u_0) > \frac{1}{2}$, the periodic solution under consideration is stable, otherwise it is unstable.

With allowance for (13), analysis of the function $g(u)$ shows that the solution corresponding to the lower equilibrium value of $u$ is unstable in the linear approximation, and, consequently, this is also true for the nonlinear problem. As to the solution corresponding to the higher value of $u$, it is stable in the linear approximation. For this solution, using a canonical transformation of the Birkhoff type, namely, $x, y \longrightarrow X, Y$, we can reduce the perturbed Hamiltonian to a normal form similar to (11). Here, the constant coefficients $\omega$ and $c$ are calculated from the formulas

$$\omega = \varepsilon^2\sqrt{(1-u_0^2)\left(\frac{dg(u_0)}{du_0} - \frac{1}{2}\right)} + O(\varepsilon^4),$$
$$c = -\varepsilon\frac{c_2}{4(1+u_0)[4\alpha^2 - (1-u_0)^3]^2} + O(\varepsilon^2). \quad (16)$$

The value of $c_2$ is found from $c_1$ [determined from (12)] by substitution of $u_0$ with $-u_0$. Both $c_1$ and $c_2$ are positive within the interval $u_0 \in (-1, 1)$. Therefore, in the case of reasonably low values of $\varepsilon$, we obtain for the coefficient $c$ in (16), $c < 0$. Consequently, from the Arnol'd–Moser theorem, the periodic motion under consideration is stable.

It follows from the analysis presented here that for two types of Lagrange-gyroscope motion existing in domains *2* (Fig. 2) and closely resembling regular precessions, one is stable while the other is unstable.

## REFERENCES


1. O. V. Kholostova, Prikl. Mat. Mekh. **63**, 786 (1999).
2. N. V. Roze, *Dynamics of the Solid State* (KUBUCh, Leningrad, 1932).
3. R. Grammel, *Der Kreisel, seine Theorie und seine Anwendungen*, Vol. 1: *Die Theorie des Kreisels* (Springer-Verlag, Berlin, 1950; Inostrannaya Literatura, Moscow, 1952).
4. K. Magnus, *Kreisel. Theorie und Anwendungen* (Springer-Verlag, Heidelberg, 1971; Mir, Moscow, 1974).
5. I. G. Malkin, *Some Problems in the Theory of Nonlinear Vibrations* (Gostekhizdat, Moscow, 1956).
6. I. G. Malkin, *Theory of Motion Stability* (Nauka, Moscow, 1966).
7. J. Moser, *Lectures on Hamiltonian Systems* (American Mathematical Society, Providence, 1968; Mir, Moscow, 1973).


*Translated by V. Tsarev*

*Doklady Physics, Vol. 45, No. 12, 2000, pp. 694–696. Translated from Doklady Akademii Nauk, Vol. 375, No. 6, 2000, pp. 767–769.*
*Original Russian Text Copyright © 2000 by Burenin, Kovtanyuk, Polonik.*

**MECHANICS**

# The Possibility of Reiterated Plastic Flow at the Overall Unloading of an Elastoplastic Medium

**A. A. Burenin, L. V. Kovtanyuk, and M. V. Polonik**

Presented by Academician V.P. Myasnikov March 27, 2000

Received April 10, 2000

The process of unloading of deformed materials is usually attributed to the decreasing or removing of external loading forces. However, in the case of nonlinear interrelation between reversible and irreversible strains, there appear such regimes of deformation where a decrease in the applied load can cause reiterated plastic flow. In this paper, we discuss this effect based on a one-dimensional problem concerning the deformation of a thick-wall pipe under pressure applied to its external cylindrical surface.

The problem concerning the accumulation of reversible and irreversible strains in pipe material was considered in [4] within the framework of the model of finite elastoplastic strains proposed in [1–3]. In [4], the plastic flow of a medium near the stress-free internal surface of a pipe was studied as a time-dependent process, whereas the state after unloading was calculated without taking into account its time dependence. This approach stems from assumptions implied in the specific model of finite elastoplastic strains in which the result of deformation does not depend on the character of the unloading path in the stress space. However, this assumption is valid only in the case when a new plastic-flow zone does not arise in the elastoplastic medium upon a decrease in the applied load. If the latter situation is possible, the process of unloading should be considered time-dependent. Hence, we should modify the formulation of the problem in itself compared to [4]. In other words, the model independence of the unloading effect from the features of the process does not ensure that this result can be calculated as that related to the eventual equilibrium state. We should also verify that no reiterated plastic flow took place in the process of unloading. Special features of such modifications in the formulation of the problem are also discussed.

The model of finite elastoplastic strains used here was discussed in detail in [2, 4]; therefore, we analyze only those relationships of the model which we use below. Tensors $e_{ij}$ and $p_{ij}$ of elastic and plastic strains, respectively, are determined by the following transport equations [4, 5]:

$$\frac{dp_{ij}}{dt} = \varepsilon_{ij}^p - \varepsilon_{ik}^p p_{kj} - p_{ik}\varepsilon_{kj}^p + r_{ik}p_{kj} - p_{ik}r_{kj},$$

$$\frac{de_{ij}}{dt} = \varepsilon_{ij} - \varepsilon_{ij}^p - \frac{1}{2}(e_{ik}\upsilon_{k,j} + \upsilon_{k,i}e_{kj} - r_{ik}e_{kj} + e_{ik}r_{kj} - \varepsilon_{ik}^p e_{kj} + e_{ik}\varepsilon_{kj}^p). \quad (1)$$

Here, $\varepsilon_{ij}$ is the Euler strain-rate tensor, $\varepsilon_{ij}^p$ is the strain-rate tensor for irreversible strains, $\upsilon_{i,j}$ is the velocity-gradient tensor for the points of a moving medium, and $r_{ij} = 0.5(\upsilon_{i,j} - \upsilon_{j,i}) + \Phi(\varepsilon_{ij}, e_{ij})$ is the skew-symmetric tensor calculated in [3, 4]. Using definitions (1) for elastic and plastic strains, the separation of the Almansi total strains $d_{ij}$ into reversible component $e_{ij}$ and irreversible component $p_{ij}$ is performed by the relationship

$$d_{ij} = e_{ij} + p_{ij} - 0.5e_{ik}e_{kj} - e_{ik}p_{kj} - p_{ik}e_{kj} + e_{ik}p_{ks}e_{sj}. \quad (2)$$

We assume that the deformation process is isothermal and that the plastic flow is ideal. We also assume the hypothesis to the effect that the free energy is independent of plastic strains holds true. In this case, the energy conservation law provides an opportunity to calculate the stresses in the deformed body based on the known strains in this body for the given dependence $F = F(e_{ij})$ of free energy on irreversible strains. In our calculations, we used the following relationships for $F(d_{ij})$ in the case of an incompressible medium:

$$F(d_{ij}) = \rho_0^{-1}W(L_1, L_2),$$
$$W = (a - \mu)L_1 + aL_2 + bL_1^2 - \chi L_1L_2 - \theta L_1^3, \quad (3)$$
$$L_1 = d_{ii}, \quad L_2 = d_{ij}d_{ji}.$$

If there are irreversible strains in the medium, then we have $W = W(e_{ij})$ and, instead of invariants of the

*Institute of Automatics and Control Processes, Far East Division, Russian Academy of Sciences, pr. Stoletiya Vladivostoka 159, Vladivostok, 690022 Russia*

Almansi tensor in (3), we should assume that

$$I_1 = e_{ii} - 0.5e_{ij}e_{ji},$$
$$I_2 = e_{ij}e_{ji} - e_{is}e_{sj}e_{ji} + 0.25e_{is}e_{sk}e_{kj}e_{ji}$$

for the same values of elastic constants $\mu$, $a$, $b$, $\chi$, and $\theta$. The choice of invariants $I_1$ and $I_2$ of the elastic-strain tensor $e_{ij}$ ensures that we can pass to $L_1$ and $L_2$ in the limit of plastic strains tending to zero.

We assume that the thick-wall pipe whose boundary surfaces in the free state is described in the cylindrical coordinate system by the equations $r = r_0$ and $r = R_0$ ($R_0 > r_0$) is loaded by a pressure applied to its outer surface $\sigma_{rr}|_{r = R(t)} = -P(t)$ and that its internal surface $r = s(t)$ remains free of stresses. When the pressure $P(t)$ increases up to a certain value $P_0$, reversible deformation takes place. At this pressure, the stressed state corresponds to the plasticity condition $\sigma_{rr} - \sigma_{\theta\theta} = 2k$ at the internal surface $r = s_0$ of the pipe. From this time moment, an irreversible deformation starts from the surface $r = s_0$ so that, at subsequent moments of time $t$, the plastic-flow zone is situated in the layer for which $s(t) \le r \le r_1(t)$, where $s(t)$ is the current position of the internal surface of the pipe and $r_1(t)$ is the position of the moving boundary of the plastic region. The accepted condition of incompressibility of the medium determines its kinematics with an accuracy to a certain function of time $\varphi(t)$:

$$u_r = u = r - (r^2 + \varphi(t))^{1/2},$$
$$d_{rr} = 0.5\varphi(t)(r^2 + \varphi(t))^{-1}, \quad d_{\theta\theta} = -0.5\varphi(t)r^{-2}, \quad (4)$$
$$\varphi(t) = R_0^2 - R^2(t) = r_0^2 - s^2(t).$$

In (4), $u_r = u$ is the nonzero component of translations and $d_{rr}$ and $d_{\theta\theta}$ are the nonzero components of the Almansi tensor. Using the given function $P(t)$, function $\varphi(t)$ can be found by solving an ordinary differential equation, which is the result of integrating equations of motion separately in the zones of reversible and irreversible deformation. We use the boundary conditions discussed above. The following values of parameters can be taken as initial conditions for such an equation: $\varphi'(0) = 0$ and $\varphi(0) = r_0^2 - s_0^2$. If a final value $P(t_1) = P_1$ of the applied pressure remains unchanged, then the medium appears to be in the equilibrium state. In Fig. 1, we show the characteristic plots illustrating the distributions of dimensionless (normalized to $\mu$) stresses in the body. Everywhere within the range between $\xi_{s_1} = s_1 R_0^{-1}$ and $\xi_{r_1} = r_1 R_0^{-1}$, the difference between dimensionless pressures $\sigma_{rr}$ (solid line) and $\sigma_{\theta\theta}$ (dashed line) is constant and equal to $2k\mu^{-1} = 0.006$.

We now unload the body by lowering the applied pressure to a certain value $P_* \le P_1$. If $P_1 \le P_1^*$, the value of $P_*$ can be zero and the unloaded state can be calculated as an equilibrium state at zero external forces but with accumulated irreversible strains [4]. In this way, we calculate the residual stresses and strains. However, at $P_1 > P_1^*$, i.e., when $r_1 \gg s_1$ as in the case shown in Fig. 1, $\xi_{r_1} \gg \xi_{s_1}$. In other words, when a significant level of irreversible strains is accumulated in the body, $P_*$ cannot attain the zero value. In fact, for a certain value $P_* = P_2 < P_1$, the stressed state at the internal surface comes again to the surface of loading but with the opposite sign: $\sigma_{rr} - \sigma_{\theta\theta} = -2k$. Such a distribution of stresses is shown in Fig. 2, where $\xi_{s_k}$ and $\xi_{r_p}$ correspond to the positions of the internal surface of the pipe and the plastic-zone boundary ($\xi_{r_p} \ne \xi_{r_1}$ owing to the difference between the material and spatial coordinates). Whereas $\sigma_{rr}$ at the internal surface of the pipe remains zero with decreasing external pressure, $\sigma_{\theta\theta}$ becomes positive with decreasing $P_*$.

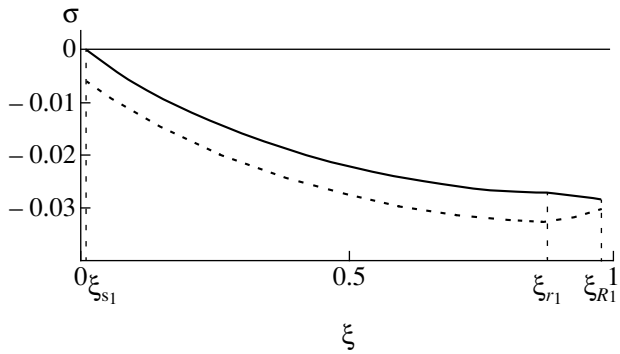


**Fig. 1.** Stresses at the onset of the unloading process.

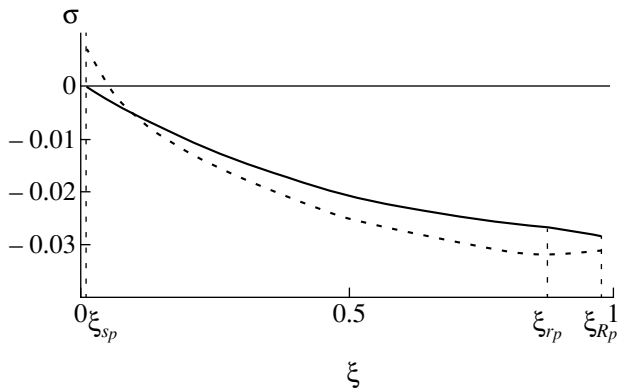


**Fig. 2.** Stresses at the onset of the reiterated plastic flow.

In the case of a further decrease in the external pressure, the process of plastic flow of material begins and, consequently, it is necessary to modify the formulation of the boundary value problem. Now, it is necessary to integrate not the equilibrium equations, but the equation of motion in the three zones $\xi_{s_k} < \xi < \xi_{r_2}$, $\xi_{r_2} < \xi <$

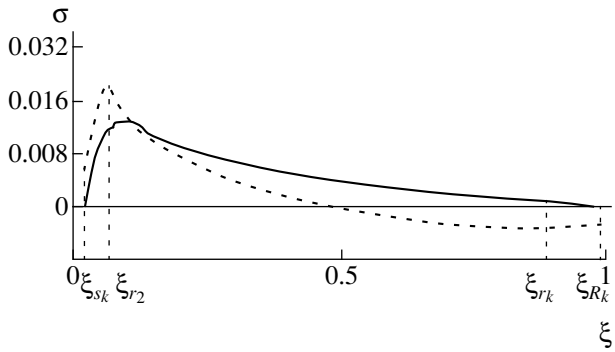


**Fig. 3.** Residual stresses after complete unloading of the body.

$\xi_{r_k}$, and $\xi_{r_k} < \xi < \xi_{R_k}$ (Fig. 3) using the boundary conditions and the continuity conditions for stresses at the boundaries of the zones. In this case, it is necessary to take into account that for $\xi < \xi_{r_2}$, the reversible strains remain the same, whereas for $\xi_{r_2} < \xi < \xi_{r_k}$, the irreversible strains are constant. The values $\xi = \xi_{r_2}$ are determined by the position of the boundary of the region of the plastic flow. In Fig. 3, we show the distributions of the residual stresses, i.e., the final values of parameters $\xi_{s_k}$, $\xi_{r_2}$, $\xi_{r_k}$, and $\xi_{R_k}$ and of dimensionless stresses $\sigma_{rr}$ and $\sigma_{\theta\theta}$ at zero applied pressure. Everywhere in the $\xi_{s_k} < \xi < \xi_{r_2}$ range, the difference between stresses $\sigma_{rr}$ and $\sigma_{\theta\theta}$ remains equal to $-2k$.

## ACKNOWLEDGMENTS

This work was supported by the Russian Foundation for Basic Research, project no. 99-01-00644.

## REFERENCES

1. G. I. Bykovtsev and A. V. Shitikov, Dokl. Akad. Nauk SSSR **311**, 59 (1990) [Sov. Phys. Dokl. **35**, 297 (1990)].
2. A. A. Burenin and L. V. Kovtanyuk, *An Example of an Incompressible Elastoplastic Body Model Undergoing Large Deformations*, in Problems of Natural Science and Industry (Dal'nevost. Gos. Tekh. Univ., Vladivostok, 1995).
3. A. A. Burenin, G. I. Bykovtsev, and L. V. Kovtanyuk, Dokl. Akad. Nauk **347**, 199 (1996) [Phys.–Dokl. **41**, 127 (1996)].
4. L. V. Kovtanyuk and M. B. Polonik, *Lamé Problem on the Equilibrium of a Thick-Walled Pipe Made of Incompressible Elastoplastic Material. Problems of Mechanics of Continuous Media and Construction Elements*, in Problems of Continuum Mechanics and Structural-Element Mechanics (Vladivostok, 1998), pp. 77–96.
5. V. P. Myasnikov, Vestn. Dal'nevost. Otd. Ross. Akad. Nauk, No. 4, 8 (1996).

*Translated by V. Bukhanov*

*Doklady Physics, Vol. 45, No. 12, 2000, pp. 697–700. Translated from Doklady Akademii Nauk, Vol. 375, No. 6, 2000, pp. 770–773.*
*Original Russian Text Copyright © 2000 by Gertsenshteĭn, Zhilenko, Krivonosova.*

**MECHANICS**

# An Attempt at Generalizing Scenarios for a Transition to Turbulence in the Spherical Couette Flow: The Case of Oppositely Rotating Spherical Boundaries

**S. Ya. Gertsenshteĭn, D. Yu. Zhilenko, and O. É. Krivonosova**

Presented by Academician G.G. Chernyĭ March 24, 2000

Received April 18, 2000

We report the results of an experimental study on the laminar-to-turbulent transition in the spherical Couette flow, i.e., in a viscous incompressible flow between two spherical boundaries rotating about the same vertical axis. The experiments are carried out in a thick spherical layer with a relative thickness $\delta = \frac{r_2 - r_1}{r_1} = 1.006$ for oppositely rotating spherical boundaries ($\mathrm{Re}_2 < 0$). The Reynolds numbers vary within the ranges $-950 < \mathrm{Re}_2 < -700$ and $250 < \mathrm{Re}_1 < 450$. Here, $\mathrm{Re}_i = \frac{\Omega_i r_i^2}{\nu}$, $\nu$ is the kinematic viscosity of the fluid in the layer under consideration, and $r_i$ and $\Omega_i$ are the radii and angular velocities of the spherical boundaries labeled by the indices 1 (inner) or 2 (outer).

Previously, the transition of the spherical Couette flow formed in a thick layer to stochastic behavior was investigated both for rotation of only the inner boundary ($\mathrm{Re}_2 = 0$) [1] and for the oppositely rotating spherical boundaries ($\mathrm{Re}_2 = -700$) [2]. In particular, it was shown that, in the case of quasi-static variation of $\mathrm{Re}_1$, the flow can become stochastic after passing through six (in the first case) or four (in the second case) bifurcation points. For a wider range of determining parameters (in the case of the spherical Couette flow, they are represented by $\mathrm{Re}_1$, $\mathrm{Re}_2$, and the relative thickness of the layer), the problem of classification of the transition scenarios remained open.

Experimental studies of the transition to stochastic behavior were carried out by using the Shar setup [1]. A laser Doppler anemometer was used for measuring the velocity pulsations at a layer point situated at a distance of 120 mm from the rotation axis of the spheres. The distance to the equator varied from 45 to 75 mm. We could maintain all parameters of the setup at a constant level, so that deviations of both the Reynolds numbers and the layer temperature from their nominal values did not exceed 0.05%. Spectra of velocity pulsations were calculated by the fast Fourier-transform method for discrete analog-signal samples consisting of 16384 and 32768 points separated by 0.06-s intervals, which were obtained with the help of a laser Doppler anemometer. All flow regimes presented here correspond to constant $\mathrm{Re}_2$ and quasi-static variation of $\mathrm{Re}_1$.

The primary flow formed in the spherical layer is symmetric with respect to both the equator and the rotation axis. It represents the superposition of the azimuth axial rotation and meridional circulation, the amplitude and shape of the latter being dependent on the relation between $\mathrm{Re}_1$ and $\mathrm{Re}_2$ [3]. For example, in the case of oppositely rotating spherical boundaries, the appearance of a flow with a two-vortex meridional circulation formed by oppositely rotating vortices is possible [3]. Then, a line separating flow regions with different directions of meridional circulation is observed in the meridian plane.

The segment *abc* for the stability boundary corresponding to the primary flow in a spherical layer of thickness $\delta = 1.006$ (see [4]) in the region $-1100 < \mathrm{Re}_2 < -510$ is shown in Fig. 1a. This boundary has a local maximum at the point *b*. In the region *a–b* corresponding to the stability threshold, the line separating meridional circulations of the primary flow is shifted in the equatorial region to the inner spherical boundary. In addition, the loss of stability is accompanied by the formation of a circumpolar secondary spiral flow spreading from the pole towards the equator. Pattern *P* in Fig. 1a shows, in the meridian plane (above the equator), a separation line of meridional circulations of the primary flow and (below the equator) a section of the secondary flow by this plane [4]. Under the conditions corresponding to the segment *b–c* of the stability threshold, the line separating the meridional circulations of the primary flow is remote along its entire length from both spherical boundaries. The secondary

*Institute of Mechanics, Moscow State University, Michurinskiĭ pr. 1, Moscow, 117234 Russia*

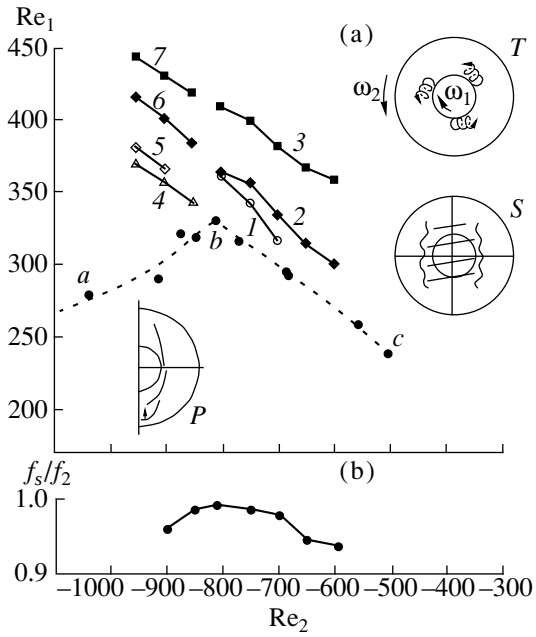


**Fig. 1.** (a) Thresholds for the onset of the supercritical-flow regimes and schematic patterns of their spatial structures; (b) relative frequency for the helicons regime.

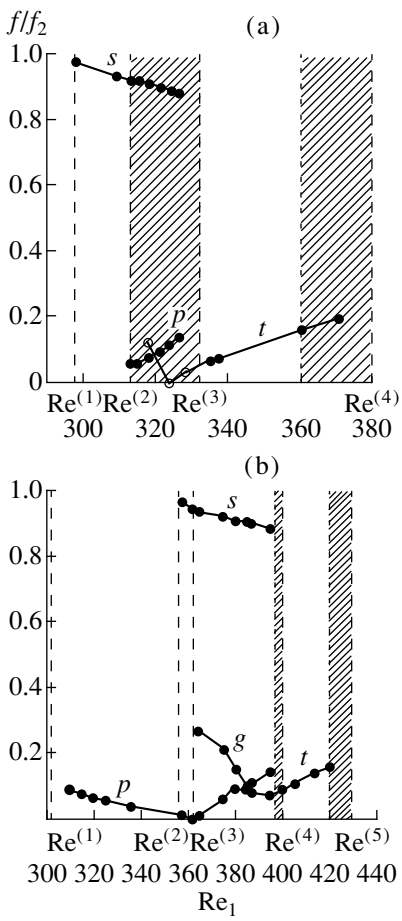


**Fig. 2.** Relative frequencies of the supercritical flow regimes as a function of $Re_1$ at (a) $Re_2 = -700$ and (b) $Re_2 = -900$. Black and white symbols correspond to the increasing and decreasing values of $Re_1$, respectively.

flow arising under such conditions is asymmetric with respect to both the equator and the rotation axis. It represents a system of helicons (shown schematically in the pattern *S* of Fig. 1a) which are equidistant from each other, inclined with respect to the equatorial plane, and propagate both along the rotation axis and in the direction of the rotation of the inner sphere. Being observed visually, this secondary flow manifests itself in the meridian plane as periodic oscillations propagating along the line that separates the meridional circulations. Similar secondary-flow structures were observed previously in thin layers [3]. Thus, neutral curves corresponding to different instability types intersect each other at the point *b*. For the Couette flow caused by oppositely rotating cylindrical boundaries, a similar region near the point of intersection of neutral curves was studied theoretically in [5].

For any $Re_2$ within the range $-810 < Re_2 < -700$, a quasi-static increase in $Re_1$ results in the same sequence of supercritical flow regimes. Each of them is characterized by its own spatial structure and a frequency set in the spectrum of velocity pulsations. In this sense, for the $Re_2$ range under consideration, the scenario of transition to chaos by passing through four bifurcation points, which was investigated in [2] at $Re_2 = -700$, is universal. For each supercritical flow regime, Fig. 2a shows the dependence of relative frequencies (normalized to the rotation frequency of the outer spherical boundary $f_2$) belonging to the velocity-pulsation spectrum on $Re_1$. The first bifurcation (at $Re^{(1)}$) represents the stability loss characterized by the appearance of helicons with a single frequency $f_s$ in the spectrum (Fig. 2a, curve *s*). The second bifurcation (at $Re^{(2)}$) characterizes the onset of a quasi-periodic regime in which circumpolar motion having frequency $f_p$ (Fig. 2a, curve *p*) arises along with the helicons. The third bifurcation (at $Re^{(3)}$) leads to a new flow regime characterized by single frequency $f_t$ (Fig. 2a, curve *t*) and is conventionally called the regime of localized vortices. In this regime, the flow resembling the open Taylor rings forms from both sides of the equator. It represents three vortices which are inclined with respect to the equatorial plane in the azimuth-equidistant opening regions and propagate, as an entire structure, along the azimuth circle. The top view of this flow regime is shown in the pattern *T* of Fig. 1a. The fourth bifurcation (corresponding to $Re^{(4)}$) leads to the chaotic flow regime. In contrast to the first two regimes, the localized-vortex and chaotic regimes are of hard excitation. (The corresponding hysteresis zones are shaded in Fig. 2a.)

Figure 1a, curves *1–3*, shows the boundaries of onset for the (*1*) quasi-periodic, (*2*) localized-vortex, and (*3*) stochastic flow regimes at $-810 < Re_2 < -700$.

Furthermore, we consider the transition from the laminar flow regime to the stochastic flow regime under the conditions conforming to the segment *a–b* of the stability-threshold line.

Figure 2b presents the relative frequencies as functions of $Re_1$ at $Re_2 = -900$. The first bifurcation (at $Re^{(1)}$) represents the stability loss characterized by the appearance of circumpolar motion with a single frequency $f_p$ in the spectrum. The second bifurcation (at $Re^{(2)}$) is accompanied by the origination of helicons on the surface separating the meridional circulations. Then, the quasi-periodic flow regime forms and the frequency $f_s$ arises in the spectrum along with $f_p$. An increase in $Re_1$ is accompanied by a decrease in the first frequency $f_p$ to zero. In this case, the spatial flow structure in the circumpolar region becomes steady. Furthermore, the circumpolar waves reverse their direction of propagation and the frequency $f_p$ starts to grow. At $Re^{(3)}$, the third frequency $f_g$ arises in the spectrum (the third bifurcation), such that the amplitude of this spectral line exceeds those of the lines with frequencies $f_s$ and $f_p$. As $Re_1$ increases, the amplitude of the circumpolar motion grows and becomes higher than that of the helicons but lower than the amplitude of the spectral line at frequency $f_g$. At $Re^{(4)}$, the fourth bifurcation occurs. It is followed by the formation of the regime of localized vortices with a single frequency $f_t$ in the spectrum. We note that the frequency $f_g$ before bifurcation and the frequency $f_t$ after bifurcation are very close to each other. This allows us to assume that the onset for the regime of local vortices occurs at the frequency $f_g$. The regime of local vortices, in turn, is changed by the stochastic regime at $Re^{(5)}$ (the fifth bifurcation).

Figure 1a shows curves for the onset of the above-described quasi-periodic (curve *4*), three-frequency (curve *5*), local-vortex (curve *6*), and stochastic flow (curve *7*) regimes for the left (with respect to the local maximum) segment of the stability threshold. Curve *4* corresponds to the onset of the quasi-periodic regime and continues the segment *b–c* of the stability-threshold line. Moreover, the relative frequency $f_s/f_2$, describing the helicons associated with curve *4*, varies without discontinuities compared to the corresponding values in the segment *b–c* (Fig. 1b). Due to this fact, we have attempted to find a unified description of the scenarios for transition to the left and to the right from the local maximum.

It turns out that, at any $Re_2$, the relative frequencies of the supercritical flow regimes depend only on the ratio $Re_1/Re_{1s}$ (Fig. 3), where $Re_{1s}$ corresponds to the threshold of helicon formation (Fig. 1a, curves *4* and *b–c*).

All *s* curves (Fig. 3), which describe the helicons, originate at the point $Re_1/Re_{1s} = 1$ and virtually represent a single curve. The difference lies in the fact that at

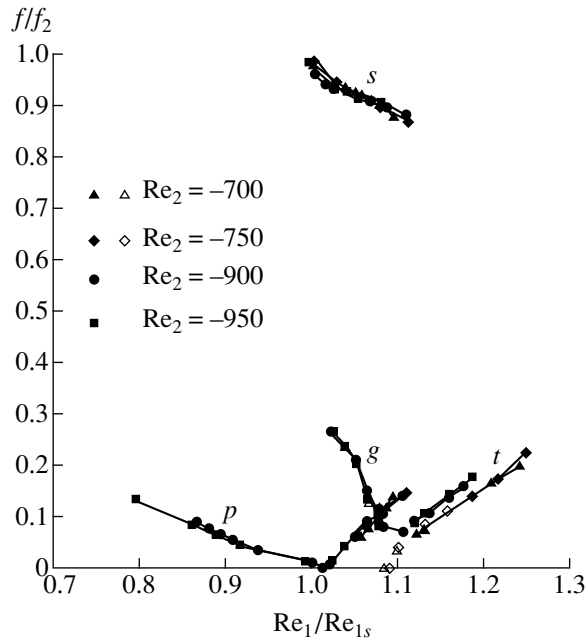


**Fig. 3.** Unified dependence of the relative frequencies for supercritical flow regimes on the ratio $Re_1/Re_{1s}$ at different values of $Re_2$. Black and white symbols correspond to increasing and decreasing $Re_1$, respectively.

$Re_2 > -810$, this regime is secondary, i.e., arising at the stability threshold, whereas at $Re_2 < -810$, it is combined with the already existing circumpolar motion. Curves *p*, which describe the circumpolar motion, also represent the unified dependence for all analyzed values of $Re_2$. The difference lies in the moment of the appearance of values of the circumpolar motion dependent on the ratio $Re_1/Re_{1s}$. The onset of the circumpolar motion occurs always for $Re_2 < -810$ at $Re_1/Re_{1s} < 1$ and for $Re_2 > -810$ at $Re_1/Re_{1s} > 1$, i.e., always in the ascending branch of the function $f_p/f_2$. It is noteworthy that the frequency $f_g/f_2$, existing only at $Re_2 < -900$, is close to $f_t/f_2$ in the hysteresis region of the localized-vortex regime corresponding to the segment *b–c* (Fig. 3, white symbols).

Thus in the region of the determining parameters under investigation, the laminar-to-turbulent transition occurs in accordance with scenarios that, with the use of the specially chosen coordinates, are of a unified description. In the analyzed range of the parameters $Re_1$ and $Re_2$, both to the left and to the right from the local maximum of the stability curve, all frequency characteristics of the supercritical flow regimes are formed by combinations of the frequencies that correspond to the following three spatial flow structures: the helicons, the circumpolar motion, and the localized-vortex regime. The transition to stochastic behavior always occurs from the single-frequency localized-vortex regime with a structure symmetric with respect to

the equatorial plane. At the same time, all bifurcation points preceding this regime arise according to the Ruelle–Takens scenario [6].

## REFERENCES


1. Yu. N. Belyaev and I. M. Yavorskaya, in *Nonlinear Dynamics and Turbulence*, Ed. by G. I. Barenblatt, G. Iooss, and D. D. Joseph (Pitman Advanced Publ. Program, Boston, 1983), pp. 61–70.
2. S. Ya. Gertsenshteĭn, D. Yu. Zhilenko, and O. É. Krivonosova, Dokl. Akad. Nauk **369**, 337 (1999) [Dokl. Phys. **44**, 775 (1999)].
3. Yu. N. Belyaev and I. M. Yavorskaya, Itogi Nauki Tekh., Ser. Mekh. Zhidk. Gaza **15**, 3 (1980).
4. S. Ya. Gertsenshteĭn, D. Yu. Zhilenko, O. É. Krivonosova, and A. A. Monakhov, Izv. Akad. Nauk, Mekh. Zhidk. Gaza, No. 4, 54 (1999).
5. V. V. Kolesov and V. I. Yudovich, Izv. Akad. Nauk, Mekh. Zhidk. Gaza, No. 4, 81 (1998).
6. D. Ruelle and F. Takens, Commun. Math. Phys. **20**, 167 (1971).


*Translated by Yu. Verevochkin*

*Doklady Physics, Vol. 45, No. 12, 2000, pp. 701–704. Translated from Doklady Akademii Nauk, Vol. 375, No. 6, 2000, pp. 774–777.*
*Original Russian Text Copyright © 2000 by Obraztsov, Barynin, Khanin.*

**MECHANICS**

# A Mechanism for Restriction of the Activation-Zone Propagation for a Hemostasis System (A Mathematical Model)

**Academician I. F. Obraztsov, Yu. A. Barynin, and M. A. Khanin**

Received September 9, 1999

## INTRODUCTION

Using methods of mathematical simulation, a hemostasis system was found to be bistable [1–4]. Later on, the concept of bistability and the existence of threshold effects in the external-path activation were supported by the results of biochemical studies. As is well known, the bistability of the hemostasis system protects against the formation of inadequate thrombosis. On the other hand, this feature suggests the possibility that there exists an autowave mechanism for the propagation of an activation zone of a hemostasis system. It was hypothesized in [5] that activation-zone propagation is terminated owing to the propagation of an autowave of a certain inhibitor that catches up to the activation wave. However, no inhibitor satisfying the necessary requirements is known. The goal of the present study is to investigate the mechanism for the processes terminating the propagation of the activation-zone for a hemostasis system using a mathematical-simulation method. The same mechanisms must also insure that the thrombus size is adequate relative to the extent of blood-vessel damage.

## BASIC PROCESSES FOR CONSTRUCTING A MATHEMATICAL MODEL

We consider only the external path of the hemocoagulation schematically shown in Fig. 1. As is seen from this figure, the external path is composed of the following components:

(*1*) cascade of fermentative reactions;

(*2*) positive feedback caused by the action of a cofactor, i.e., the factor *Va*;

(*3*) positive feedback appearing in the mutual activation of factors *VII* and *X*;

(*4*) negative feedback caused by the action of the C protein.

In the mathematical model proposed, the following processes are represented:

(i) fermentative reactions resulting in the activation of coagulation factors;

(ii) chemical reactions of the second order resulting in the formation of activated-factor complexes;

(iii) diffusion of proenzymes, procofactors, enzymes, cofactors, as well as complexes of activated factors and cofactors;

(iv) activation of the external path by the tissue factor;

(v) distinction between the rate of fermentative reactions on thrombocyte membranes and that in the blood bulk;

(vi) transfer of the coagulation factors by the blood flow.

## MATHEMATICAL MODEL FOR PROPAGATING THE ACTIVATION ZONE

With the structure of the external path and the processes under consideration taken into account, the mathematical model being developed takes the following form.

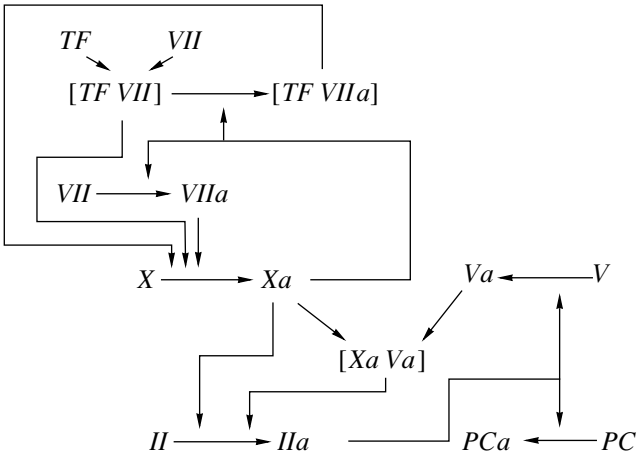


**Fig. 1.** Diagram for the hemocoagulation external path.

*Moscow Institute of Aviation and Technology (MATI), ul. Orshanskaya 3, Moscow, 121552 Russia*

1028-3358/00/4512-0701$20.00 © 2000 MAIK “Nauka/Interperiodica”

**The process proceeding on cell membranes:**

$$\frac{\partial[TF]}{\partial t} = -\frac{\partial[TFVII]}{\partial t} - \frac{\partial[TFVIIa]}{\partial t},$$

$$\frac{\partial[TFVII]}{\partial t} = k_{tf_7}[TF][VII] - E_{tf\,7}[TFVII] - k_{tf\,7_10a}\frac{[TFVII][Xa]}{k_{mtf\,7_10a} + [TFVII]},$$

$$\frac{\partial[TFVIIa]}{\partial t} = k_{tf\,7_10a}\frac{[TFVII][Xa]}{k_{mtf\,7_10a} + [TFVII]} - E_{TF7a}[TFVIIa],$$

$$\frac{\partial[VII]}{\partial t} = -\alpha k_{7_10a}\frac{[VII][Xa]}{k_{m7_10a} + [VII]} - k_{tf_\mathrm{VII}}[TF][VII] + E_{tf\,7}[TFVII] + \frac{D_7}{\delta}\frac{\partial[VII]}{\partial x}\bigg|_{x=0},$$

$$\frac{\partial[VIIa]}{\partial t} = \alpha k_{7_10a}\frac{[VII][Xa]}{k_{m7_10a} + [VII]} + E_{tf\,7a}[TFVIIa] + \frac{D_{7a}}{\delta}\frac{\partial[VIIa]}{\partial x}\bigg|_{x=0},$$

$$\frac{\partial[Xa]}{\partial t} = \alpha k_{10_7a}\frac{[X][VIIa]}{k_{m10_7a} + [X]} + k_{10_TFVII}\frac{[X][TFVII]}{k_{m10_TFVII} + [X]} + k_{10_TFVIIa}\frac{[X][TFVIIa]}{k_{m10_TFVIIa} + [X]} - k_{10a_5a}[Xa][Va] + \frac{D_{10a}}{\delta}\frac{\partial[Xa]}{\partial x}\bigg|_{x=0},$$

$$\frac{\partial[V]}{\partial t} = -\alpha k_{5_2a}\frac{[V][IIa]}{k_{m5_2a} + [V]} - \alpha k_{5_10a}\frac{[V][Xa]}{k_{m5_10a} + [V]} + \frac{D_5}{\delta}\frac{\partial[V]}{\partial x}\bigg|_{x=0}, \tag{1}$$

$$\frac{\partial[Va]}{\partial t} = \alpha k_{5_2a}\frac{[V][IIa]}{k_{m5_2a} + [V]} + \alpha k_{5_10a}\frac{[V][Xa]}{k_{m5_10a} + [V]} - k_{10a_5a}[Xa][Va] + \frac{D_{5a}}{\delta}\frac{\partial[Va]}{\partial x}\bigg|_{x=0},$$

$$\frac{\partial[XaVa]}{\partial t} = k_{10a_5a}[Xa][Va] + \frac{D_{10a5a}}{\delta}\frac{\partial[XaVa]}{\partial x}\bigg|_{x=0},$$

$$\frac{\partial[II]}{\partial t} = -\alpha k_{2_10a5a}\frac{[II][XaVa]}{k_{m2_10a5a} + [II]} - \alpha k_{2_10a}\frac{[II][Xa]}{k_{m2_10a} + [II]} + \frac{D_2}{\delta}\frac{\partial[II]}{\partial x}\bigg|_{x=0},$$

$$\frac{\partial[IIa]}{\partial t} = \alpha k_{2_10a5a}\frac{[II][XaVa]}{k_{m2_10a5a} + [II]} + \alpha k_{2_10a}\frac{[II][Xa]}{k_{m2_10a} + [II]} + \frac{D_{2a}}{\delta}\frac{\partial[IIa]}{\partial x}\bigg|_{x=0},$$

$$\frac{\partial[PC]}{\partial t} = -k^*_{PC_2a}\frac{[PC][IIa]}{k_{mPC_2a} + [PC]} + \frac{D_{PC}}{\delta}\frac{\partial[PC]}{\partial x}\bigg|_{x=0},$$

$$\frac{\partial[PCa]}{\partial t} = k^*_{PC_2a}\frac{[PC][IIa]}{k_{mPC_2a} + [PC]} + \frac{D_{PCa}}{\delta}\frac{\partial[PCa]}{\partial x}\bigg|_{x=0}.$$

Here, $[i]$ and $D_i$ are the $i$-factor concentration and diffusivity, respectively; $k_{i,\,ma}$ is the constant for the rate of activation of the $i$-factor by the $m$th-ferment; $k_{mi,\,ma}$ is the Michaelis constant in the fermentative activation reaction for the $i$-factor by the $m$th-ferment; $\delta$ is the thickness of the near-membrane layer; and $E_i$ is the constant of the $i$-factor inactivation.

**The process proceeding in a blood bulk:**

$$\frac{\partial[VII]}{\partial t} = -k_{7_10a}\frac{[VII][Xa]}{k_{m7_10a} + [VII]} + H\frac{x}{L}\left(2 - \frac{x}{L}\right)\frac{(VIIo - [VII])}{L_y} + D_7\frac{\partial^2[VII]}{\partial x^2},$$

$$\frac{\partial[VIIa]}{\partial t} = k_{7_10a}\frac{[VII][Xa]}{k_{m7_10a} + [VII]} - H\frac{x}{L}\left(2 - \frac{x}{L}\right)\frac{[VIIa]}{L_y} + D_{7a}\frac{\partial^2[VIIa]}{\partial x^2},$$

$$\frac{\partial[X]}{\partial t} = -k_{10_7a}\frac{[X][VIIa]}{k_{m10_7a} + [X]} + H\frac{x}{L}\left(2 - \frac{x}{L}\right)\frac{(Xo - [X])}{L_y} + D_{10}\frac{\partial^2[X]}{\partial x^2}, \tag{2}$$

$$\frac{\partial[Xa]}{\partial t} = k_{10_7a}\frac{[XVIIa]}{k_{m10_7a} + [X]} - E_{10_ATIII}[Xa] + k_{10a5a_PCa}\frac{[XaVa][PCa]}{k_{m10a5a_PCa} + [PCa]} - k_{10a_5a}[Xa][Va] - H\frac{x}{L}\left(2 - \frac{x}{L}\right)\frac{[Xa]}{L_y} + D_{10a}\frac{\partial^2[Xa]}{\partial x^2},$$

$$\frac{\partial[V]}{\partial t} = -k_{5_2a}\frac{[V][IIa]}{k_{m5_2a}+[V]} - k_{5_10a}\frac{[V][Xa]}{k_{m5_10a}+[V]} + H\frac{x}{L}\left(2-\frac{x}{L}\right)\frac{(Vo-[V])}{L_y} + D_5\frac{\partial^2[V]}{\partial x^2},$$

$$\frac{\partial[Va]}{\partial t} = k_{5_2a}\frac{[V][IIa]}{k_{m5_2a}+[V]} + k_{5_10a}\frac{[V][Xa]}{k_{m5_10a}+[V]} + E_{10a5a_ATIII}[XaVa] - k_{5a_PCa}\frac{[Va][PCa]}{k_{m5a_PCa}+[Va]} - k_{10a_5a}[Xa][Va] - H\frac{x}{L}\left(2-\frac{x}{L}\right)\frac{[Va]}{L_y} + D_{5a}\frac{\partial^2[Va]}{\partial x^2},$$

$$\frac{\partial[XaVa]}{\partial t} = k_{10a_5a}[Xa][Va] - E_{10a5a_ATIII}[XaVa] - k_{10a5a_PCa}\frac{[XaVa][PCa]}{k_{m10a5a_PCa}+[XaVa]} - H\frac{x}{L}\left(2-\frac{x}{L}\right)\frac{[XaVa]}{L_y} + D_{10a5a}\frac{\partial^2[XaVa]}{\partial x^2},$$

$$\frac{\partial[II]}{\partial t} = -k_{2_10a5a}\frac{[II][XaVa]}{k_{m2_10a5a}+[II]} - k_{2_10a}\frac{[II][Xa]}{k_{m2_10a}+[II]} + H\frac{x}{L}\left(2-\frac{x}{L}\right)\frac{(IIo-[II])}{L_y} + D_2\frac{\partial^2[II]}{\partial x^2},$$

$$\frac{\partial[IIa]}{\partial t} = k_{2_10a5a}\frac{[II][XaVa]}{k_{m2_10a5a}+[II]} + k_{2_10a}\frac{[II][Xa]}{k_{m2_10a}+[II]} - k_{2a_ATIII}[IIa] - H\frac{x}{L}\left(2-\frac{x}{L}\right)\frac{[IIa]}{L_y} + D_{2a}\frac{\partial^2[IIa]}{\partial x^2},$$

$$\frac{\partial[PC]}{\partial t} = -k_{PC_2a}\frac{[PC][IIa]}{k_{mPC_2a}+[PC]} + H\frac{x}{L}\left(2-\frac{x}{L}\right)\frac{(PCo-[PC])}{L_y} + D_{PC}\frac{\partial^2[PC]}{\partial x^2},$$

$$\frac{\partial[PCa]}{\partial t} = k_{PC_2a}\frac{[PC][IIa]}{k_{mPC_2a}+[PC]} - H\frac{x}{L}\left(2-\frac{x}{L}\right)\frac{[PCa]}{L_y} + D_{PCa}\frac{\partial^2[PCa]}{\partial x^2}.$$

**The boundary conditions.** Equations (1) define the boundary condition of the problem at $x = 0$, i.e., at the boundary of a near-membrane layer.

Another boundary condition at $x = L$, where $L$ is a value on the order of the vessel radius, is of the form

$$\left.\frac{\partial[i]}{\partial x}\right|_{x=L} = 0.$$

For $t = 0$, $[i] = [i_0]$ and $[ia] = 0$.

## RESULTS

In Figs. 2 and 3, the concentration distributions for the factors *II*, *IIa* (thrombin), *V*, and *Va* are shown along

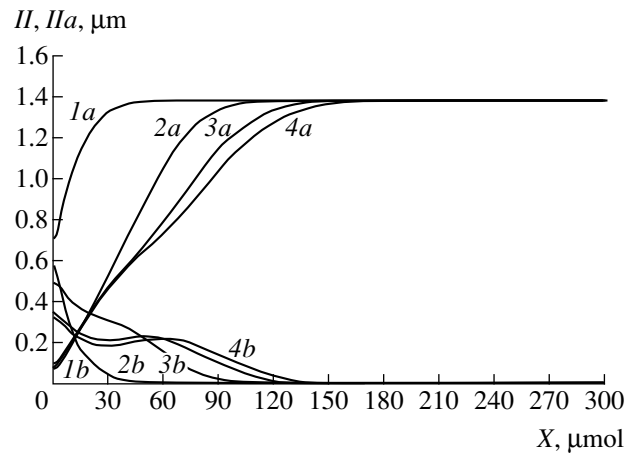


**Fig. 2.** Distributions of the prothrombin and thrombin concentrations over the external-path activation zone. The curves with indices *a* and *b* correspond to prothrombin and thrombin, respectively. The indices *1*, *2*, *3*, and *4* correspond to the time moments of 1, 2, 3, and 4 min after the onset of the process. After an elapsed time of 4 min, the activation-zone front becomes stabilized.

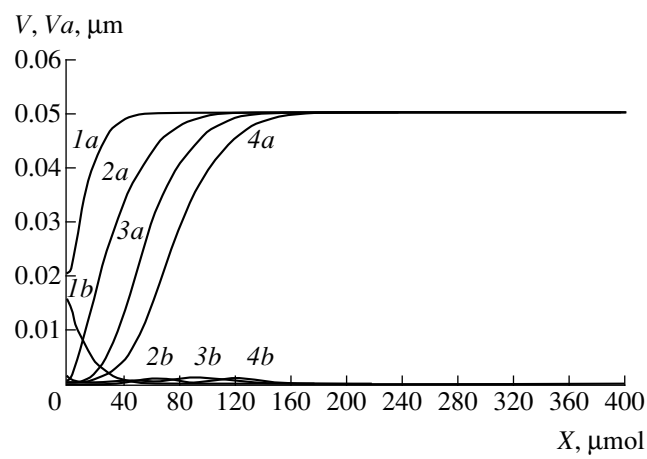


**Fig. 3.** Concentration distributions for the factors *V* and *Va* over the external path activation zone. The curves with indices *a* and *b* correspond to the factors *V* and *Va*, respectively. The indices *1*, *2*, *3*, and *4* correspond to the time moments of 1, 2, 3, and 4 min after the onset of the process. After an elapsed time of 4 min, the activation-zone front becomes stabilized.

the coordinate axis normal to the vessel-wall surface for various instants of time. As is seen from Figs. 2 and 3, the activation-zone front moves deeply into the vessel and attains a certain steady position. If the terms corresponding to hemodynamic transport are discarded in Eqs. (1) and (2), the wave front propagates continuously. The same effect is also observed in the absence of a cascade in the hemocoagulation scheme. Thus, a cascade of fermentative reactions enhances the effect of the hemodynamic entrainment as a factor restricting propagation of the activation zone for a hemostasis system. The greater the number of fermentative reactions involved in a cascade, the smaller the path traversed by the activation zone. For example, an internal path involving a "longer" cascade forms an activation zone with a smaller penetration depth compared to that of the external path. This corresponds to the physiological functions of the external and internal paths, the former of which is fitted at significantly heavier damage of the vessels.

## CONCLUSIONS

Employing the method of mathematical simulation, the hemodynamic entrainment of activated factors is established as the basic mechanism resulting in the termination of hemostasis activation-zone propagation. The same mechanism insures that the thrombus size is adequate for the extent of vessel damage. The mechanism for regulation of the penetration depth of the activation zone associated with the hemodynamic transport of activated factors is essential only in the case of existence of a cascade scheme for fermentative reactions.

The results obtained are appropriate for the case of the activation-zone propagation in a blood flow.

## ACKNOWLEDGMENTS

This study was supported by the International Science Foundation (grants NAK-000 and ITN-4200).

## REFERENCES

1. V. V. Semenov and M. A. Khanin, Biofizika **35**, 139 (1990).
2. M. A. Khanin, Izv. Vyssh. Uchebn. Zaved., Prikl. Nelineĭnaya Din., Nos. 3/4, 65 (1994).
3. M. A. Khanin, V. L. Leytin, and A. P. Popov, Thromb. Res. **64**, 659 (1991).
4. M. A. Khanin and V. V. Semenov, J. Theor. Biol. **136**, 127 (1989).
5. F. I. Attaulakhanov, G. T. Guriya, and A. Yu. Safroshkina, Biofizika **39**, 89 (1994).

*Translated by V. Tsarev*